May 2019

Structural Health Monitoring of Laminate Structures Using Shear-Mode Piezoelectric Sensors

Hussain Altammar
University of Wisconsin-Milwaukee

STRUCTURAL HEALTH MONITORING OF LAMINATE STRUCTURES USING SHEAR-MODE PIEZOELECTRIC SENSORS

by

Hussain Altammar

A Dissertation Submitted in

Partial Fulfillment of the

Requirements for the Degree of

Doctor of Philosophy

in Engineering

at

The University of Wisconsin – Milwaukee

May 2019

ABSTRACT

STRUCTURAL HEALTH MONITORING OF LAMINATE STRUCTURES USING SHEAR-MODE PIEZOELECTRIC SENSORS

by

Hussain Altammar

The University of Wisconsin – Milwaukee, 2019
Under the Supervision of Professors Anoop Dhingra and Nathan Salowitz

Structural health monitoring (SHM) employing embedded piezoelectric transducers has shown potential as a promising solution for inspection of different engineering structures such as aircraft, bridges, and renewable energy structures. Despite advancements in the field of ultrasonic SHM, inspection of laminate structures is still a major challenge due to their susceptibility to various joint defects. This thesis presents a novel approach to tackle the challenge of inspecting laminate structures using shear-mode (d35) piezoelectric transducers that are made of lead zirconate titanate (PZT).

This study begins with the characterization of d35 piezoelectric transducers using analytical, numerical, and experimental approaches. The results were found to match well. A finite element (FE) simulation of a laminate structure was developed based on multiphysics analysis to identify the propagating waves generated by d35 PZT actuators embedded within the bondline of the laminate structure. The group velocities of voltage signals as well as the distributions of normal displacements and stresses induced by the

propagating waves showed that the elastic waves generated by the d35 PZT actuator exhibit the characteristics of antisymmetric (flexural) waves coupled with strong transverse shear stress across the thickness of the adhesive layer. The FE results were validated by testing laminate specimens with bondline-embedded d35 PZTs in a pitch-catch arrangement.

A parametric study was performed to provide design guidelines for d35 PZT sensors and actuators. The thickness and length of d35 PZT transducers were varied while monitoring the actuation strength and the sensed voltage signal. It was found that thicker and shorter d35 PZT sensors can produce stronger signals compared to thinner and longer d35 PZT sensors. On the contrary, d35 PZT actuators were noticed to exhibit the opposite response to d35 PZT sensors. The selectivity of d35 PZT sensors was also investigated in multiphysics simulations by comparing voltage signals obtained from a bondline-embedded d35 PZT sensor and a surface-mounted conventional (d31) PZT sensor. It was found that d35 PZTs offer a selective hardware filter that primarily captures antisymmetric wave modes in the laminate structure while suppressing symmetric wave modes. Filtering symmetric modes significantly reduced the complexity of signal processing and this could potentially enhance the process of SHM as well.

Various joint defects including disbonds, cracks, and voids were introduced in the bondline of laminate structures to investigate the feasibility of embedding d35 PZT transducers in the bondline of laminate structures for detection of joint defects. It was observed that antisymmetric waves generated by d35 PZT actuators exhibited strong interaction with joint defects especially nonlinear defects such as cracks and disbonds. By placing the transducers within the bondline and at the neutral axis of the laminate

structure, it provided a direct strong coupling between the bondline and the d35 PZT transducers resulting in high transmission and sensitivity of flexural waves to joint defects. Several specimens were prepared and tested. The results obtained from experiments and simulations were found in good agreement.

The proposed approach was also evaluated experimentally for health monitoring of bondline integrity. A laminate specimen with bondline-embedded d35 PZT and surface-mounted d31 PZT piezoelectric transducers was subjected to a three-point bending test to create joint defects. Damage indices were implemented to detect the presence of damage and its severity. The experimental results demonstrate the ability of bondline-embedded d35 PZTs to be used as sensors and actuators for ultrasonic SHM of bondline integrity. The proposed approach successfully produced promising results for detection of joint defects that often impose a significant challenge to detect using conventional nondestructive evaluation techniques. The results presented in this thesis provided fundamental work towards creating embedded, automated damage detection systems for laminate structures using bondline-embedded d35 piezoelectric transducers.

To my parents

TABLE OF CONTENTS

LIST OF FIGURES

LIST OF TABLES

ACKNOWLEDGEMENTS

First of all, I would like to express my thanks and appreciation to my advisors, Dr. Anoop Dhingra and Dr. Nathan Salowitz for their time, support, and guidance throughout this study. Without their help, this dissertation would not have been possible. Also, I would like to thank my committee members, Dr. Sudhir Kaul, Dr. Habib Tabatabai, and Dr. Ilya Avdeev for serving on my committee and for their comments and suggestions.

I would like to express special thanks to my sisters and my brothers for their continuous support and encouragement with their faithful prayers for my success. Also, I am very thankful to my beloved wife Sukinah for her sincere support all the time and for all the sacrifices that she had made for me. Finally, I want to express my sincere appreciation and thanks to my parents for their unconditional love and unwavering support throughout my educational journey.

Chapter 1
Introduction

This chapter provides a brief introduction to structural health monitoring followed by its benefits and the current challenges that hinder the growth of SHM to wider applications. This chapter concludes with an overview of the subsequent chapters.

1.1. Introduction to structural health monitoring

Structural health monitoring has been increasingly growing as a promising technology for inspection of engineering structures such as pipelines, bridges, aircrafts, and renewable energy structures. This increasing interest was driven by a high demand for ensuring safety and durability while also reducing maintenance cost. SHM exhibits the merits of a promising solution that can make this possible [1]. In recent years, numerous nondestructive testing and evaluation methods have been developed for damage detection. For example, ultrasonic techniques that are well-established technologies are widely used for scanning various kinds of structures. Despite use of nondestructive testing and evaluation (NDT/E) tools in SHM techniques, there are subtle differences between SHM and NDT/E.

SHM techniques involve the application of permanent sensors that can perform global real time monitoring of the state of structural integrity during operation. SHM is expected to detect defects at an early stage and evaluate their impact on the whole structure. As shown in Figure 1.1, an ideal SHM procedure involves five levels that begin with the primary objective of SHM: damage detection, then followed by damage localization, assessment of damage severity (size), prognosis of remaining useful life, and self-repair

or control of damage [2]. The first four levels have been extensively studied in existing literature and are mostly related to modeling, signal processing and statistical methods. Self-healing is a newly emerging level to the SHM procedure and is still investigated in a laboratory setting with no commercially available solutions.

Figure 1.1: Levels of structural health monitoring procedure.

Installation of SHM systems is very expensive and often performed on new structures. The process of damage identification in SHM is mainly based on history of operation in which measured signals compared against baseline signals to predict damage existence with reasonable probability and accuracy [2]. For damage identification, there are four elements that are required prior to the installation of SHM system to a structure: 1) knowledge of material and geometrical properties of monitored structures; 2) types of possible defects; 3) potential actuators and sensors to collect data; 4) signal processing methods to extract information about damage characteristics and overall structural integrity.

1.2. Benefits of SHM Systems

Safety is the primary factor for the existence of SHM in the first place. However, there are other important benefits of SHM that have economical, aesthetical, ecological impact [3]. Some of the benefits of SHM are: 1) reducing downtime and maintenance costs through early detection of a structural damage; 2) increasing durability while decreasing economic losses for maintenance, repair, and reconstruction; 3) providing an opportunity

to study the performance of new materials and structures in order to create and update numerical models for more advanced structures. As shown in Figure 1.2, there are mainly three elements that justify the necessity of SHM systems in a variety of different structures ranging from civil to aerospace structures.

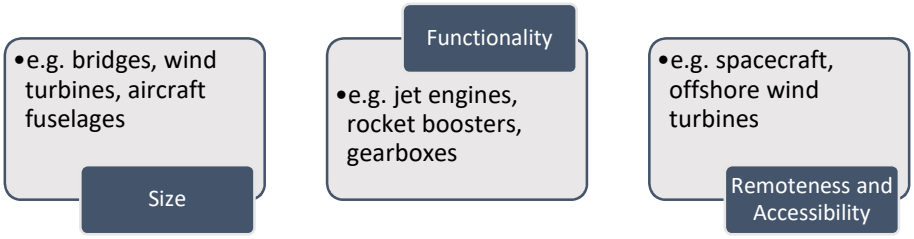

Figure 1.2: Main factors to justify the necessity of SHM systems

- Size – large structures such as bridges, wind turbines, and aircraft structures are often associated with high inspection cost using conventional NDT techniques. Nowadays, even larger structures are being built [4] , e.g., to harvest more power and to lower operation cost. This makes inspection using NDTs very difficult if not even impossible [5].
- Functionality – structures and components that have critical functionality, and their failure could result in catastrophic consequences. For example, jet engines, booster rockets, and gearboxes have SHM systems integrated for fault identification [6].
- Remoteness and accessibility – structures that are located in distant areas, have limited alternative access, or with no physical access are likely to require SHM systems to ensure proper functionality. Spacecraft and offshore wind turbines [4] are common applications in which SHM system is important to fulfill their mission.

Also, structures that are expected to be exposed to frequent harsh environmental conditions are excellent candidate to have a SHM system because it can accelerate the repair process by providing vital information regarding defective units. As the occurrences of violent environmental conditions are in the rise, an infrastructure integrated with SHM systems becomes very desirable. This was also supported by the SHM market growth from $701.4 Million in 2015 to $3407.7 Million by 2022. Other factors to this growth are the growing use of composite structures, the need for health monitoring of structures in hazardous (inaccessible) areas, and the rapidly aging infrastructure [7].

1.3. Challenges in SHM

A significant progress has been achieved in SHM over the last few decades due to the technological advancements that made smart transducers including piezoceramic, fibers, and polymers readily available and at low cost. However, there are still several challenges that hinder wider application of SHM:

- High installation cost especially for existing and old structures.
- Continuous monitoring of a structure often produces big data sets that impose challenges in signal processing, transferring, and storing data [8].
- No standards available for SHM methods that ensure applicability and repeatability among different structures, thus a health monitoring strategy has to be implemented for each structure.
- No real solutions available yet to detect defects in joints such as bolted joints, adhesive joints, riveted joints, etc. NDT methods are still the primary choice.
- Inspection of composites with unknown material properties [9].

- Extraction of damage characteristics via comparison between measured signals and baseline signals.
- Highly fluctuating loads often complicate the detection of damage due to load interaction effects [6].

Adhesive joints are commonly used in aircraft structures due to specific advantages in comparison with conventional joining techniques. However, adhesively bonded structures are susceptible to various types of defects such as cracks, voids, disbonds and delaminations as well as kissing bonds (weak bonds) that are often difficult to detect using conventional NDT/E techniques. Therefore, the objective of this dissertation is to tackle the challenge of detecting joint defects in laminate structures and to develop a health monitoring solution of bondline integrity based on ultrasonic inspection methods.

1.4. Dissertation Overview

This dissertation is organized in ten chapters. Chapter 1 provides brief introduction to structural health monitoring, its benefits, and current challenges to widen its applications in the future. Chapter 2 provides a brief introduction to various ultrasonic waves propagating in solid media. The concept of Lamb waves in waveguide structures is also discussed with more details on solving the Lamb wave equation for symmetric and antisymmetric modes. The Lamb wave dispersion curves are compared with the dispersion curves of shear-horizontal waves as well as conventional flexural and axial waves to foster an understanding of commonly existing modes in solid structures. State-of-the-art in using antisymmetric waves and shear waves for detection of defects in plates and joints are discussed. This chapter also highlights research works in which embedded

sensors in adhesively bonded structures have been pursued. Several damage index methods that have been implemented in the literature to quantify and to locate defects in various kinds of structures are reviewed. The chapter concludes with research questions.

Chapter 3 focuses on studying the linear piezoelectric response of three different transducers: conventional circular, conventional rectangular, and shear-mode plate. The results of free piezoelectric transducers from experiment are compared with closed-form solutions and numerical solutions. Chapter 4 investigates the traits of fundamental Lamb modes under symmetric and antisymmetric actuation to detect structural damage. The propagation of Lamb waves in a thin plate involving the use of piezoelectric transducers are simulated using 3D finite element multiphysics analysis to validate a pitch-catch experiment. A full-field view of elastic wave propagation is discussed to study the interaction of Lamb waves in a plate. This chapter also presents pulse-echo analysis and pitch-catch analysis conducted on a damaged plate with a pair of transducers modeled on both sides to send symmetric and antisymmetric actuation signals. This analysis is then followed by damage localization using the time-of-flight (ToF) approach.

Chapter 5 investigates the properties of ultrasonic waves generated by embedded shear-mode piezoelectric transducers made of lead zirconate titanate using finite element analysis. In Chapter 6, the FE results are validated experimentally by preparing several specimens with d35 PZTs internally embedded in the bondline. Chapter 7 presents a parametric study into the sensing and actuation properties of d35 PZTs. The parametric study includes the effects of d35 PZT size on the strength of actuation and sensed output signals. The selectivity of d35 PZT sensors was also investigated by generating multiple

wave modes in the medium. Time-frequency methods such as Discrete Wavelet Transform and Short-time Fourier Transform are used to process voltage signals.

Chapter 8 investigates the effectiveness of flexural waves to detect damage in laminate structures through internally embedded d35 PZT transducers in the bondline. FE method was used simulate multilayered structures with various defects. Experimental work was performed to validate FE simulations. Chapter 9 is dedicated to study the ability of d35 PZT for health monitoring of bondline integrity. A quasi-static three-point bending test was performed to create joint defects, and damage assessment was quantified using damage index methods. Finally, Chapter 10 summarizes the outcomes and the main findings of this study while addressing the research questions presented in Chapter 2. This final chapter concludes with future work that will be necessary to implement the approach proposed herein to real-life SHM applications.

Chapter 2
Background and Literature Review

This chapter provides a brief introduction to various ultrasonic waves propagating in solid media. The concept of Lamb waves in waveguide structures is also discussed with more details on solving the Lamb wave equation for symmetric and antisymmetric modes in a plate as well as plotting phase velocity and group velocity dispersion curves. Furthermore, the shear-horizontal waves as well as conventional waves including flexural and axial waves are also compared with Lamb waves to foster an understanding of commonly existing waves in structures. State-of-the-art in using antisymmetric waves for detection of defects in plates and joints are also discussed. This chapter highlights research works in which embedded sensors inside structures have been attempted. This is followed by a review of several damage index methods that have been implemented in the literature to quantify and to locate defects in different types of structures. This chapter concludes with the scope of this thesis.

2.1. Introduction to Ultrasonic Waves

2.1.1. Elastic waves

Elastic waves are mechanical waves associated with mechanical forces that result in volume deformation and shape deformation of particles. The motion of waves (disturbances) generated by a wave source (transducer) is significantly small such that the particles allow the waves to propagate at ultrasonic speed (greater than 344 m/s) without causing structural vibration. Thus, the particle velocity which signifies the physical motion of particles in the medium is quite small in comparison to the wave speed.

Standing waves, however, could exist in the medium yielding structural vibration under certain conditions. The frequency of the wave as well as boundary conditions and geometrical properties of the medium are the primary factors that determine the existence of standing waves. Elastic waves which travel in all directions and in infinite unbounded medium are called bulk waves. A specific case of bulk waves is plane waves in which the propagated waves are invariant with respect to one direction, usually referred as z-invariant. When the wave crest is parallel to the z-axis, all the waves travel in the medium are independent of z, $\partial / \partial z = 0$. The equation of plane waves in terms of displacement is described as [10]

$$\vec{u} = \underbrace{\left(\frac{\partial \phi}{\partial x} + \frac{\partial H_z}{\partial y} \right)}_{u_x} \vec{i} + \underbrace{\left(\frac{\partial \phi}{\partial y} - \frac{\partial H_z}{\partial x} \right)}_{u_y} \vec{j} + \underbrace{\left(\frac{\partial H_y}{\partial x} - \frac{\partial H_x}{\partial y} \right)}_{u_z} \vec{k} \tag{2.1}$$

In Eq.(2.1), $\vec{u}$ is the vector displacement, ϕ is the scalar potential of displacement, and H_x , H_y , H_z are displacement potentials in x, y, and z directions, respectively. The characteristics of existing waves in the medium is dictated by the boundary conditions. For instance, surface waves such as Rayleigh waves and Love waves propagate in 3D medium bounded by one surface, see Figure 2.1.

On the other hand, 3D medium bounded by two surfaces allows for propagation of compression waves and shear waves which are guided inside the medium. These waves are usually referred to as guided Lamb waves. When a 3D medium is bounded by another medium, interface waves such as Stoneley waves propagate between two solid media. Scholte waves propagate between a solid medium and a liquid medium. More detailed description is provided in this reference [11]. It is noteworthy to mention that all guided

waves including Lamb waves, surface waves, and interface waves result from the interaction of longitudinal and shear motion components.

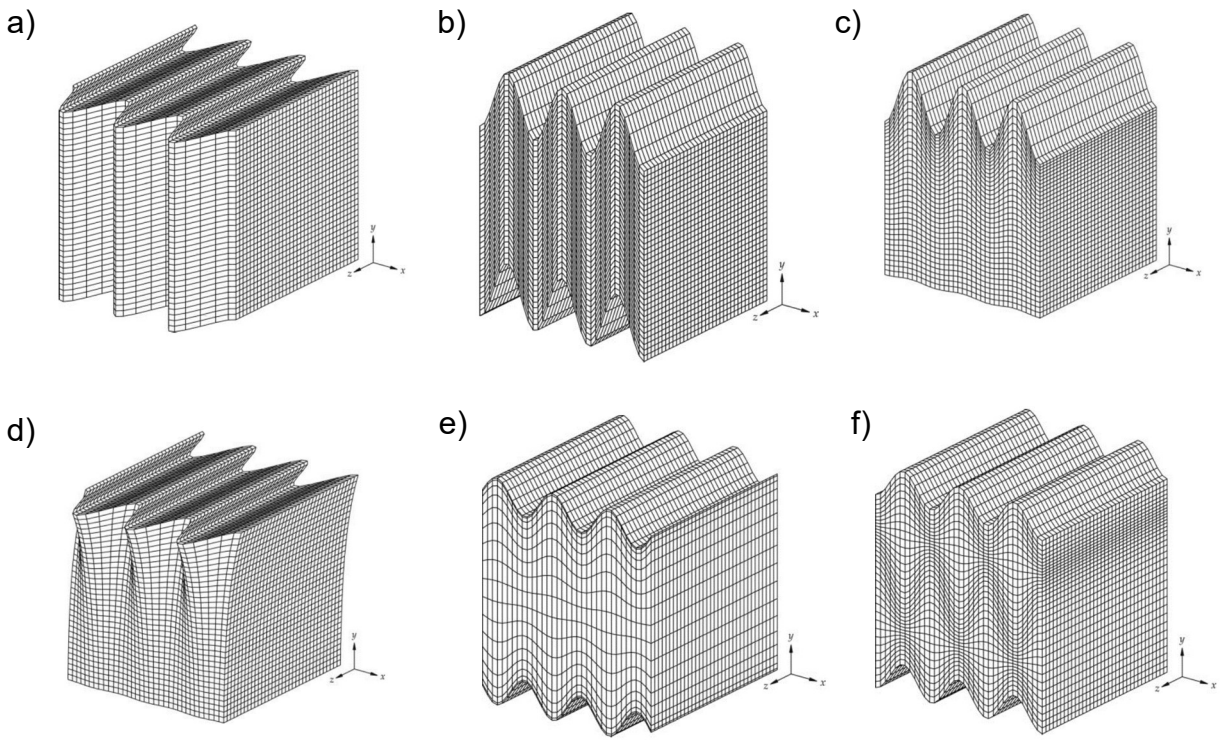

Figure 2.1: Distribution of displacements: a) horizontal shear wave, b) vertical shear wave, c) Rayleigh wave, d) Love wave, e) S0 mode of Lamb waves, f) A0 mode of Lamb waves [10].

2.1.2. Flexural and axial waves

The analysis of flexural wave propagation starts with the governing differential equations of motion in plates. These equations are often expressed in frequency-wavenumber domain to obtain the dispersion relations including phase velocity and group velocity of propagating waves. The dispersion relations define the behavior and characteristics of wave propagation as a function of frequency. The theory of flexural waves in plates is well-established with details on fundamentals and analysis of flexural

waves presented in references [1,12,13]. The flexural wave equation for plates is given as

$$D\frac{\partial^4 u}{\partial x^4}+\rho h\frac{\partial^2 u}{\partial t^2}=0 \tag{2.2}$$

In Eq. (2.2), *h* is the plate thickness, *ρ* is the density, *D* is the bending stiffness defined by the following expression,

$$D=\frac{Eh^3}{12(1-\nu)} \tag{2.3}$$

In Eq.(2.3), *E* is the Young's modulus, ν is the Poisson's ratio. The flexural (bending) wavenumber is defined by

$$\gamma=\frac{\rho h}{D}\omega^2 \tag{2.4}$$

Therefore, the phase velocity can be obtained using the wavenumber-frequency relation, $\gamma=\omega/v_\phi$ as [12]

$$v_\phi=\left(\frac{Eh^2}{12\rho\left(1-\nu^2\right)}\right)^{1/4}\sqrt{\omega} \tag{2.5}$$

The flexural phase velocity, v_ϕ (also known as wave speed) depends on the material properties of the plate, the plate thickness, and the frequency. It can be observed the phase velocity is proportional to the square root of the plate thickness. The group velocity is derived using this relation $v_g=\partial\omega/\partial\gamma$ as

$$v_g=2\left(\frac{Eh^2}{12\rho\left(1-\nu^2\right)}\right)^{1/4}\sqrt{\omega} \tag{2.6}$$

The flexural wave packet can travel twice as fast as the phase of wave within the signal. The difference between the phase velocity and group velocity indicates that the flexural waves are highly dispersive.

The analysis of axial waves in plates is relatively simple and quite similar to axial waves in bars with the only difference of including the Poisson's effect in the wave speed. The axial waves in plates have particle motion in the direction of wave propagation and it is common in literature to refer to axial waves as longitudinal (or pressure) waves. The wave equation of axial waves in plates is given as,

$$c_L \frac{\partial^2 u}{\partial x^2} - \frac{\partial^2 u}{\partial t^2} = 0 \tag{2.7}$$

In Eq. (2.7), c_L is the axial wave speed defined by the following expression,

$$c_L = \sqrt{\frac{1}{1-\nu^2}\frac{E}{\rho}} \tag{2.8}$$

As can be observed from Eq. (2.8), axial waves do not depend on angular frequency and that suggests the phase velocity and group velocity of axial waves are identical and axial waves are nondispersive.

2.1.3. Shear Horizontal Waves

Guided waves are elastic waves propagating at ultrasonic sound speed in an elastic medium. In a thin plate, shear horizontal waves and Lamb waves can coexist. Shear horizontal (SH) waves are characterized by particle motion perpendicular to the direction of wave propagation. SH waves can be symmetric (S_0, S_1, S_2,…) and antisymmetric (A_0,A_1,A_2,…). The governing equation of SH waves in plates is

$$\left(\frac{\partial^2}{\partial x^2}+\frac{\partial^2}{\partial y^2}\right)u_z=\frac{1}{c_s^2}\frac{\partial u_z}{\partial t^2} \tag{2.9}$$

In Eq. (2.9), c_s is the shear wave speed defined by the following expression,

$$c_s=\sqrt{\frac{1}{2(1+v)}\frac{E}{\rho}} \tag{2.10}$$

The wave speed of symmetric and antisymmetric SH modes given in terms of eigenvalues are expressed as,

$$c(\omega)=\frac{c_s}{\sqrt{1-(\beta h)^2\left(\frac{c_s}{\omega h}\right)^2}},\quad (\beta h)^{sy}=0,\,2\frac{\pi}{2},4\frac{\pi}{2}...;\quad (\beta h)^{as}=\frac{\pi}{2},\,3\frac{\pi}{2},5\frac{\pi}{2},.... \tag{2.11}$$

In Eq. (2.11), *h* is the half-thickness of the plate, ω is the angular frequency, and βh is the eigenvalue of SH wave mode. It is worth noting from the wave-speed formula in Eq.(2.11) that the first symmetric SH-S0 mode is not dispersive and as the angular frequency approaches infinity, the wave speed of all SH modes approaches the shear wave speed, i.e., SH-S0 wave speed.

2.1.4. Lamb Waves

Interaction of longitudinal waves and vertical shear waves inside the plate thickness yields guided Lamb waves which can also exist as symmetric Lamb waves (S0, S1, S2,…) and antisymmetric Lamb waves (A0, A1, A2,…). Rayleigh waves result from the interaction of P-wave and vertical shear waves near the surface and its speed is independent of frequency. Love waves, unlike Rayleigh waves, are dispersive and result from SH waves trapped near the surface [12].

Eigenvalues of Lamb wave equation yield symmetric and antisymmetric propagation modes [14]. The wavenumber can take any value including real, imaginary and complex numbers. Complex wavenumbers with negative imaginary value indicate decaying waves which are called evanescent and their amplitudes decrease exponentially with distance. This phenomenon can be observed at a near field of scattering center such as a notch. However, complex wavenumbers with positive imaginary value indicate exponentially growing waves. Real wavenumbers which are of interest to plot the dispersion curves indicate propagation of waves with no damping (harmonic modes).

The Lamb wave equation is highly nonlinear and can only be solved by numerical methods. To obtain only real solutions, the Lamb wave equation for symmetric modes can expressed as [14]

$$\frac{\tan(qh)}{q} = -\frac{4\zeta^2 p \tan(ph)}{(q^2-\zeta^2)^2} \tag{2.12}$$

For antisymmetric modes,

$$q\tan(qh) = -\frac{(q^2-\zeta^2)^2 \tan(ph)}{4\zeta^2 p} \tag{2.13}$$

In Eq. (2.13), *h* is half-thickness, ζ is the wavenumber equal to ω/v_ϕ, where ω is the angular velocity, q and p are defined as the following

$$p^2 = \frac{\omega^2}{c_p^2} - \zeta^2 \qquad q^2 = \frac{\omega^2}{c_s^2} - \zeta^2 \tag{2.14}$$

where c_p is the longitudinal wave speed and c_s is the shear wave speed. The phase velocity dispersion curves of a traction-free aluminum plate are plotted in Figure 2.2.

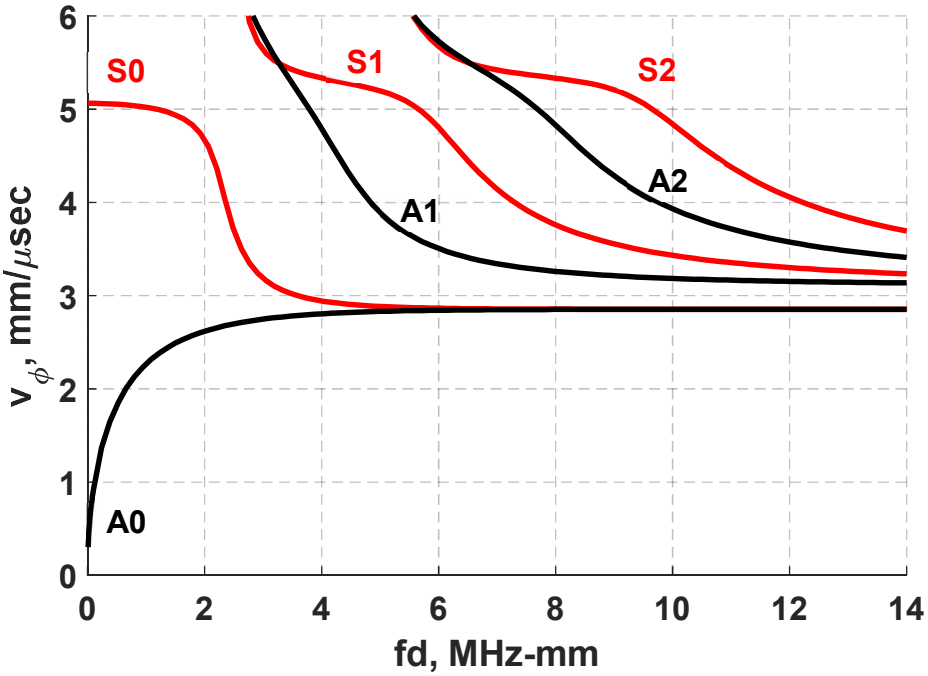

Figure 2.2: Phase velocity dispersion curves of symmetric and antisymmetric Lamb wave modes in a traction-free aluminum plate.

Furthermore, the group velocity dispersion curves can also be derived from the phase velocity dispersion curves using the following expression [14]

$$v_g = v_\phi^2 \left[v_\phi - (fd) \frac{dv_\phi}{d(fd)} \right]^{-1} \tag{2.15}$$

In Eq. (2.15), fd is the frequency times thickness, $dv_\phi / d(fd)$ is the derivative of v_ϕ with respect to fd. The group velocity dispersion curves of a traction-free aluminum plate are plotted in Figure 2.3.

The dispersion rate of group velocity can be calculated as

$$a_g = \frac{dv_g}{d(fd)} \tag{2.16}$$

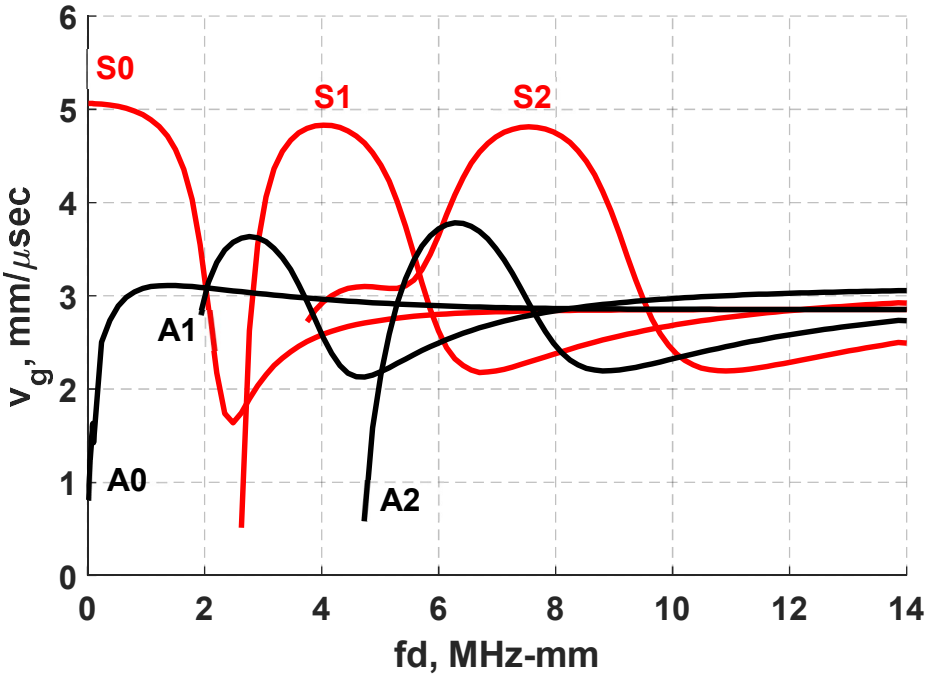

Figure 2.3: Group velocity dispersion curves of symmetric and antisymmetric Lamb wave modes in a traction-free aluminum plate.

The dispersion curves of Lamb waves in Figure 2.2 and Figure 2.3 indicate that certain wave modes can exist at a given frequency-thickness. For example, at low frequencies (e.g. 1 MHz) the fundamental Lamb S0 and A0 modes are expected to propagate in the media while other modes may not exist because their critical frequencies are higher than 1 MHz.

2.1.5. Ultrasonic waves in plates

As previously mentioned, multiple wave modes can coexist in the media depending on the frequency-thickness product and the transduction mechanism. The phase velocity and group velocity dispersion curves for 1-mm thick aluminum plate are displayed in Figure 2.4 and Figure 2.5. The material properties of aluminum are provided in Table 1 of the Appendix. The dispersion curves show that all other modes are expected to exist

at all frequencies except (SH-A0), the first antisymmetric A0 mode of the SH waves. However, at low frequencies the fundamental Lamb waves (S0 and A0 modes) have the characteristics of conventional axial waves and flexural waves respectively while at higher frequencies they differ substantially in plates. At high frequencies, the wave speed of fundamental Lamb modes will eventually converge to the speed of Rayleigh waves (2.85 mm/μsec). Their behavior will also resemble Rayleigh waves that are only confined to the free surfaces of the plate. Similarly, it can also be noted from Figure 2.4 and Figure 2.5 that the wave speed of SH-A0 approaches the shear wave speed of (SH-S0), the first symmetric S0 of the SH waves.

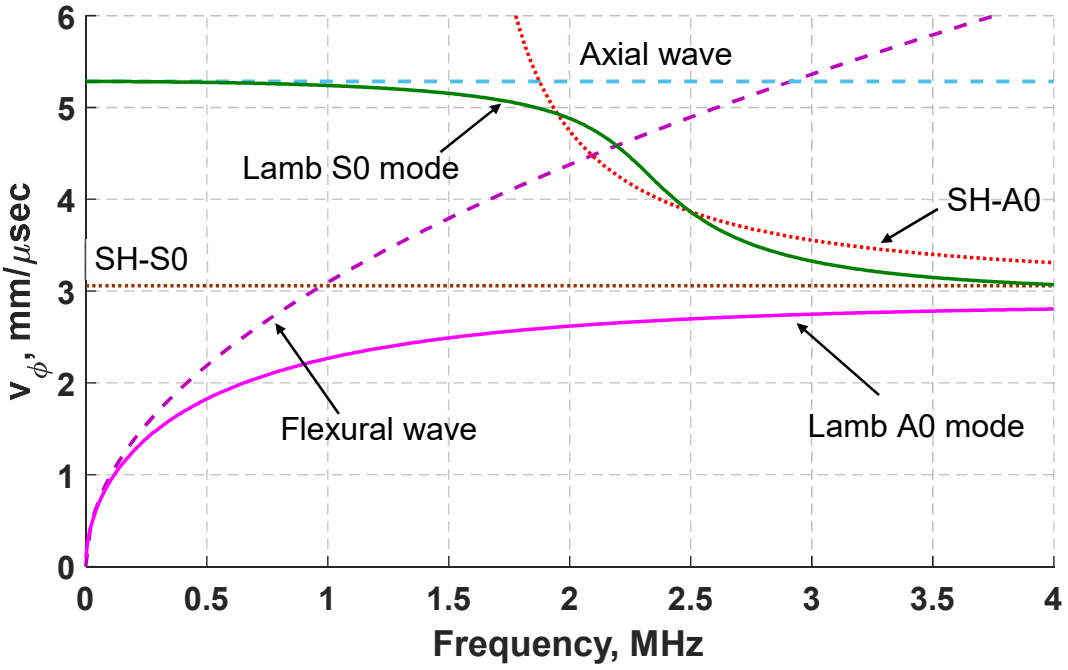

Figure 2.4: Phase velocity dispersion curves of axial waves, flexural waves, Lamb wave S0 and A0 modes, and fundamental SH modes in 1-mm thick aluminum plate.

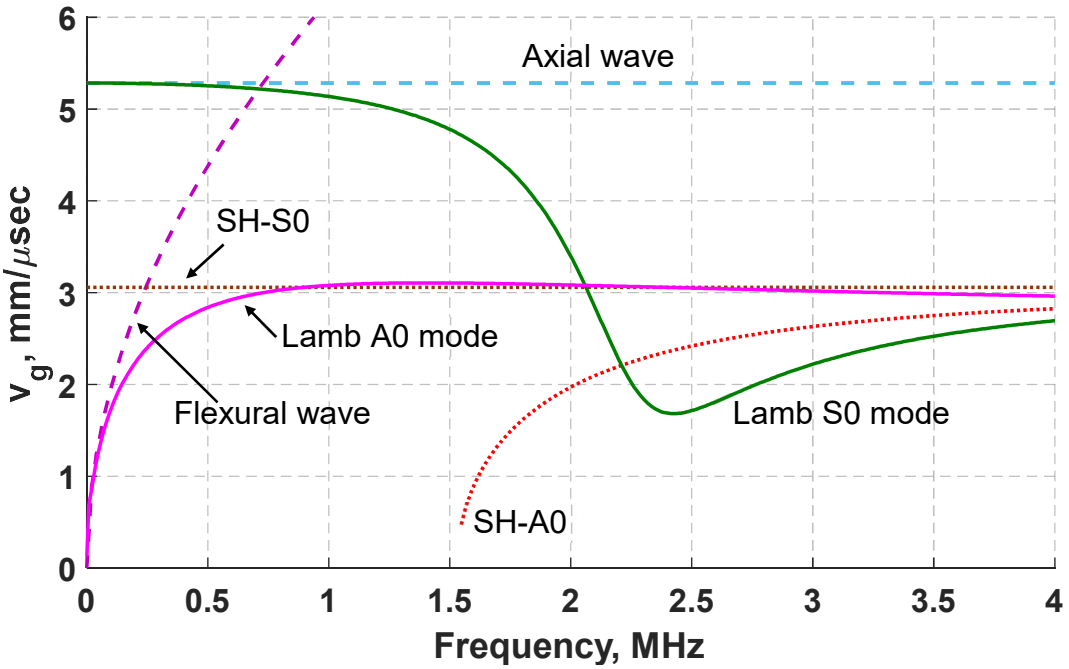

Figure 2.5: Group velocity dispersion curves of axial waves, flexural waves, Lamb wave S0 and A0 modes, and fundamental SH modes in 1-mm thick aluminum plate.

2.2. Ultrasonic Waves for Damage Detection

2.2.1. Using shear waves to detect defects in plates

At higher actuation frequencies, a complex superposition of wave modes can coexist in the plates resulting in complex patterns that make interpretation of the data a challenging task. An advantage of antisymmetric waves, which make them often preferred over symmetric waves, enables a simple comparison between reflection and transmission waves from pristine state and damaged state. This phenomenon, which is called mode conversion, is discussed in Chapter 4. Pau et al. [15] studied the scattered modes from A0 mode in plates with simple geometric discontinuities consisting of one-sided notch and double-sided notch. An analytical method based on the principle of reciprocity in elastodynamics was implemented to determine the reflection and transmission modes

from a notch at various values of the frequency-thickness product. The analytical solution was found in close agreement with finite element (FE) results.

Kohler et al. [16] designed a piezoelectric fiber patch (PFP) transducer that can mainly excite directional shear horizontal (SH0) waves in a plate. It was concluded that the PFP transducers are highly efficient when the inspection of far distance spots is required. Traditionally, bends in structures are often inspected with wedge transducers that produced dispersive Lamb waves. Yu et al. [17] investigated the propagation of shear horizontal waves in a structure with 90^{o} bend. The velocity of dispersion curves was extracted revealing the guided SH mode confined in curvature regions maintains its strength at higher actuation frequencies. Similar findings were reached by Nazeer et al. [18]. They studied the interaction of SH guided waves with defects in the bend region of a structure. They found strong relation between the actuation frequency and the sensitivity of SH0 to inner and outer bend defects.

2.2.2. Using antisymmetric waves to detect joint defects

Adhesive joints are commonly used due to specific advantages in comparison with conventional joining techniques such as fastening, welding, riveting, etc. Adhesive joints offer a capability to join non-similar materials, thereby allowing design flexibility that has led to the use of composites in high performance applications such as aircrafts and electronic microchips [19].

Adhesive joints are used extensively in construction and repair in various areas for bonding metallic materials and non-metallic materials together. However, adhesive joints are susceptible to various types of defects such as cracks, voids, disbond, delamination,

and most recently categorized type of defect known as kissing bond. Kissing bonds are one of the most difficult defects to detect using conventional ultrasonic techniques due to their unique mechanical characteristics [20]. Typical failure of a composite structure with kissing bonds is at the interface between the adhesive and the adherent which is known as adhesive failure mode. Kissing bonds often result from seemingly flawless interface with little bonding strength surrounded by normally well-bonded areas.

In existing literature, kissing bonds have been defined slightly different among researchers yielding several techniques in creating artificial kissing bonds in test specimens. There are two approaches commonly used to create kissing bonds: 1) use of chemical contaminants to weaken the adhesive joint at a predefined region and 2) varying the compressive normal stress applied on a specimen that has an interface-open-crack, disbond. Marty et al. [21] conducted an extensive experimental study on detection of joint defects including kissing bonds through the simulation of defects in the bondline of aluminum samples using silicon based contamination. Nagy [22] considered using conventional C-scan configuration to produce longitudinal and shear waves at the interface of six specimens by varying the angle of incidence. Joint defects were created in the adhesive bondline by painting spots with a release agent. The sensitivity of shear waves to artificial joint defects was found higher compared to the longitudinal waves created at normal incidence.

Kundu et al. [20] have conducted harmonic ultrasonic testing on glass specimens using two transducers in a pitch-catch arrangement that is similar to C-scan configuration. The transducers however have been placed at an angle with respect to the vertical axis in order to produce Lamb waves in the specimens. The transmitting transducer was set

to send a tone burst signal with a frequency sweep to capture the first seven Lamb modes at a specific phase velocity. Another specimen with about the same thickness as the pristine specimen and comprised of two glass plates compressed together by hydraulic pressure to simulate weak bonds was also tested for monitoring changes in the propagation of Lamb waves. They found all modes insensitive to the presence of kissing bond except for the first antisymmetric, A0, but this sensitivity was found limited to just a certain range of phase velocities.

Studies that have addressed damage detection of layered structures using wave propagation of antisymmetric Lamb waves from surface-mounted PZT transducers were performed by several researchers [23–25]. Diaz Valdes and Soutis [23] found the A0 with a low excitation frequency range (<100 kHz) produced promising results for detection of delaminations in a composite beam using surface-mounted piezoelectric transducers. This was followed by FE analyses to qualitatively investigate the interaction of Lamb waves across the surface of a plate using a linear array of actuators excited at 20 kHz to ensure the predominance of A0 mode. Similarly, Osmont et al. [24] used low-frequency A0 Lamb waves (10 and 20 kHz) to detect and localize damage in a foam core of a sandwich plate with round piezoelectric transducers mounted on the skin. Pau et al. [15] studied the scattered modes from A0 mode in plates with simple geometric discontinuities consisting of one-sided notch and double-sided notch. Cuc and Giurgiutiu [26] have tested and simulated guided Lamb waves in an aluminum lap joint to detect a disbond using conventional d31 piezoelectric transducers in a pitch-catch configuration. It was observed a strong attenuation of the S0 Lamb wave mode occurs along the bondline

compared to the A0 mode. This ability to use guided waves to inspect complex structures provides a foundation on which to inspect bondlines and their possible failure modes.

2.2.3. Embedded sensors in adhesively bonded structure

Electromechanical impedance (EMI) is a rapidly evolving technique in structural health monitoring due to its inherent sensitivity to structural stiffness. The EMI response is often obtained over the first resonance by a frequency sweep. Blanas et al. [27] have embedded bimorph piezo-composite film in composite plates for detection of acoustic emission signals. Zhuang et al [28] investigated the feasibility of embedding piezoelectric sensors into the adhesive bond joints and monitor their EMI in order to predict the bondline integrity. They tested single-lap shear samples made of aluminum with PZT disc embedded in the bondline to be quasi-statically loaded in ultimate tension system to investigate the relationship between the sensor response and the load history on the joint strength. The static load was increased cyclically until failure while the EMI measurements were collected under no-loading condition. The piezoelectric transducer response in a pristine sample was compared with the response of a sample with kissing bond through calculation of the root mean square deviation (RMSD). They found the damage index relatively constant for all samples including samples with surface contaminates until around 80% to 90% of the failure load.

This work was further extended by Dugnani et al. [29] in which they developed a different method to interpret the EMI response of an embedded piezoelectric transducer replacing RMSD damage index. The proposed method, named the proposed-minimum detection method, traces the cross-correlation of two parameters which are the normalized shift and change in the first radial resonant frequency corresponding to the

reference response measured prior to any surface degradation caused by the application of a quasi-static load on samples. This method was found able to predict joint failure earlier than RMSD method.

Since the electrical impedance of piezoelectric transducer influenced by the acoustical impedance of the inspected structure, a recent development in narrowband ultrasonic spectroscopy (NBS) technique was based on monitoring the transducer's electrical impedance instead of its resonance frequency. Therefore, a change in the structure's acoustical impedance is reflected on the transducer's electrical impedance. Instruments such as a bond tester designed according to this concept are commonly used to detect boundary defects such as disbond and delamination in aerospace structures such as aluminum and carbon fiber reinforced panel (CFRP) samples [30]. This technique, however, was proved incapable of detecting kissing bonds in aluminum samples. Narrowband ultrasonic spectroscopy in a single frequency mode was found unable to detect the presence of kissing bond due to the very nature of measurements being performed in a single frequency that isn't sensitive to this type of defect [30].

Murayama et al. (2011) deployed fiber Bragg grating (FBG) optic sensors into the adhesive layers of two single-lab joints specimen to monitor the variation of longitudinal strain distribution inside the adhesive joints [31]. Similarly, Sulejmani et al, (2014) investigated the use of shear stress optical fiber sensors embedded in the bondline of a single-lab joint specimen for disbond detection. Disbond in the bondline was created by tensile cyclic loading. The sensors were found to be sensitive to small disbonds of 100 μm [32]. Yeager et al. (2017) conducted an investigation into the use of surface-mounted and internally embedded FBG optic sensors for SHM of composite structures. They

assessed the robustness of FBGs in composites through water exposure, comparison of manufacturing techniques, and damage detection. It was found that FBG sensors can survive high temperature curing (185^{o}F) but the resulting micro-bending and micro-constriction from manufacturing techniques caused false discontinuities in the strain response [33].

Pieper et al. [34] have used frequency selective surfaces (SSFs) which are often designed to operate in reflection or transmission modes as filters. They have embedded SSFs in multilayered structures to monitor normal and shear strain via electromagnetic resonant response. It was noted that joint defects at the vicinity of SSF sensors can be detected with high resolution.

2.2.4. Shear-mode PZT transducers

Recently there has been increasing interest in using shear-mode (d35) PZTs for SHM. Kamal and Giurgiutiu [35] have studied shear horizontal waves excited with d35 piezoelectric actuators attached to the surface of aluminum plates. They have derived a closed-form solution to predict the propagation of SH waves in simple structures. The analytical results were then validated with experimental work using d35 PZTs as well as conventional d31 PZTs. Some other studies involving the use of shear-mode PZTs as actuator mechanisms were conducted by some researchers in [36–38]. Benjeddou and Deu [36,37] have presented a 3D analytical formulation of transverse shear actuation and sensing to study the static response and the resonant frequencies of a piezoelectric laminated plate with a d35 PZT sandwiched between two graphite/epoxy plates. A 3D FE for static analysis of a sandwiched beam with a d35 PZT embedded as the central layer was presented by Koutsawa et al. [38].

2.3. Damage Index

Damage index (DI) is a scalar quantity which is essentially the difference between two signal contents of the same entity being processed using statistical methods. A list of some commonly used and recently developed statistical methods are included in Table 2-1. In the literature, the damage index method has been used for signals in the time domain and in the frequency domain. The damage index sensitivity relies heavily on the signal characteristics and the statistical method implemented to process the signals. The damage index is typically used to detect the presence of damage and assess its severity. It can also yield the location of damage when the damage index is calculated at different locations of a structure.

Table 2-1: Damage index methods used in literature.

Damage index (DI)	Description
Root mean square deviation (RMSD) [39]	$RMSD = \sqrt{\sum_{i=1}^{N}\left(X_i - x_i\right)^2 \Big/ \sum_{i=1}^{N} X_i^2}$
Peak-to-peak amplitude [40]	$PTPA = A_X / A_x$
Pearson correlation coefficient (PCC) [41]	$PCC = 1 - Cov/\sigma_X\sigma_x \qquad Cov = 1/N\sum_{i=1}^{N}\left(X_i - \bar{X}\right)\left(x_i - \bar{x}\right)$
Mean absolute percentage deviation (MAPD) [42]	$MAPD = \sum_{i=1}^{N}\left\|\left(X_i - x_i\right)/X_i\right\|$
Normalized correlation moment (NCM) [43]	$NCM = \sum_{i=1}^{N}\sum_{j=1}^{M} t_j^n \left\|X_i x_{i-j}\right\| - \sum_{i=1}^{N}\sum_{j=1}^{M} t_j^n \left\|X_i X_{i-j}\right\| \Big/ \sum_{i=1}^{N}\sum_{j=1}^{M} t_j^n \left\|X_i X_{i-j}\right\|$
Normalized signal energy (NSE) [44]	$NSE = \sum_{i=1}^{N} X_i^2 - \sum_{i=1}^{N} x_i^2 \Big/ \sum_{i=1}^{N} X_i^2$

In Table 2-1, X_i is the pristine state at the i^{th} measurement point, x_i is the comparison signal (damaged state) at i^{th} measurement point, t_i is the time at i^{th} measurement point, the j^{th} index for shifting (sliding) the series to measure the similarity between two states, n is an arbitrary moment order, σ_X, σ_x are the standard deviations, $\bar{X}$, $\bar{x}$ are the mean of the pristine signal and the comparison signal, respectively.

Taheri and Cheraghi [45] proposed a damage energy index based on empirical mode decomposition (EMD) to monitor the change in stiffness by using modal analysis of a structure. The proposed approach was demonstrated on several simulations of a pipe modeled as a cantilever beam with an array of piezoelectric sensors along its length to obtain the vibration response including mode shapes and natural frequencies. They found the damage index can predict the damage location within a range of a pair of sensors. The damage severity was found proportional to the magnitude of the damage index.

Hu et al. [46] adapted RMSD and correlation coefficient deviation (CCD) damage indices to detect damage in simply supported concrete structure using EMI of PZTs. They conducted experimental and numerical studies to verify the effectiveness of EMI method in predicting the size and location of damage via hosting four PZT transducers on each quarter of the structure. The EMI response signal before and after inflicting damage were collected for damage diagnostics. The EMI found sensitive to a half-thickness crack, but the damage indices show little growth from the pristine state to the damaged state. Consistent results, however, were observed for larger damage.

Tseng et al. [42] investigated four damage indices on an aluminum specimen with varying damage (hole) sizes. Covariance (Cov) and correlation coefficients (CC) showed uniform and consistent decrease with the increase in damage size compared to RMSD

and MAPD methods. The Cov and CC methods were concluded to be more appropriate choices to characterize the size of damage. A similar conclusion was supported by Torkamani et al. [43] in which CC method was found incapable in assessing the damage severity of a delaminated composite.

Therefore, a damage index based on local statistical features of guided Lamb waves was proposed by Torkamani et al. [43]. The damage index, called normalized correlation moment, was tested to detect and assess delamination in laminated composite structures via numerical simulations and experimental data. It was shown that the proposed method can outperform CCD method. NCM has low sensitivity to the noise level and is sensitive to the wave attenuation while CCD is completely insensitive to the attenuation. Wave attenuation, which is a gradual reduction in magnitude of the wave signal, could happen due to damage existence, inhomogeneity of the tested material and travel distance. Giurgiutiu and Rogers [39] have used RMSD to quantify the severity of disbond by attaching disbond gauges on adhesively bonded rotor blade structure. The damage index was calculated based on the EMI before and after the damage was introduced to the structure.

2.4. Summary and Scope of the Thesis

From this detailed survey, it was found that SHM of laminate structures has several issues that need to be addressed before it could be deployed on real-life structures. Despite ultrasonic NDT methods such as C-scan and wedge transducers found effective for detection of joint defects in laminate structures, they are often expensive and require taking the structure offline for inspection and evaluation. Furthermore, inspection of large and remote structures is still a challenge for NDTs. This thesis aims to tackle the

challenge of detecting joint defects in laminate structures using bondline-embedded d35 piezoelectric transducers for the purposes of ultrasonic SHM. The following questions will be addressed in this thesis.

1. *Can embedded piezoelectric transducers in the bondline be used to identify the presence of damage in an adhesive joint through wave propagation?*

2. *If so, can the proposed technique detect various types of damage such as voids, cracks, and disbond?*

3. *To what extent simulation approach can be beneficial to this study in terms of validation of the experimental results?*

4. *Can the proposed technique make use of signal processing methods to detect the severity of damage? If so, what is the damage detection algorithm?*

Despite a relatively large body of work has employed piezoelectric transducers for damage detection, most the work was concerned with either conventional d31 piezoelectric wafer active sensors or d33 PZT interdigitated transducers. There have been no studies considering the use of bondline-embedded d35 PZTs for ultrasonic inspection of laminate structures. This thesis will investigate the sensing and actuation properties of d35 PZTs that are internally embedded in the bondline of laminate structures. A parametric study of d35 PZT size will also be performed while monitoring the strength of actuation and sensed output signals in order to make informed design decisions about size of d35 PZT sensors and actuators. The feasibility of bondline-embedded d35 PZTs for health monitoring of bondline integrity and detection of different joint defects in laminate structures will be investigated. These analyses will be conducted

through FE simulations based on multiphysics analysis in conjunction with several laminate specimens that will be prepared and tested to validate the FE findings.

Chapter 3
Characterization of Free Piezoelectric Transducers: Circular, Rectangular, and Shear-mode Plate

This chapter focuses on studying the linear piezoelectric response of three different transducers: conventional circular, conventional rectangular, and shear-mode plate. A 2D analytical analysis of circular piezoelectric transducer polarized along its thickness is performed for the impedance response and planar electromechanical (EM) resonant frequencies. Then, the results from closed-form expressions are compared with experimental and FE results. A 1D analysis of a conventional rectangular transducer polarized along its thickness was conducted next to obtain axial electrical resonances and the impedance response. The piezoelectric response is determined experimentally and numerically, and then a comparison with analytical response is performed. A detailed 2D analysis of a shear-mode transducer is also conducted to derive closed-form solutions of mechanical and electromechanical responses as well as the impedance response. Experimental results and FE solutions based on multiphysics analysis are compared with analytical results.

3.1. Circular Piezoelectric Transducers

This section addresses the piezoelectric response of a circular transducer that is polarized in the thickness direction. In Figure 3.1, a circular transducer has radius, R, and thickness, h, with material properties listed in Table 1 of the Appendix. A harmonic voltage is applied to the bottom and top electrodes inducing an electrical field over the surface area of the transducer. The piezoelectric response is determined by deriving a closed-

form expression of the impedance response which is followed by FE and experimental analysis for comparison purposes.

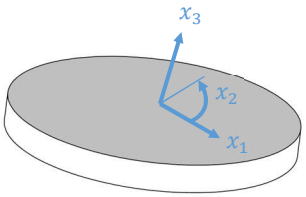

Figure 3.1: A d31 circular piezoelectric transducer polarized in x_3 - direction.

3.1.1. Analytical model

Piezoelectric materials have linear relation between the mechanical and the electrical components. The general constitutive equations in tensorial form are expressed in IEEE standard format [1]

$$T_{ij} = c^{E}_{ijkl} S_{kl} - e_{kij} E_k \tag{3.1}$$

$$D_i = e_{ikl} S_{kl} + \varepsilon^{T}_{ik} E_k \tag{3.2}$$

In Eq.(3.1) and Eq.(3.2), T_{ij} is the mechanical stress, c^{E}_{ijkl} is the material stiffness coefficient at zero electrical field, S_{kl} is the mechanical strain, E_k is the electrical field, D_i is the electrical displacement, ε^{T}_{ik} is the material dielectric permittivity at zero mechanical stress, e_{kij} and e_{ikl} are the piezoelectric stress coupling coefficients between mechanical and electrical variables. Since a vertical line across the piezoelectric thickness remains vertical in vibration, the electrical field can be assumed to be uniform over the transducer, i.e. $\partial E_3 / \partial x_3 = 0$. This also means that the transducer has uniform radial and circumferential expansion, thus the analysis can be reduced to a 2D axis-symmetric problem, i.e.

$\partial(.)/\partial x_2 = 0$ and $u_2 = 0$. The stress constitutive equations of the piezoelectric transducer in polar coordinates can be simplified as:

$$T_{11} = c_{11}^E S_{11} + c_{12}^E S_{22} - e_{31} E_3 \tag{3.3}$$

$$T_{22} = c_{21}^E S_{11} + c_{22}^E S_{22} - e_{31} E_3 \tag{3.4}$$

$$D_3 = e_{31} S_{11} + e_{31} S_{22} + \varepsilon_{33}^T E_3 \tag{3.5}$$

In Eq.(3.3) through Eq.(3.5), S_{11} and S_{22} are the radial strain and the tangential strain respectively, T_{11} and T_{22} are the radial and circumferential stresses respectively, e_{31} is the piezoelectric stress coupling constant. As per stiffness-compliance relation, the stiffness coefficients for a 2D isotropic material are

$$\begin{bmatrix} c_{11}^E & c_{12}^E \\ c_{21}^E & c_{22}^E \end{bmatrix} = \begin{bmatrix} s_{11}^E & -\nu s_{11}^E \\ -\nu s_{11}^E & s_{11}^E \end{bmatrix}^{-1} = \begin{bmatrix} \dfrac{1}{(1-\nu^2)s_{11}^E} & \dfrac{\nu}{(1-\nu^2)s_{11}^E} \\ \dfrac{\nu}{(1-\nu^2)s_{11}^E} & \dfrac{1}{(1-\nu^2)s_{11}^E} \end{bmatrix} \tag{3.6}$$

In Eq.(3.6), s_{11}^E is the compliance coefficient, and ν is the Poisson's ratio.

The electrical field and the general response of a transducer subjected to a harmonic alternating voltage are also harmonic and can be expressed as:

$$V(t) = \hat{V} e^{i\omega t} \tag{3.7}$$

$$E_3(t) = \hat{E}_3 e^{i\omega t} \tag{3.8}$$

$$u_1(t, x_1) = \hat{u}_1(x_1) e^{i\omega t} \tag{3.9}$$

For a relative free-motion at the axis of symmetry and stress-free boundaries, the boundary conditions can be stated as:

$$\begin{aligned} \hat{u}_1(0) &= 0 \\ T_{11}(R) &= 0 \end{aligned} \tag{3.10}$$

Application of Newton's second law on an infinitesimal element of a circular piezoelectric transducer shown in Figure 3.2 yields the equation of motion

$$\frac{\partial T_{11}}{\partial x_1} + \frac{1}{x_1}(T_{11} - T_{22}) = \rho \frac{\partial^2 u_1}{\partial t^2} \tag{3.11}$$

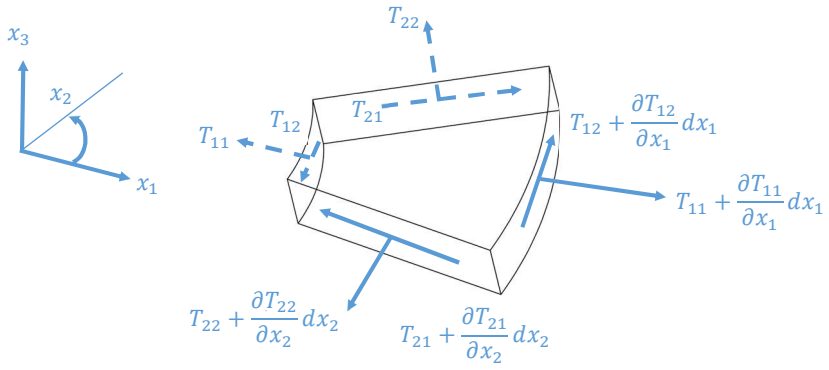

Figure 3.2: Infinitesimal polar element in cylindrical coordinate system.

Recall stress-strain relation,

$$\begin{aligned} S_{11} &= \frac{\partial u_1}{\partial x_1} \\ S_{22} &= \frac{1}{x_1}\frac{\partial u_2}{\partial x_2} + \frac{u_1}{x_1} \end{aligned} \tag{3.12}$$

Substitution of Eq.(3.12) and Eq.(3.6) into Eq.(3.3) through Eq.(3.5) yields

$$T_{11} = c_{11}^E \frac{\partial u_1}{\partial x_1} + v c_{11}^E \frac{u_1}{x_1} - e_{31} E_3 \tag{3.13}$$

$$T_{22} = vc_{11}^{E}\frac{\partial u_1}{\partial x_1} + c_{11}^{E}\frac{u_1}{x_1} - e_{31}E_3 \tag{3.14}$$

$$D_3 = e_{31}\frac{\partial u_1}{\partial x_1} + e_{31}\frac{u_1}{x_1} + \varepsilon_{33}^{T}E_3 \tag{3.15}$$

Using the general solution given in Eq.(3.9) and substituting the expressions of T_{11} and T_{22} into Eq.(3.11) yields

$$\frac{\partial^2 \hat{u}_1}{\partial x_1^2} + \frac{1}{x_1}\frac{\partial \hat{u}_1}{\partial x_1} - \frac{1}{x_1^2}\hat{u}_1 = -\frac{\omega^2}{c_p^2}\hat{u}_1 \tag{3.16}$$

The planar wave speed c_p in the material is

$$c_p = \sqrt{\frac{c_{11}^{E}}{\rho}} \tag{3.17}$$

The wavenumber is defined as:

$$\gamma = \frac{\omega}{c_p} \tag{3.18}$$

Rearranging Eq.(3.16) and introducing the wavenumber yields

$$x_1^2\frac{\partial^2 \hat{u}_1}{\partial x_1^2} + x_1\frac{\partial \hat{u}_1}{\partial x_1} + (x_1^2\gamma^2 - 1)\hat{u}_1 = 0 \tag{3.19}$$

This is a special ordinary differential equation (ODE) called Bessel function which has variable coefficients and has general series solution as:

$$\hat{u}_1(x_1\gamma) = A_1 J_1(x_1\gamma) + A_2 Y_1(x_1\gamma) \tag{3.20}$$

$J_1(.)$ is the Bessel function of the first kind and order 1, $Y_1(.)$ is the Bessel function of the second kind and order 1, A_1 and A_2 are arbitrary constants determined from the boundary conditions. Applying the first boundary condition stated in Eq. (3.10) to Eq.(3.20) yields

$$\hat{u}_1(0) = A_1 J_1(0) + A_2 Y_1(0) = 0 \tag{3.21}$$

Because $J_1(0) = 0$ and $Y_1(0) = \infty$, A_2 is zero. Now, applying the second boundary condition to Eq.(3.13)

$$T_{11}(R) = A_1 \frac{\partial J_1(R\gamma)}{\partial x_1} + A_1 \frac{v}{R} J_1(R\gamma) - \frac{e_{31} E_3}{c_{11}^E} = 0 \tag{3.22}$$

Solving for A_1 yields

$$A_1 = \frac{1}{c_{11}^E} \frac{e_{31} E_3}{\gamma J_o(R\gamma) + (v-1) R^{-1} J_1(R\gamma)} \tag{3.23}$$

Hence, the general solution is

$$u_1(t, x_1) = A_1 J_1(\gamma x_1) e^{i\omega t} \tag{3.24}$$

The mechanical resonances of the transducers can also be obtained from Eq.(3.23) by setting the electrical term to zero and solving the eigenvalue equation. Similar results have been reported in the existing literature [47].

Electromechanical response: To determine the EM response, the total charge flow between the top and bottom surface electrodes needs to be calculated by integrating the electrical displacement in Eq.(3.15) over the electrode area as:

$$Q = \int_A D_3 x_1 dx_2 dx_1 = \pi R^2 \varepsilon_{33}^T \hat{E}_3 \left[1 + 2 \frac{A_1 J_1(\gamma R)}{\hat{E}_3 \varepsilon_{33} R} \right] e^{i\omega t} \tag{3.25}$$

The net charge can be expressed in terms of the electrical capacitance, the potential voltage, and the planar EM coupling factor $k_p^2 = 2\,e_{31}^2 / c_{11}^E \varepsilon_{33}^T$ as:

$$Q = C\hat{V}\left[1 + \frac{k_p^2}{e_{31}} \frac{J_1(R\gamma)}{R\gamma J_o(R\gamma) + (\nu - 1) J_1(R\gamma)}\right] e^{i\omega t} \tag{3.26}$$

Differentiating Eq.(3.26) with respect to time yields the electric current and dividing the electric voltage by the electric current yields the impedance.

$$Z = \frac{\hat{V}}{\hat{I}} = \frac{1}{i\omega C}\left[1 + \frac{k_p^2}{e_{31}} \frac{J_1(R\gamma)}{R\gamma J_o(R\gamma) + (\nu - 1) J_1(R\gamma)}\right]^{-1} \tag{3.27}$$

The EM response of the circular piezoelectric transducer is governed by the impedance expression. While varying the frequency of the alternating electrical voltage, the impedance response indicates the locations of resonances and anti-resonances. Finding the zeros of Eq.(3.27) yields the EM resonant frequencies whereas the poles of Eq.(3.23) yield the mechanical resonant frequencies. Both have the same eigenvalue equation resulting in identical mechanical and EM resonances.

$$R\gamma J_o(R\gamma) + (\nu - 1) J_1(R\gamma) = 0 \tag{3.28}$$

For the sake of completeness, the first three eigenvalues and mode shapes are given in here for a Poisson's ratio of 0.35.

$$U_{1n}(x_1) = J_1\left(\frac{\omega_n}{c_p} x_1\right), \qquad \frac{\omega_n}{c_p} = \frac{1}{R}(2.0795,\ 5.3989\ ,8.5778,....) \tag{3.29}$$

As may be noted from Eq.(3.27), the EM resonances merely depend on structural and geometrical properties of the transducer and are not affected by the EM material properties. The EM material properties primarily influence the magnitude of the response.

3.1.2. Finite element analysis

In addition to analytical formation, a 3D numerical simulation was also implemented in ANSYS to determine the piezoelectric harmonic response of a free circular transducer. The transducer has a diameter of 6 mm and a thickness of 0.25 mm with material polarization in z-direction for structural and EM material properties included in Table 1 of the Appendix. The piezoelectricity of the transducer was simulated by conducting a multiphysics analysis that couples electrical field and mechanical field simultaneously in the solution process. The circular transducer was meshed with a coupled-field element, SOLID226, which has 20 nodes and a maximum of five degrees of freedom, see Figure 3.3. The piezoelectricity option was activated so that each node has four degrees of freedom including the voltage and the displacements in the global coordinate system.

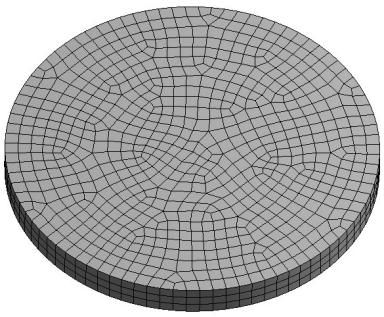

Figure 3.3: A circular piezoelectric transducer meshed with coupled-field elements.

To simulate the free response, there were no structural loads applied to the transducer. A coupling voltage was applied on the top and bottom surface of the

transducer to create the electrodes by coupling the voltage degree of freedom for all nodes on the top and the bottom area separately. Next, the transducer was subjected to a harmonic voltage applied on the surface electrodes with a constant magnitude. The frequency sweep of the applied voltage was from 10 kHz to 1.6 MHz which is expected to contain the first three EM resonances, and thus the same frequency range was used to produce the analytical and experimental results for comparison in the next sections.

3.1.3. Experimental setup

A simple fixture constructed to hold the specimen is shown in Figure 3.4a. The fixture has two bolts connected to a couple of springs that functions as a c-clamp allowing any necessary adjustment to the pressure on the specimen and the jaw gap. The specimen was placed between the end-tips of two bolts that gently touching the specimen under test. A $100\,\Omega$ resistor was placed in series to the specimen and connected to a wave generator at the other terminal. A schematic diagram of the electrical circuit is shown in Figure 3.4b. The impedance was calculated by the following expression:

$$Z = R_s \frac{V_i}{V_o} \tag{3.30}$$

In Eq.(3.30), Z is the electrical impedance, R_s is a constant resistance, V_i is the voltage applied to the circuit, and V_o is the voltage across the sensing resistor and the PZT element. A MDO3014 Mixed Domain Oscilloscope manufactured by Tektronix was used to obtain voltage measurements across the specimen and the entire circuit. The tone burst signal in frequency sweep mode transmitted to the specimen was generated by a KEYSIGHT 33500B Series wave generator. The alternating voltage was continuously

varying from the start frequency to the stop frequency. Five round piezoelectric elements (APC-850) that were tested have an average diameter of 6 mm and thickness of 0.25 mm. They were tested by sweeping alternating voltage frequency from 10 kHz to 1.6 MHz. The voltage measurements collected from the oscilloscope have been processed to generate the piezoelectric response, voltage amplitude versus frequency diagram.

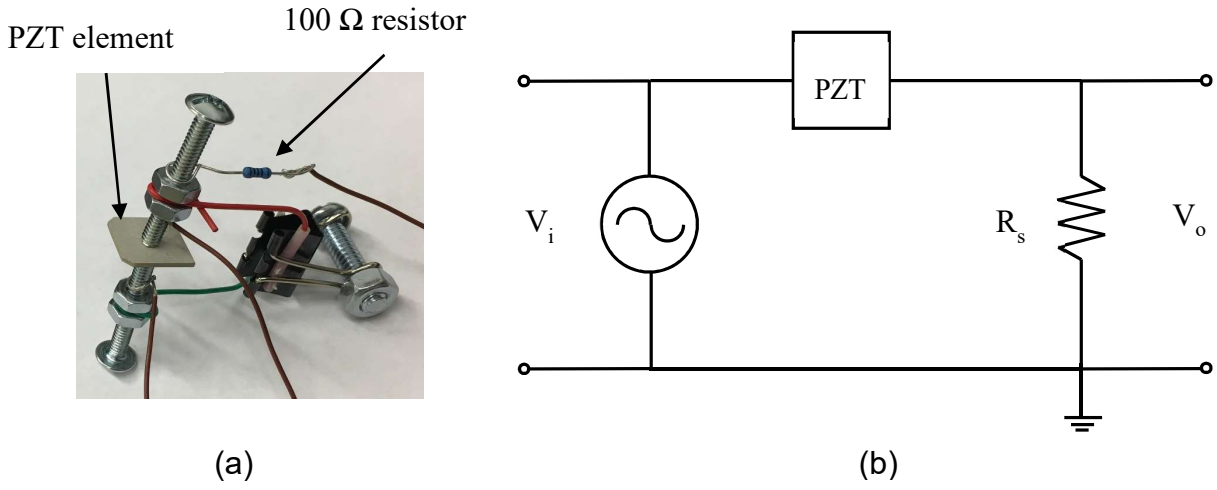

Figure 3.4: a) Experimental setup and PZT element under test; b) electrical circuit for approximating PZT impedance [48].

Signal processing: To process the signal obtained from testing, the generated signal in time domain is first transformed into the frequency domain by applying the Fast Fourier Transform algorithm. A band-pass filter based on a window function is designed to attenuate the end effects that caused by a quick change in frequency at the start frequency, ω_{st} , and at the stop frequency, ω_{sp} of each frequency sweep. The band-pass filter response represents the response-sum of high-pass (HP) filter and low-pass (LP) filter [49].

$$H_d(e^{i\omega}) = \begin{cases} e^{-j\omega n}, & \omega_{st} \le |\omega| \le \omega_{sp} \\ 0, & |\omega| \le \omega_{st} \\ 0, & \omega_{sp} \le |\omega| \le \pi \end{cases} \tag{3.31}$$

In Eq.(3.31), H_d is the desired filter response. A Kaiser window was integrated into the filtering process. The coefficients of a Kaiser window were determined by [49]

$$W(n) = \frac{I_o\left(\beta\sqrt{1-\frac{4n^2}{(N-1)^2}}\right)}{I_o(\beta)}, \qquad -\frac{(N-1)}{2} \le n \le \frac{(N-1)}{2} \tag{3.32}$$

In Eq.(3.32), N is the number of sampling points, I_o is the modified 0th order Bessel function of the first kind, and β is the attenuation parameter. A Kaiser window was selected because it uses an attenuation parameter that is able to control the decay rate as well as the magnitude of the side peaks. The signal was then de-noised using wavelet transform in order to enhance the signal resolution. The continuous wavelet transform of a function, $f(x)$, with independent space variable, *x*, can be defined as [50]:

$$C(u,s) = \frac{1}{\sqrt{s}} \int_{-\infty}^{\infty} f(x)\psi\left(\frac{x-u}{s}\right)dx \tag{3.33}$$

In Eq.(3.33), $C(u,s)$ are the wavelet coefficients and ψ is the analyzing wavelet. The function, $f(x)$ is decomposed by the mother wavelet, ψ that is translated/shifted by a factor of *u* and dilated/scaled by a factor of *s*. In practice, the discrete wavelet transform was used to transform a discrete signal to discrete wavelet coefficients in the wavelet domain. The de-noising process was conducted by decomposing the signal into wavelet coefficients using Coifl4 at level 9. It should be mentioned that there are many possible

choices of the analyzing wavelet ψ, unlike Fourier Transform that is limited to a single basis, $e^{j\omega t}$. The wavelet coefficients generated in the wavelet domain are comprised of detailed coefficients (HP filter outputs) and approximation coefficients (LP filter outputs). Finally, applying the universal threshold to detail coefficients and then reconstructing the signal using the original approximation coefficients and the processed detail coefficients yields the results presented in the next section.

3.1.4. Results and Discussion

The results of a circular piezoelectric transducer obtained from the analytical, FE and experimental approaches are discussed in this section. Table 3-1 summarizes the EM resonances of the first three modes and the percent difference in FE and analytical results compared to experimental results. Since the experimental results represent the actual solution, they were used as a benchmark to compare other results with. There is about 0.73% difference between the experimental and the analytical first resonant frequency. However, the second and the third experimental resonant frequencies are reported below the theoretical ones with a maximum difference of about 3%. On the other hand, the resonant frequencies of FE approach included in Table 3-1 are determined slightly lower than the experimental resonant frequencies. Overall, the experimental results are in good agreement with theoretical calculations and numerical solutions.

Table 3-1: Results summary of electromechanical resonances for a circular APC-850 piezoelectric element: closed-form, experiment, and FE.

Mode	Closed-form	Experiment	Error	FE	Error
#	kHz	kHz	%	kHz	%
1	343.1	345.6	0.73	329.7	4.6
2	890.8	883.56	0.81	847.8	4.05
3	1415	1371.8	3.15	1328	3.12

As previously mentioned, five circular APC-850 transducers were tested for natural resonances and the statistics of the first three EM resonances are listed in Table 3-2. The experimental results were found to be more consistent with smaller standard deviations than the manufacturer specifications for the same product. As per APC International, the capacitance and the frequency have manufacturing tolerances of ±20% and ±5%, respectively. It is expected that the underlying contributors to the standard deviations calculated in Table 3-1 especially for higher modes are the machining and electrical tolerances. The diameter and thickness of the specimens have machining tolerances of ±0.25 mm and ±0.025 mm, respectively. As may be noted from Table 3-2, the standard deviation is relatively small compared to the mean values and the difference between the extreme values.

Table 3-2: Experimental results summary of EM resonances for five circular APC-850 piezoelectric samples.

Mode	Mean	Standard deviation	Maximum	Minimum
#		kHz		
1	345.6	3.1	348.4	341.7
2	883.5	6.6	889.4	875.3
3	1371.8	10.2	1383.1	1359.1

The impedance diagram of a circular piezoelectric transducer was calculated using Eq.(3.27) and displayed in Figure 3.5. The frequency response shows the first three planar EM resonances at which the impedance is low while the electric current drawn by the piezoelectric transducer is maximum. The experimental response shown in Figure 3.5 also indicates the locations of EM resonances at low potential voltage values. Similar outcomes have been also observed from the FE response which agrees well with the experimental and the analytical response, see Figure 3.5.

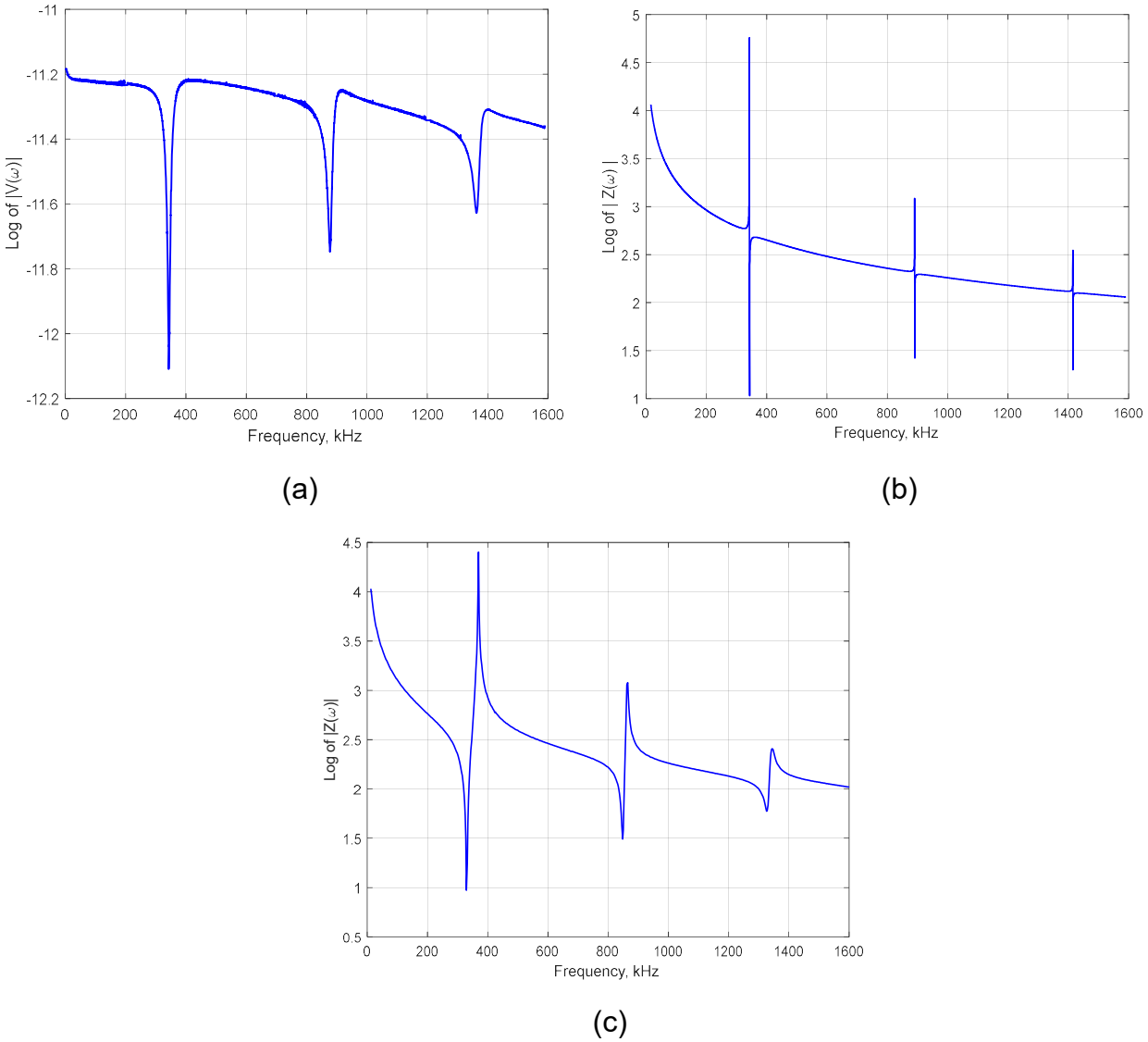

Figure 3.5: Piezoelectric response of a circular transducer: a) experiment, b) analytical, c) simulation.

It should be noted that the anti-resonances which happen at high impedance and high voltage are also present in the impedance response. The gap difference between the resonances and anti-resonances is shrinking and becoming negligible for higher modes. A piezoelectric transducer has better performance at its natural resonances, but due to stability region being too narrow that may be causing some difficulty to maintain the transducer operating at natural frequencies. Finally, the EM mode shapes of a circular

transducer were obtained from a 2D FE modal analysis and are displayed in Figure 3.6. It shows the radial axisymmetric deformation at the EM resonant frequencies.

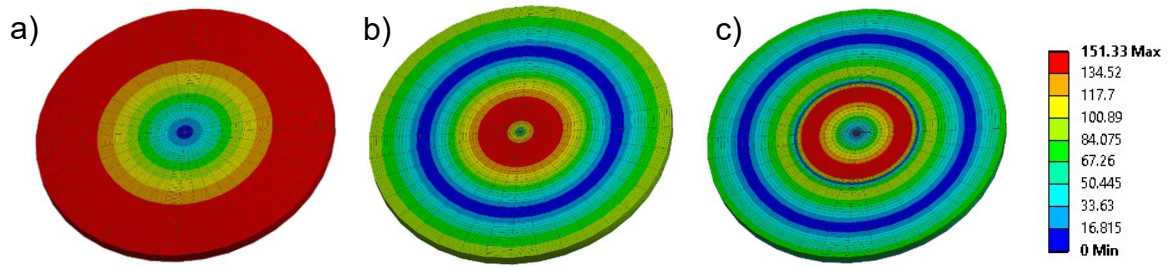

Figure 3.6: Finite element EM mode shapes of a circular PZT: a) first mode, b) second mode, and c) third mode.

3.2. Rectangular Piezoelectric Transducer

A conventional rectangular piezoelectric transducer is considered here to study the piezoelectric response by varying the frequency of electric voltage applied to the transducer. In Figure 3.7, the transducer with a thickness polarization has a length l, width w, and thickness h. The material properties of the transducer are given in Table 1 of the Appendix. This section focuses on modeling the behavior of a rectangular transducer analytically as well as performing a 3D numerical analysis and experimental testing for purposes of comparison.

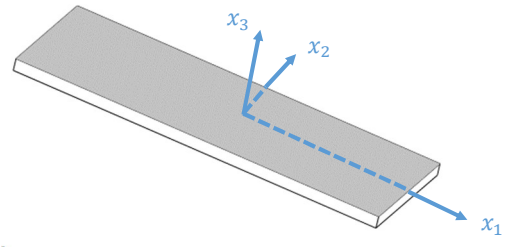

Figure 3.7: Schematic of a standard piezoelectric transducer polarized in x_3 - direction.

3.2.1. Analytical model

The piezoelectric transducer is expected to have a predominant axial motion in x_1- direction by assuming the ratios of length to width and width to thickness are relatively large causing uncoupled motion among the principal axes of the transducer. This assumption renders the problem into 1D analysis and yields the following stress formulation of the piezoelectric constitutive equations:

$$T_{11} = c_{11}^{E} S_{11} - e_{31} E_3 \tag{3.34}$$

$$D_3 = e_{31} S_{11} + \varepsilon_{33}^{T} E_3 \tag{3.35}$$

In Eq.(3.34) and Eq.(3.35), S_{11} is the longitudinal strain in x_1- direction, e_{13} is the piezoelectric stress coupling coefficient, i.e., electrical field E_3, applied in x_3- direction induces mechanical stress T_{11}, in x_1- direction. The harmonic voltage applied on the electrodes of the transducer is assumed to induce uniform electrical field over the transducer, thus the electric field is independent of x_1- direction, i.e., $\partial E_3 / \partial x_1 = 0$. Since the voltage applied is harmonic, the electric field and the general response are also harmonic.

$$V(t) = \hat{V} e^{i\omega t} \tag{3.36}$$

$$E_3(t) = \hat{E}_3 e^{i\omega t} \tag{3.37}$$

$$u_1(t, x_1) = \hat{u}_1(x_1) e^{i\omega t} \tag{3.38}$$

Because the transducer has stress-free boundaries, the structural boundary conditions for this problem can be defined as:

$$T_{11}(l/2)=0$$
$$T_{11}(-l/2)=0 \tag{3.39}$$

Application of Newton's second law on an infinitesimal element of the piezoelectric transducer shown in Figure 3.8 yields the equation of motion

$$\frac{\partial T_{11}}{\partial x_1}=\rho\frac{\partial^2 u_1}{\partial t^2} \tag{3.40}$$

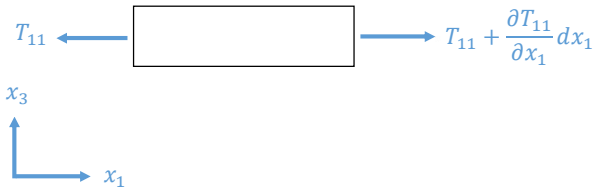

Figure 3.8: Infinitesimal axial element in Cartesian coordinate system.

Recall the stress-strain relation,

$$S_{11}=\frac{\partial u_1}{\partial x_1} \tag{3.41}$$

Substitution of Eq.(3.41) into Eq.(3.34) and Eq.(3.35) yields

$$T_{11}=c_{11}^{E}\frac{\partial u_1}{\partial x_1}-e_{31}E_3 \tag{3.42}$$

$$D_3=e_{31}\frac{\partial u_1}{\partial x_1}+\varepsilon_{33}^{T}E_3 \tag{3.43}$$

Using the general solution in Eq.(3.38) and substituting Eq.(3.42) into Eq.(3.40) gives the wave equation

$$\frac{\partial^2 \hat{u}_1}{\partial x_1^2} = -\frac{\omega^2}{c_p^2}\hat{u}_1 \tag{3.44}$$

The pressure wave speed c_p in the piezoelectric material is defined as:

$$c_p = \sqrt{\frac{c_{11}^E}{\rho}} \tag{3.45}$$

The wavenumber can be expressed as:

$$\gamma = \frac{\omega}{c_p} \tag{3.46}$$

Introducing the wavenumber into Eq.(3.44) yields

$$\frac{\partial^2 \hat{u}_1}{\partial x_1^2} = -\gamma^2 \hat{u}_1 \tag{3.47}$$

This is a second order ODE and has a general solution commonly expressed in this form:

$$\hat{u}_1(x_1) = A_1 \cos(\gamma x_1) + A_2 \sin(\gamma x_1) \tag{3.48}$$

In Eq.(3.48), A_1 and A_2 are arbitrary constants to determine from the application of boundary conditions. Applying the boundary conditions given in Eq.(3.39) to Eq.(3.42) yields a system of algebraic equations in a matrix form

$$\begin{bmatrix} -\sin(\gamma l/2) & \cos(\gamma l/2) \\ \sin(\gamma l/2) & \cos(\gamma l/2) \end{bmatrix} \begin{bmatrix} A_1 \\ A_2 \end{bmatrix} = \begin{bmatrix} e_{31}\hat{E}_3 / \gamma c_{11}^E \\ e_{31}\hat{E}_3 / \gamma c_{11}^E \end{bmatrix} \tag{3.49}$$

Solving the system of linear equations, the constants can be expressed as:

$$\begin{aligned} A_1 &= 0 \\ A_2 &= \frac{e_{31}\hat{E}_3}{\gamma c_{11}^E \cos(\gamma l/2)} \end{aligned} \tag{3.50}$$

Thus, the general solution is given as:

$$u_1(t,x_1)=\frac{e_{31}\hat{E}_3}{\gamma c_{11}^E\cos(\gamma l/2)}\sin(\gamma x_1)e^{i\omega t} \tag{3.51}$$

Electromechanical response: Integration of the electric displacement given in Eq.(3.43) over the electrode area yields the total charge, Q

$$Q=\left[2e_{31}A_1\sin(l\gamma/2)+l\varepsilon_{33}\hat{E}_3\right]be^{i\omega t} \tag{3.52}$$

The total charge can be expressed in terms of the electric voltage given in Eq.(3.36), as well as the transducer electric capacitance, $C=\varepsilon_{33}^T A/h, A=bl$, and the EM coupling factor $k_{31}^2=e_{31}^2/c_{11}^E\varepsilon_{33}^T$, to be as follows:

$$Q=C\hat{V}\left[k_{31}^2\frac{\tan(l\gamma/2)}{l\gamma/2}+1\right]e^{i\omega t} \tag{3.53}$$

Differentiation of the net charge with respect to time yields the electric current and dividing Eq.(3.36) by the electric current yields the impedance, Z.

$$Z=\frac{1}{i\omega C}\left[k_{31}^2\frac{\tan(l\gamma/2)}{l\gamma/2}+1\right]^{-1} \tag{3.54}$$

Eq.(3.54) predicts the impedance response of the piezoelectric transducer as well as the locations of the EM resonances and anti-resonances. By finding the zeros of Eq.(3.54), it produces the eigenvalues which are the EM resonances. Thus, the normalized mode shapes of the transducer at the EM resonances can be stated in a closed-form expression.

$$U_{1n}^{EM} = \sin\left(\frac{n\pi}{l}x_1\right), \quad \omega_n = \frac{n\pi c_p}{l}, \quad n = 1,3,5,... \tag{3.55}$$

The mechanical modes which comprised of symmetric modes and antisymmetric modes can be determined from Eq.(3.49) by solving the homogeneous system of equations for nontrivial solutions. For the sake of completeness, the normalized symmetric and antisymmetric mode shapes are given below.

$$U_{1n}^{S} = \cos\left(\frac{m\pi}{l}x_1\right), \quad \omega_m = \frac{m\pi c_p}{l}, \quad \mathrm{m} = 2,4,6,... \tag{3.56}$$

$$U_{1m}^{A} = \sin\left(\frac{n\pi}{l}x_1\right), \quad \omega_n = \frac{n\pi c_p}{l}, \quad n = 1,3,5,... \tag{3.57}$$

It is worth noting from Eq.(3.55) and Eq.(3.57) that the EM modes and the antisymmetric modes are the same indicating that piezoelectric resonances are independent of piezoelectric properties.

3.2.2. Finite element analysis

A simulation of rectangular piezoelectric transducer was also conducted to obtain the EM response when it is subjected to a harmonic voltage at a constant magnitude. The rectangular transducer has average dimensions of 13 mm x 3 mm x 0.3 mm and was polarized in the z - direction. Due to only geometrical difference between the rectangular and the circular transducer, the same boundary conditions and material properties applied in the analysis of a circular transducer were also applied to this analysis. In Figure 3.9, SOLID226 element with four degrees of freedom was also used to mesh the model for

multiphysics analysis. The frequency sweep of the electric voltage applied on the top and bottom electrodes was from 10 kHz to 700 kHz with 1.5 kHz increment.

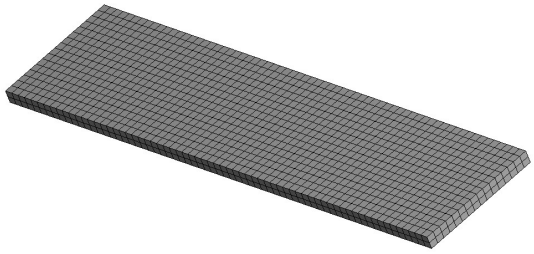

Figure 3.9: A rectangular piezoelectric transducer meshed with coupled-field elements.

3.2.3. Experimental test

The same experimental setup used to test the circular specimens in Section 3.1.3 was also implemented for conventional rectangular specimens. The fixture was adjusted to have sufficient gap open with little pressure applied on the specimen to hold it steady in place. Five rectangular APC-850 piezoelectric elements with dimensions of 13 mm x 3 mm x 0.3 mm were purchased from APC International, Ltd. These dimensions were carefully selected to make sure that the assumption made to produce the analytical results is reasonably valid when the results of closed-form analysis and FE method are compared. The frequency sweep mode was selected to apply the alternating voltage with continuously increasing frequency from 10 kHz to 700 kHz. The collected voltage measurements across the specimen were processed to produce the EM response using the algorithm developed in Section 3.1.3.

3.2.4. Results and discussion

The EM resonant frequencies obtained using the three methods discussed in the previous sections and the percent difference calculated with respect to the experimental

results are listed in Table 3-3. The statistical results for testing five rectangular piezoelectric transducers are summarized in Table 3-4. It can be noted that the experimental resonances were found higher than FE resonances of the first three modes with a maximum difference of about 2.6%.

Table 3-3: Results summary of EM resonances for a rectangular APC-850 piezoelectric element: closed-form, experiment, and FE.

Mode	Closed-form	Experiment	Error	FE	Error
#	kHz	kHz	%	kHz	%
1	111.5	111.1	0.34	108.5	2.36
2	334.6	319.8	4.60	311.5	2.62
3	557.7	526.4	5.94	512.7	2.61

Table 3-4: Experimental results summary of EM resonances for five rectangular APC-850 piezoelectric samples.

Mode	Mean	Standard deviation	Maximum	Minimum
#		kHz		
1	111.1	1.08	112.1	109.7
2	319.8	2.33	323.5	317.2
3	526.4	4.8	534.1	522.9

On the other hand, the analytical resonances were predicted higher than experimental resonances with a maximum difference of about 5.9%. A possible reason for this difference is the geometrical dimensions of the samples caused the assumption that was made to simplify the analytical analysis into 1D problem less accurate. This finding was further verified by comparing the experimental results in Table 3-3 against the FE results which has been produced from a 3D harmonic analysis. The maximum difference between the actual and the FE resonances is less than 3%. Furthermore, the experimental impedance response in Figure 3.11 supports this conclusion with several resonances including the first three longitudinal modes being present over the

predetermined frequency sweep. Therefore, a better agreement between the analytical analysis and experiment can be reached by choosing a larger length to width ratio in order to assure decoupled-motions among the major system coordinates.

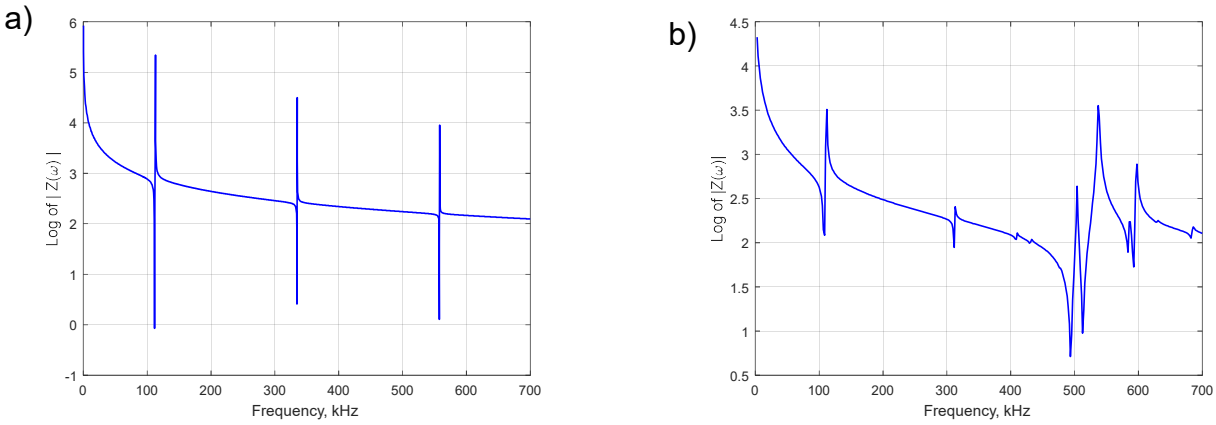

Figure 3.10: Piezoelectric response of a rectangular PZT: a) analytical model and b) simulation.

By inspecting the piezoelectric response in Figure 3.10 and Figure 3.11, the analytical impedance response shows the first three EM resonances along the transducer length, whereas the experimental response contains all possible resonances along the major coordinates. It can be noted that the experimental and 3D FE response contain about the same number of EM resonances at similar locations. To identify these resonances according to their directions of motion, the piezoelectric response of a FE harmonic analysis was compared with the experimental response by retrieving the mode shapes at each resonance in Figure 3.10b.

Experimental response of a rectangular PZT is given Figure 3.11 with annotations defining the locations of EM resonances based on 3D FE analysis as: l_n - longitudinal mode, w - width mode, T_x - twisting mode about x axis, T_z - twisting mode about z axis, and C_m - coupled mode. The response in Figure 3.11 shows two twisting modes and a

width mode take place right before the third longitudinal resonance and a coupled mode at about 600 kHz. Some of these results have been also verified analytically but not included in here. For instance, the first width resonance was determined for the same sample dimensions and predicted a little lower than the third longitudinal resonance. The first three EM mode shapes based on FE modal analysis are displayed in Figure 3.12.

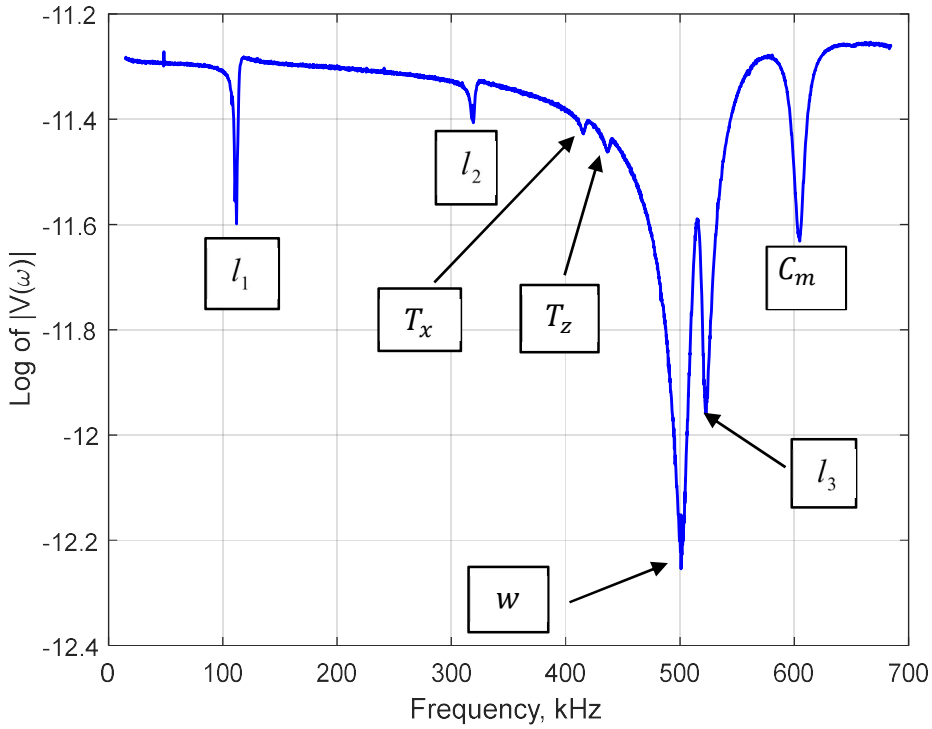

Figure 3.11: Experimental response of a rectangular PZT with annotations defining the locations of EM resonances based on 3D FE analysis.

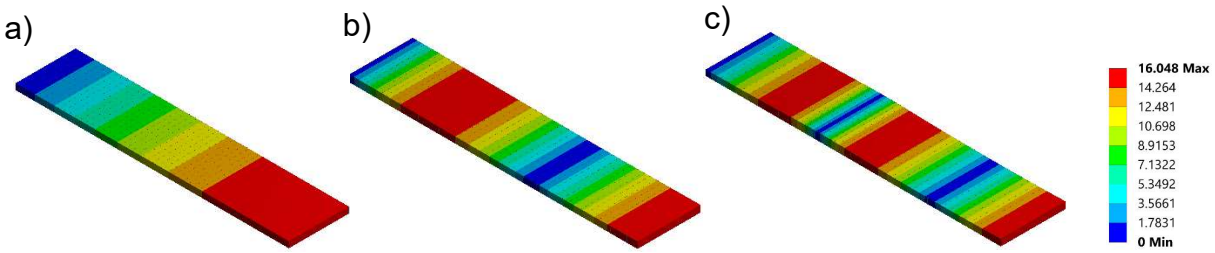

Figure 3.12: FE electromechanical mode shapes of a d31 PZT: a) first mode, b) second mode, and c) third mode.

3.3. Shear-mode Piezoelectric Transducer

This section discusses the harmonic response of a shear-mode piezoelectric transducer that is polarized in x_1 - direction. In Figure 3.13, the transducer is excited with electric voltage applied on the top and bottom electrodes causing the transducer periodically oscillates in accordance with the frequency of the induced electric field, E_3. The transducer with material properties listed in Table 1 of the Appendix has length l, width *w*, and thickness *h*. In here, the study focuses on determining a closed-form solution of the piezoelectric response including the impedance and EM responses and then comparing the results with a 3D FE simulation and experimental results.

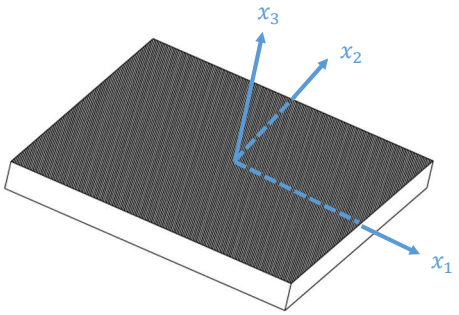

Figure 3.13: Shear-mode piezoelectric transducer polarized in x_1 - direction.

3.3.1. Analytical model

For a piezoelectric transducer polarized in x_1 - direction with electric field induced in x_3 - direction, the transducer is assumed to have a predominant shear motion in $x_1 - x_3$ plane and decoupled shear strains among the principal planes. The shear strain is assumed to be uniform along the transducer length. This implies that the derivative with respect to x_1 is zero, i.e. $\partial(.)/\partial x_1$. The volume of the transducer in vibration remains substantially

constant meaning that expansion in longitudinal direction must always accompanied by contraction in the transverse direction and vice versa. These assumptions render the problem into 2D analysis and yield the constitutive equations in Eq.(3.1) and Eq.(3.2) to be simplified as:

$$T_5 = c_{55}^E S_5 - e_{35} E_3 \tag{3.58}$$

$$D_3 = e_{35} S_5 + \varepsilon_{33}^T E_3 \tag{3.59}$$

In Eq.(3.58) and Eq.(3.59), T_5 is the shear stress in $x_1 - x_3$ plane, S_5 is the mechanical shear strain in $x_1 - x_3$ plane, c_{55}^E is the stiffness coefficient, e_{35} is the stress coupling constant between electric field applied in x_3- direction and mechanical shear strain in $x_1 - x_3$ plane. As per stiffness-compliance relation,

$$c_{55}^E = \frac{1}{s_{55}^E} \tag{3.60}$$

In Eq.(3.60), s_{55}^E is the shear compliance coefficient, and for a transversely isotropic material, $s_{55}^E = s_{44}^E$. Since the applied voltage on the piezoelectric transducer induces a shear motion normal to the direction of the electric field, this means the electric field confined between the electrodes changes with respect time and space, i.e. $\partial E_3 / \partial x_3 \neq 0$. As a result of a harmonic voltage, the electric field and the general response are also harmonic and can be expressed as:

$$V(t) = \hat{V} e^{i\omega t} \tag{3.61}$$

$$E_3(t, x_3) = \hat{E}_3(x_3) e^{i\omega t} \tag{3.62}$$

$$u_1(t, x_3) = \hat{u}_1(x_3) e^{i\omega t} \tag{3.63}$$

Because the transducer has stress-free boundaries and the voltage across the transducer is the same as the applied voltage, the mechanical and electrical boundary conditions of a free piezoelectric transducer can be stated as follows:

$$\begin{aligned} &T_{13}(h/2) = 0 \\ &T_{13}(-h/2) = 0 \\ &V_E(h/2) - V_E(-h/2) = \hat{V} e^{i\omega t} \end{aligned} \tag{3.64}$$

In Eq.(3.64), V_E is the electric potential, and $\hat{V}$ is the magnitude of electric voltage. Application of Newton's second law on an infinitesimal element of a shear-mode piezoelectric transducer shown in Figure 3.14 in x_1 - direction yields the equation of motion

$$\frac{\partial T_{31}}{\partial x_3} = \rho \frac{\partial^2 u_1(x_3)}{\partial t^2} \tag{3.65}$$

In Eq.(3.65), T_{31} is the shear stress and ρ is the material density. Differentiation of the general solution in Eq.(3.63) and using shear stress in matrix notation (Voigt notation), i.e. $T_{31} = T_5$, yields

$$\frac{\partial T_5}{\partial x_3} = -\rho \omega^2 u_1 \tag{3.66}$$

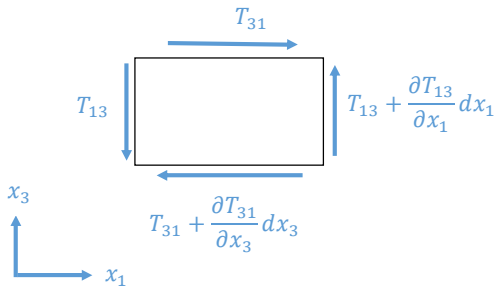

Figure 3.14: Infinitesimal shear element.

From stress-strain relation, the shear strain tensor in $x_1 - x_3$ plane can be written in terms of displacement,

$$S_{31} = \frac{1}{2}\left(\frac{\partial \hat{u}_1}{\partial x_3} + \frac{\partial \hat{u}_3}{\partial x_1}\right) \tag{3.67}$$

Since the shear strain is uniform, the derivative with respect to x_1 is zero, i.e., $\partial u_3 / \partial x_1 = 0$. Also, the total shear strain S_5 is twice the shear strain tensor, i.e., $S_5 = 2S_{13}$. Simplifying the stress-strain relation yields

$$S_5 = 2S_{31} = \frac{\partial \hat{u}_1}{\partial x_3} \tag{3.68}$$

The electric potential and electric field relation is

$$E_3 = -\frac{\partial V_E}{\partial x_3} \tag{3.69}$$

Substitution of Eq.(3.68) and Eq.(3.69) into Eq.(3.58) and Eq.(3.59) yields

$$T_5 = c_{55}^E \frac{\partial \hat{u}_1}{\partial x_3} + e_{35} \frac{\partial V_E}{\partial x_3} \tag{3.70}$$

$$D_3 = e_{35}\frac{\partial u_1}{\partial x_3} - \varepsilon_{33}^T \frac{\partial V_E}{\partial x_3} \tag{3.71}$$

Differentiation of the shear stress and electric displacement with respect x_3 yields

$$\frac{\partial T_5}{\partial x_3} = c_{55}^E \frac{\partial^2 u_1}{\partial x_3^2} + e_{35}\frac{\partial^2 V_E}{\partial x_3^2} \tag{3.72}$$

$$\frac{\partial D_3}{\partial x_3} = e_{35}\frac{\partial^2 u_1}{\partial x_3^2} - \varepsilon_{33}^T \frac{\partial^2 V_E}{\partial x_3^2} = 0 \tag{3.73}$$

Because shear strain only depends on x_3, the surface area of the electrodes remains constant. This also means the electric displacement remains constant, i.e., $\partial D_3 / \partial x_3 = 0$. Substituting Eq.(3.73) into Eq.(3.72) and then substitute the resulting equation into the equation of motion yields the wave equation

$$\frac{\partial^2 \hat{u}_1}{\partial x_3^2} = -\frac{\omega^2}{c_s^2}\hat{u}_1 \tag{3.74}$$

The shear wave speed c_s in the material is defined as:

$$c_s = \sqrt{\frac{\overline{c}_{55}}{\rho}} \tag{3.75}$$

and

$$\overline{c}_{55} = c_{55}^E + \frac{e_{35}^2}{\varepsilon_{33}^T} \tag{3.76}$$

The wavenumber is defined as:

$$\gamma = \frac{\omega}{c_s} \tag{3.77}$$

Introducing the wavenumber to Eq.(3.74) yields

$$\frac{\partial^2 \hat{u}_1}{\partial x_3^2} = -\gamma^2 \hat{u}_1 \tag{3.78}$$

This is a second order ODE and has a general solution commonly expressed in this form

$$\hat{u}_1(x_3) = A_1 \cos(\gamma x_3) + A_2 \sin(\gamma x_3) \tag{3.79}$$

In Eq.(3.79), A_1 and A_2 are arbitrary constants and can determined by applying the boundary conditions. The electric potential can be determined by integrating Eq.(3.73) twice

$$V_E = \frac{e_{35}}{\varepsilon_{33}^T} u_1 + x_3 B_1 + B_2 \tag{3.80}$$

In Eq.(3.80), B_1 and B_2 are arbitrary constants. Due to the antisymmetric nature of the electric potential with respect to the neutral axis, B_2 is set to zero. The shear stress is maximum at the neutral axis and vanishes at the top and bottom surfaces. Thus, applying the boundary conditions stated in Eq.(3.64) to Eq.(3.70) and Eq.(3.80) yields

$$-\overline{c}_{55} A_1 \gamma \sin(\beta) + \overline{c}_{55} A_2 \gamma \cos(\beta) + e_{35} B_1 = 0 \tag{3.81}$$

$$\overline{c}_{55} A_1 \gamma \sin(\beta) + \overline{c}_{55} A_2 \gamma \cos(\beta) + e_{35} B_1 = 0 \tag{3.82}$$

$$2\frac{e_{35}}{\varepsilon_{33}} A_2 \sin(\beta) + hB_1 = \hat{V} \tag{3.83}$$

In Eq.(3.81) through Eq.(3.83), $\beta = \gamma h / 2$ and $\overline{c}_{55} = c_{55}^E + e_{35}^2 / \varepsilon_{33}^T$. Elimination of A_1 terms by adding Eq.(3.81) and Eq.(3.82) yields the following system of linear equations in a matrix form:

$$\begin{bmatrix} \overline{c}_{55}\gamma\cos(\beta) & e_{35} \\ 2\dfrac{e_{35}}{\varepsilon_{33}}\sin(\beta) & h \end{bmatrix}\begin{bmatrix} A_2 \\ B_1 \end{bmatrix}=\begin{bmatrix} 0 \\ \hat{V} \end{bmatrix} \tag{3.84}$$

Solving the system of equations, the constants can be expressed as:

$$\begin{aligned} A_2 &= \frac{-e_{35}\hat{V}}{\overline{c}_{55}\gamma h\cos(\beta)-2\dfrac{e_{35}^2}{\varepsilon_{33}^T}\sin(\beta)} \\ B_1 &= \frac{\overline{c}_{55}\gamma\hat{V}}{\overline{c}_{55}\gamma h-2\dfrac{e_{35}^2}{\varepsilon_{33}^T}\tan(\beta)} \end{aligned} \tag{3.85}$$

Therefore, the general solution is given as:

$$u_1(t,x_3) = A_2\sin(\gamma x_3)e^{i\omega t} \tag{3.86}$$

Electromechanical response: To determine the electric displacement, differentiate Eq.(3.80) and then substitute it into Eq.(3.71) yields

$$D_3 = -\varepsilon_{33}^T B_1 \tag{3.87}$$

The net charge flow between the electrodes can be determined by integrating the electric displacement over the surface area of the electrode

$$Q = -\varepsilon_{33} lb\left[\frac{\overline{c}_{55}\gamma}{\overline{c}_{55}\gamma h-2\dfrac{e_{35}^2}{\varepsilon_{33}^T}\tan(\beta)}\right]e^{i\omega t} \tag{3.88}$$

Rearranging Eq.(3.88) and expressing the total charge in terms of the electric capacitance, $C = \varepsilon_{33}^T A/h$, $A = lb$ yields

$$Q = -h\hat{V}C\left[\frac{\varepsilon_{33}^{T}\bar{c}_{55}^{E}\gamma h}{\varepsilon_{33}^{T}\bar{c}_{55}^{E}\gamma h - 2e_{35}^{2}\tan(\beta)}\right]e^{i\omega t} \tag{3.89}$$

Differentiating the net charge with respect to time and introducing the shear electromechanical coupling factor $\bar{k}_{35}^{2} = e_{35}^{2}/\varepsilon_{33}^{T}\bar{c}_{55}$ yields the electric current

$$I = i\omega\hat{V}C\left[\bar{k}_{35}^{2}\frac{\tan(\beta)}{\beta} - 1\right]^{-1}e^{i\omega t} \tag{3.90}$$

It should be noted that $\bar{k}_{35}^{2} = k_{35}^{2}/\left(k_{35}^{2}+1\right)$ and $k_{35}^{2} = e_{35}^{2}/\varepsilon_{33}^{T}c_{55}$. Therefore, dividing Eq.(3.61) by Eq.(3.90) yields the electric impedance

$$\hat{Z} = \frac{\hat{V}}{\hat{I}} = \frac{1}{i\omega C}\left[\bar{k}_{35}^{2}\frac{\tan(\beta)}{\beta} - 1\right] \tag{3.91}$$

The impedance response of the piezoelectric transducer can show the EM resonances and anti-resonances while varying the frequency of the applied voltage. Setting Eq.(3.91) to zero yields the eigenvalue equation.

$$\bar{k}_{35}^{2}\tan(\beta) - \beta = 0 \rightarrow \beta_{n}^{EM} = \beta_{1}, \beta_{2}, \beta_{3}, ... \tag{3.92}$$

The normalized mode shapes of the transducer at the EM resonant frequencies can be determined by finding the numerical solution of Eq.(3.92) for $\bar{k}_{35} = 0.59$ which yields

$$U_{1n}^{EM}(x_3) = \sin\left(\frac{\beta h}{2}x_3\right), \quad \beta^{EM} = 1.3069,\ \ 4.6364,\ \ 7.8088,... \tag{3.93}$$

It is worth noting that the system of equations in Eq.(3.81) through Eq.(3.83) can also give the mechanical response by setting the electrical terms to zero. Subtraction of Eq.(3.81) and Eq.(3.82) yields the eigenvalue equation of mechanical symmetric modes.

$$\sin(\beta) = 0 \rightarrow \beta^{sy} = n\frac{\pi}{2}, n = 2,4,6 \tag{3.94}$$

Hence, the normalized symmetric modes when $A_2 = 0$ are

$$U_{n1}^{sy} = \cos\left(\frac{\pi n}{h}x_3\right), \quad \omega_n = \frac{\pi n c_s}{h}, \quad n = 2,4,6,... \tag{3.95}$$

Addition of Eq.(3.81) and Eq.(3.82) yields the mechanical antisymmetric eigenvalue equation.

$$\cos(\beta) = 0 \rightarrow \beta^{ay} = m\pi / 2, m = 1,3,5 \tag{3.96}$$

The normalized antisymmetric modes when $A_1 = 0$ are

$$U_{m1}^{ay} = \sin\left(\frac{m\pi}{h}x_3\right), \quad \omega_m = \frac{\pi m c_s}{h}, \quad \mathrm{m} = 1,3,5,... \tag{3.97}$$

It should be noted that the EM resonances depend on the electromechanical coupling factor unlike standard piezoelectric transducers which only depend on structural properties and geometrical properties. The EM modes and mechanical antisymmetric modes are similar, but the EM resonances are predicted always higher than the mechanical antisymmetric resonances due material stiffening behavior resulting from integrating the EM material properties. Shear-modes of piezoelectric plates were studied in references [35,51,52].

3.3.2. Finite element analysis

The finite element method (FEM) is an alternative approach to analytical methods and can be used to simulate complex structures and solve problems that are very demanding and cumbersome to analyze by analytical methods. In recent years, a FEM has been

used to solve multiphysics problems. The advanced elements used in such analyses are called coupled-field elements. In this section, the multiphysics problem is a piezoelectric transducer which simulates the interaction of elastic, dynamic, and electric fields that occur simultaneously on atomic scale. The linear piezoelectricity strongly couples the equations of elasticity to the charge equations of electrostatics by piezoelectric constants.

$$\begin{Bmatrix} \{T\} \\ \{D\} \end{Bmatrix} = \begin{bmatrix} [c^E] & [e] \\ [e]^T & -[\varepsilon^T] \end{bmatrix} \begin{Bmatrix} \{S\} \\ -\{E\} \end{Bmatrix} \tag{3.98}$$

In Eq.(3.98), $\{T\}$ is the stress vector, $\{D\}$ is the electric displacement vector (also referred to as flux density vector), $[c^E]$ is the elasticity matrix at a constant electric field, $[e]$ is the piezoelectric stress matrix, $[\varepsilon^T]$ is the dielectric matrix at a constant stress, $\{S\}$ and $\{E\}$ are the elastic strain vector and the electric field intensity vector, respectively.

To model the piezoelectric response, an appropriate coupled-field element must be selected to conduct multiphysics analysis. The coupled-field element should have the capability to couple mechanical and electrical components so that change in mechanical field will induce a change in electrical field and vice versa. The FE program ANSYS was used to simulate a 3D piezoelectric transducer using a brick coupled-field element called SOLID226. Since the frequency response of the EM impedance was of interest, harmonic analysis was conducted with an alternating electric voltage. To model a shear-mode piezoelectric transducer, a square plate with the dimensions 15 mm x 15 mm x 1 mm was created and meshed using the coupling field element, SOLID226, as shown in Figure 3.15.

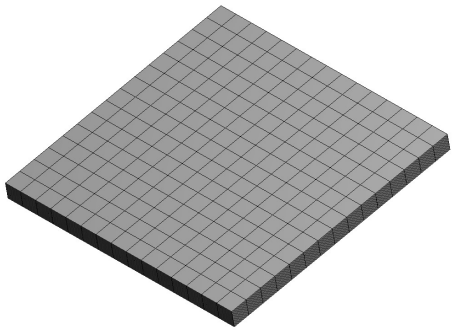

Figure 3.15: A square shear-mode PZT meshed with coupled-field elements.

In Table 1 of the Appendix, the structural and electromechanical material properties of a piezoelectric transducer polarized in x_1 - direction were used to define the elasticity matrix, the piezoelectric stress coupling constants and the permittivity matrix as in Eq.(1) of the Appendix. To simulate the EM response of a free transducer, there were no mechanical boundary conditions applied to the model. To create electric terminals on the top and bottom surfaces of the transducer, the voltage degrees of freedom for the nodes at the top surface were coupled so that all nodes were forced to take the same voltage, creating the top electrode. Similarly, a coupling voltage was also applied on the bottom nodes to create the bottom electrode. Two electrical loads in the form of electric voltage were then applied on the surface electrodes to excite the transducer with a sinusoidal alternating voltage at a frequency sweep ranging from 10 kHz to 7 MHz.

The analytical and experimental results presented in Sections 3.3.1 and 3.3.3 were also produced with the application of the same frequency sweep for comparison purposes. The piezoelectric response was expected to be primarily influenced by the number of elements across the thickness of the transducer. Therefore, a convergence analysis was carried out to assure the appropriate number of divisions. In Figure 3.16, the analysis was conducted by monitoring the third EM frequency as converging to the

correct solution while increasing the number of divisions from 3 to 15 elements. Smaller change in the frequency was noticed in the results beyond 10 elements, therefore the convergence analysis was concluded at 15 elements, and thus the numerical analysis in here was conducted with 15 divisions.

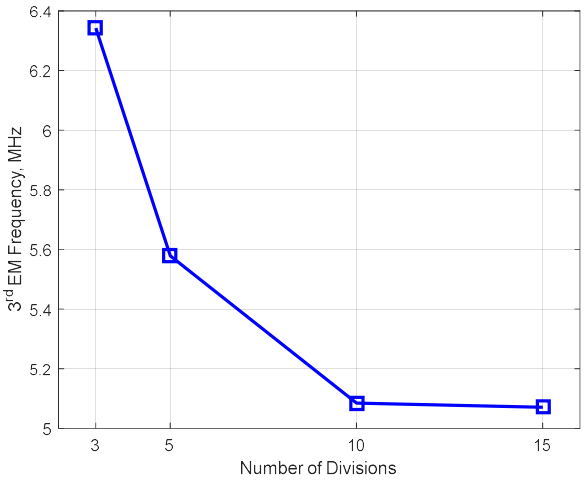

Figure 3.16: Convergence analysis of shear-mode piezoelectric transducer.

3.3.3. Experimental test

Shear-mode piezoelectric specimens were tested using the same experimental setup for the circular and rectangular specimens in Section 3.1.3. The fixture was adjusted to assure pressure-free testing while the specimen gently clamped in place to assure good electrical connection and prevent rigid body motion. Ten shear-mode piezoelectric elements with dimensions of 15 mm x 15 mm x 1 mm were tested to obtain the piezoelectric response and the locations of EM resonances. These elements were made of APC850 material (equivalent to Navy II) and manufactured by APC International, Ltd. Since the oscilloscope was limited to 10 million samples, the voltage frequency range was divided into two frequency sweeps in order to assure the piezoelectric response produced with sufficient resolution while also avoiding aliasing effects. The stop frequency

of the first sweep is the start frequency of the next sweep. The sweeping time for each frequency sweep was set to cause smooth transition while the voltage frequency increasing from the start frequency to the stop frequency. The voltage applied across the specimens was varied continuously from 10 kHz to 7 MHz. The voltage measurements collected from the oscilloscope were also processed using the same proposed algorithm in Section 3.1.3 and the results included in the next section for discussion.

3.3.4. Results and discussion

The EM resonant frequencies of a shear-mode transducer based on theoretical, experimental, and FE approach are provided in Table 3-5. The experimental resonances are the average values of ten specimens with statistical results listed in Table 3-6. The experimental results were also used as a benchmark for calculating the percent difference among other implemented methods in here. From Table 3-6, the maximum difference calculated in experimental resonances is about 10% at the third mode. Similarly, in FE results, the third mode has the maximum difference compared to the experimental resonances. It should be noted that theoretical resonances diverge from experimental ones and the difference increasing for higher modes. FE results appeared in good agreement with analytical results resulting in negligible difference in higher modes.

Table 3-5: Results summary of electromechanical resonances for a shear-mode APC-850 piezoelectric element: closed-form, experiment, and FE.

Mode	Closed-form (MHz)	Experiment (MHz)	FE (MHz)
1	0.879	0.888	0.853
2	3.028	3.139	3.001
3	5.092	5.637	5.051

Since the analytical and FE results are in a good agreement, possible reasons causing this difference in comparison to experiment could be the transducer thickness as well as

structural and electromechanical properties as these were found to be the primary parameters affecting the shear piezoelectric response. The standard thickness tolerance of a shear-mode element is ±0.05 mm and using the minimum possible thickness in the analytical analysis can significantly shift the locations of electromechanical resonances closer to the actual resonances. Furthermore, the statistics of experimental results in Table 3-6 as well as the data provided by APC International for another ten elements suggest that a patch of piezoelectric elements could have some variations in material and geometrical properties from another patch.

Table 3-6: Experimental results summary of electromechanical resonances for ten shear-mode APC-850 piezoelectric samples.

Mode	Mean	Standard deviation	Maximum	Minimum
#		MHz		
1	0.890	0.0087	0.903	0.873
2	3.139	0.0437	3.202	3.050
3	5.637	0.0504	5.692	5.569

On the other hand, the overall response of the experimental and FE approach in Figure 3.17 are comparable and show decreasing in amplitude of shear motion in higher modes. The locations of electromechanical resonances and anti-resonances can also be identified from the piezoelectric response. The FE mode shapes including the total deformation at 30 kHz are displayed in Figure 3.18. It can be noted from the natural mode shapes that the d35 PZT element undergoes almost negligible displacement at the neutral axis with sinusoidal behavior across the thickness. The analytical approach discussed in Section 3.3.1 has yielded mode shapes which are similar to the ones produced by Eq.(3.93). Additionally, the higher modes show limited displacement indicating it may not be advantageous to actuate at these frequencies. On the contrary, the actuation of d35 PZT at 30 kHz induces linear displacement across the thickness with maximum

displacement at the top surface and minimum displacement in the bottom surface. This analysis will be further discussed in the wave propagation analysis in the next chapter.

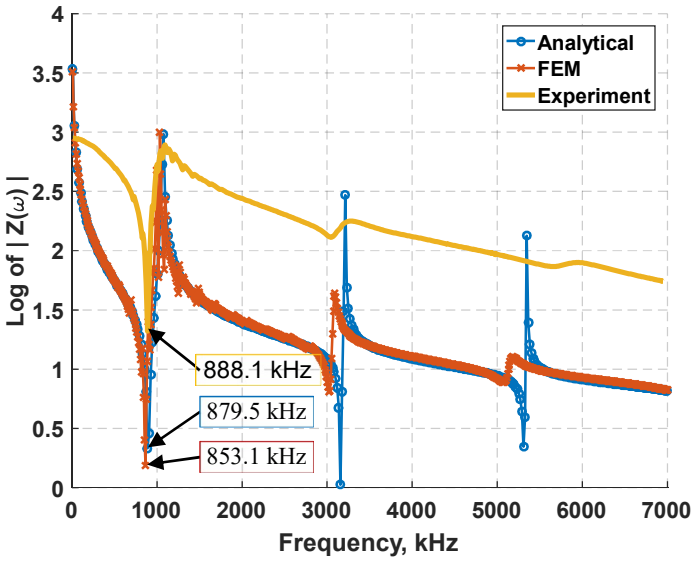

Figure 3.17: Piezoelectric response of shear-mode piezoelectric transducer.

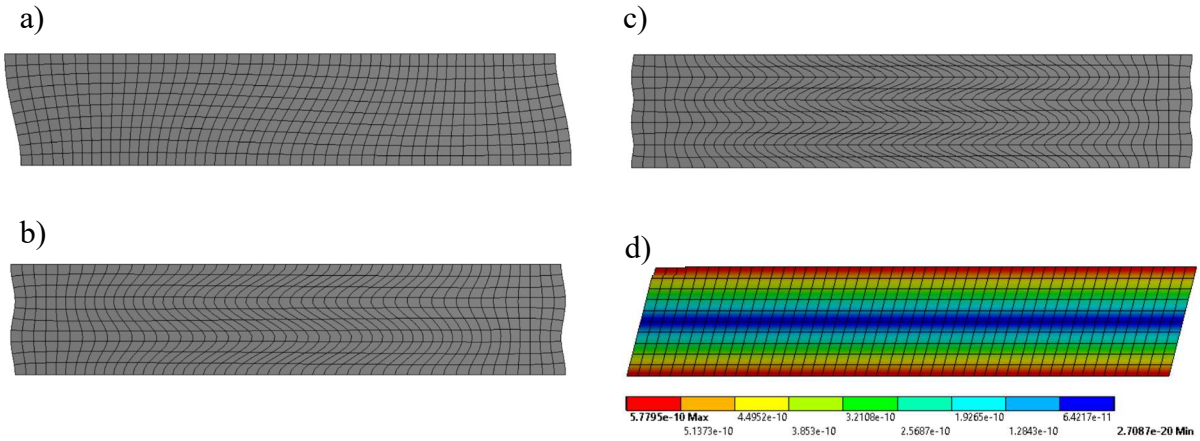

Figure 3.18: FE mode shapes of free d35 PZT element: a) first at 835 kHz; b) second at 3001 kHz; c) third at 5051 kHz; d) total deformation (mm) at 30 kHz.

3.4. Summary and Conclusions

In this chapter, three different transducers were discussed. A 2D analysis of circular transducer was conducted for electromechanical response and a closed-form expression for the impedance response. An experiment using five circular elements was performed

and the collected data were processed to obtain the piezoelectric response. A FE simulation based on multiphysics analysis was also performed and the obtained results were compared with experimental and analytical results. A rectangular transducer was analyzed based on 1D analysis and compared with experimental results obtained from five specimens. A numerical simulation using 3D coupled-field analysis was created and the impedance response of a rectangular transducer was determined. For a shear-mode piezoelectric transducer, a closed-form expression of the impedance response was derived based on 2D analysis and the solutions were compared with a 3D numerical models and experimental results.

It was found that the EM resonant frequencies of a d31 circular and rectangular PZT transducers are independent of EM material properties and only influenced by geometrical and structural material properties. The EM resonant frequencies of a shear-mode transducer depend on geometrical and structural material properties as well as EM material properties, specifically the shear piezoelectric coupling factor. Thus, it should be noted the piezoelectric coupling factor of a shear-mode transducer can be determined from the EM resonances as well.

For a circular d31 PZT transducer, it was found that the experimental results and FE solutions were both in good match with the analytical calculations. For a rectangular d31 PZT transducer however, it was observed that the FE impedance response replicates much better the experimental response than the analytical analysis. The deviation was attributed to low-aspect-ratio specimens which lessen the accuracy of 1D analysis assumption. For a shear-mode transducer, it was noted that the natural EM resonances of analytical analysis were in good agreement with the FE resonances with negligible

difference in higher modes whereas a comparison with experimental resonances yielded about 10% difference. The difference was attributed to high sensitivity of shear-mode transducer to geometrical and piezoelectric material properties that influence the EM resonant frequencies.

Chapter 4
Guided Lamb Waves in Thin Plates

This chapter investigates the traits of fundamental Lamb modes under symmetric and antisymmetric actuations to detect structural damage. The analysis begins with validation of FE approach that is used in the subsequent sections. The propagation of Lamb waves in a thin plate involving the use of piezoelectric transducers simulated using 3D finite element multiphysics analysis to validate a pitch-catch experiment. A full-field view of elastic wave propagation is discussed to foster an understanding of the interaction of Lamb waves in plates. The next section presents pulse-echo analysis conducted on a damaged plate with a pair of transducers modeled on both sides to send symmetric and antisymmetric actuation signals. This analysis is then followed by damage localization using the time-of-flight method. The following section presents a pitch-catch analysis of a plate with the same damage characteristics used in pulse-echo method. The damage location predicted from the scattered Lamb modes is then compared with the actual damage location.

4.1. Validation of FE Approach

This section serves as a validation unit for a FE approach that is used throughout this chapter to simulate ultrasonic wave propagation in a thin plate. A 3D multiphysics analysis as well as 2D structural analysis are conducted to simulate guided Lamb waves from the transmitter (actuator) to the receiver (sensor). The waveform responses are then plotted against experimental response for validation of the FE modeling method.

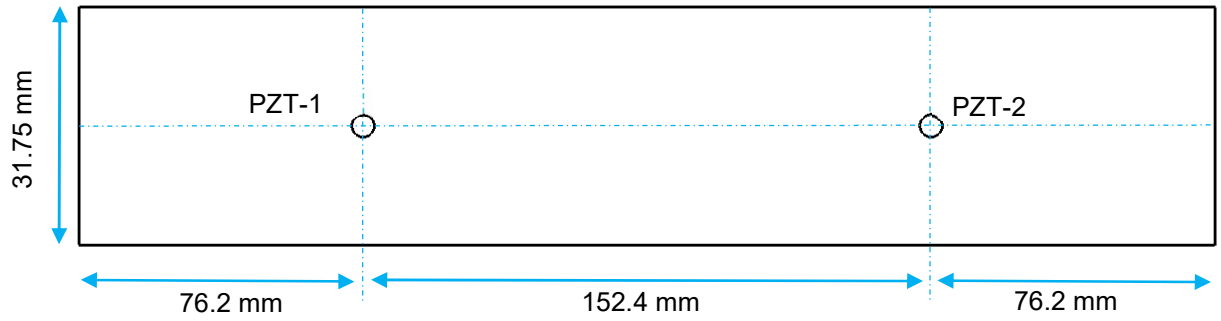

Figure 4.1: Schematic diagram of a 1 mm aluminum plate with two 6 mm round PZT transducers attached in a pitch-catch configuration.

4.1.1. Finite element analysis

3D FE modeling: In Figure 4.1, an aluminum plate with two round PZTs attached on the surface are simulated in a commercial FE software, ANSYS 17.0. To simulate electromechanical response of the PZTs, 3D multiphysics analysis is conducted using a 10-node coupled-field solid element, SOLID227. This element has five degrees of freedom including voltage, temperature, and nodal displacement in global coordinates. The plate was meshed with structural solid element (SOLID187) with 10 nodes which makes it suitable to transmit elastic waves from and to the transducers.

To define the interface regions between the transducers and the plate as fully bonded components, contact elements (CONTA174) and target elements (TARGE170) are used to mesh the interface regions. The mesh at the interface is further refined to improve solution accuracy and convergence. PZT-1 was simulated as an actuator through the application of voltage coupling and alternating voltage on all nodes located on its top and bottom surfaces. PZT-2 is simulated as a sensor through the application of coupling voltage on nodes located at both sensors' surfaces while voltage is set on the bottom surface. The piezoelectric material properties used for both transducers are provided in

Table 1 of the Appendix. The actuation signal is plotted in Figure 4.2a. The signal captured by the sensor is plotted in Figure 4.2b.

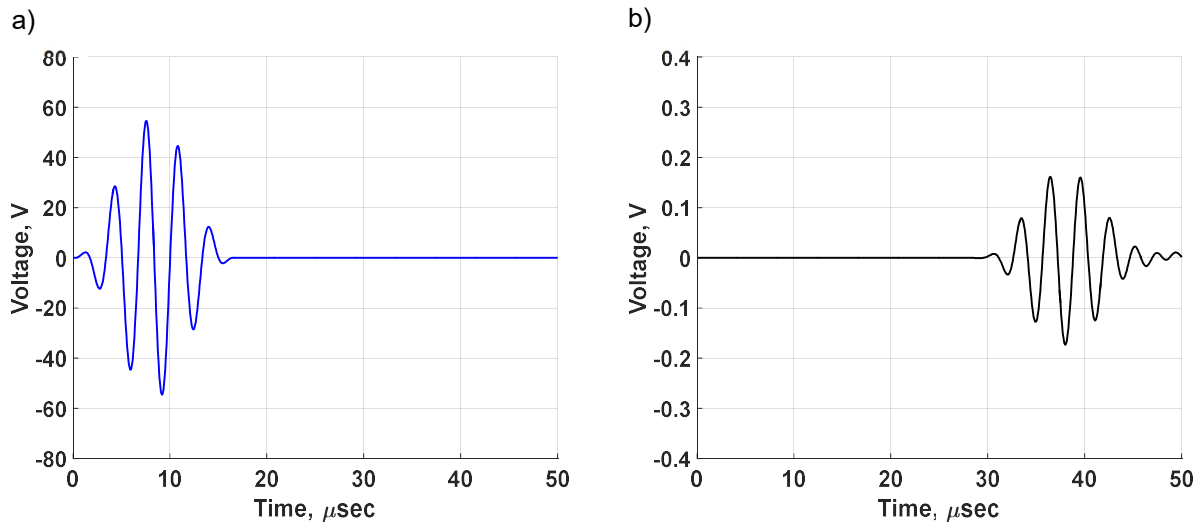

Figure 4.2: Pitch-catch method of aluminum plate with two surface-mounted d31 PZTs: a) actuation signal at 300 kHz; b) 3D FE sensor signal.

Elastic waves combine according to the principle of superposition of harmonic waves result in a stationary vibration pattern known as a standing wave. Standing waves are expected to be generated in the medium when superposition of waves occurs at frequency that relatively close to the natural frequencies of the plate. In Figure 4.3, the distribution of wave propagation in the plate from the actuator to the sensor is displayed beginning at 4 μs*ec* to the time at which the signal arrives the sensor, at about 32 μsec. The guided waves reach the horizontal boundaries at 10 μ*sec*, and the reflected waves at both ends interfere with the part of the wave that still moving towards the boundaries. It can be noted from Figure 4.3 at 20 μsec the wave interference is neither fully constructive nor destrutive, but the vibrational (pressure) nodes and displacement antinodes of the standing waves can easily be obsereved.

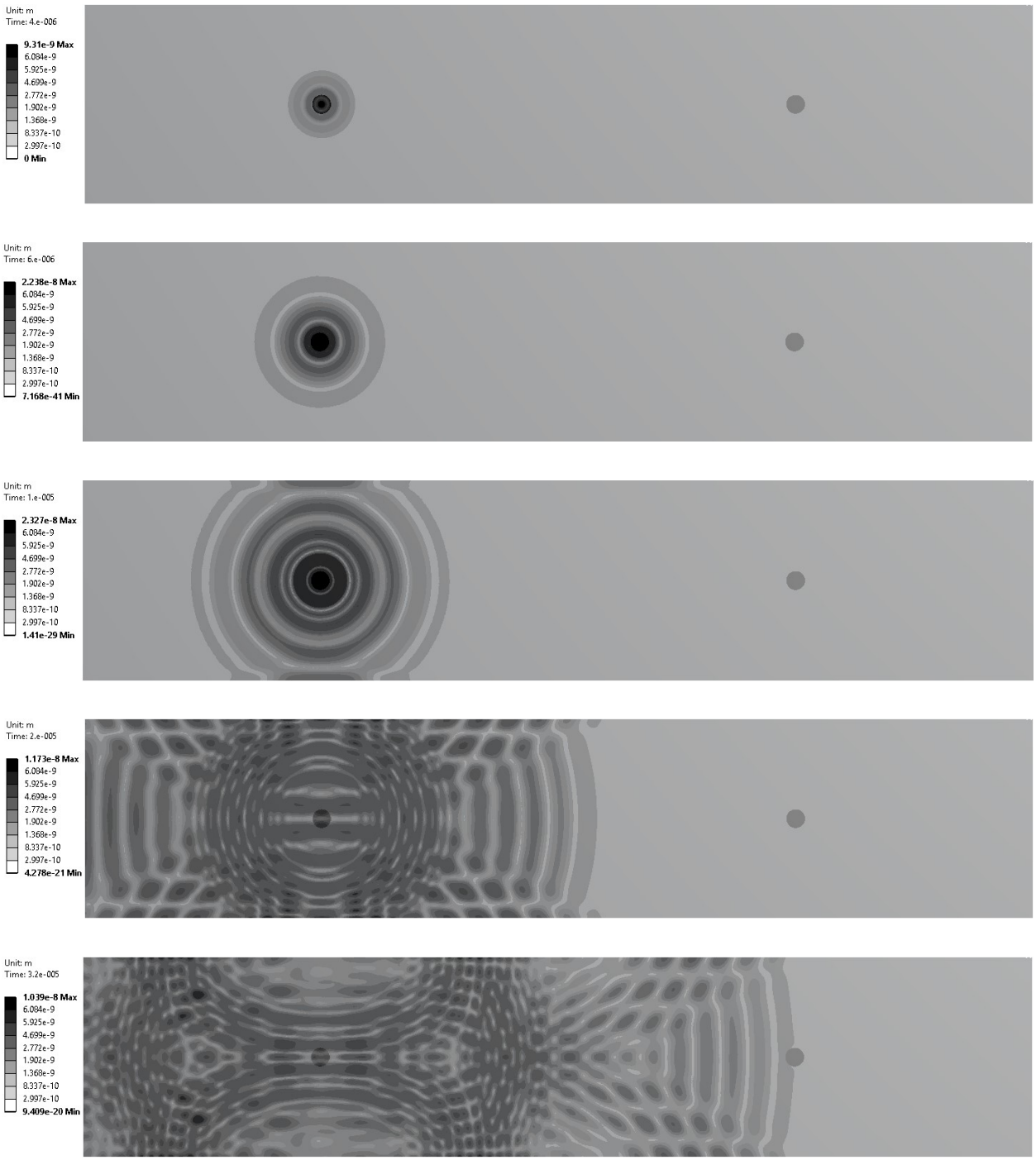

Figure 4.3: Total deflection full-field view of elastic wave propagation in 1 mm aluminum plate at (up to down): 4 μsec, 6 μsec, 10 μsec, 20 μsec, and 32 μsec.

In the region near the actuator, the wave pulse (packet) no longer exists in its original form as the structural vibration is continuously being developed throughout the plate. Due to boundary reflection from top and bottom surfaces, the actuation signal is only preserved in the direction in which it is traveling to the sensor. Thus, it can be also noted from Figure 4.3 that at 32 μsec a strong reflection signal from the top edge is expected to reach the sensor next.

2D FE modeling: To investigate whether the waveform response can be obtained via 2D analysis with reasonable accuracy in comparison to 3D multiphysics, 2D FE structural analysis is conducted herein.

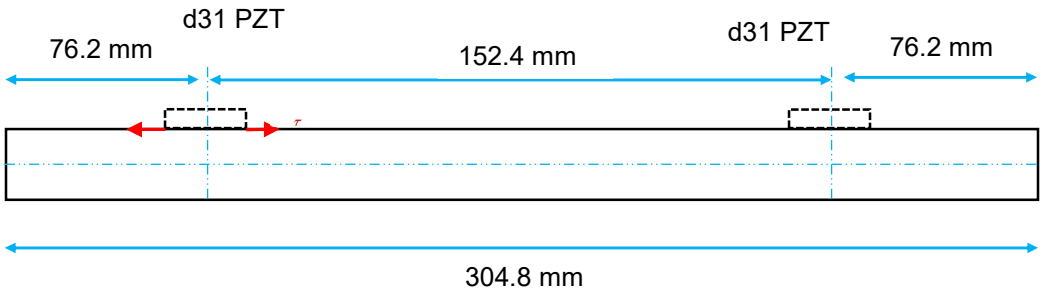

Figure 4.4: 2D schematic diagram of a 1 mm aluminum plate with two d31 PZT transducers.

In Figure 4.4, a 1 mm aluminum plate is shown along with two d31 piezoelectric transducers 152.4 mm apart and at an equal distance from the boundaries. As early discussed in Chapter 3, when voltage V applied on a piezoelectric transducer, it induces an electric field E which induces mechanical strain that is governed by the piezoelectric coupling relation as

$$s_1 = d_{31} E_3 \tag{4.1}$$

where $E_3 = V / h$, and h is the thickness. This strain is transmitted to the structure through the bonding layer predominantly in the form of shear stress. Thus, the actuation signal

which has been used in 3D analysis can be calculated in terms of displacement using Eq. (4.1).

To simulate the traction from the actuator, a nodal displacement is applied to the end nodes corresponding to the location of the actuator. The plate was meshed using PLANE183 which is an 8-node element with two degrees of freedom at each node: translation in x and y directions. Due to high width-to-thickness ratio, a plane strain condition was set for the analysis. The waveform response captured at the sensor is normalized and plotted in Figure 4.5a. The signal received within 50 μsec period is compared to the signal captured through actual modeling of PZT transducers in 3D multiphysics analysis. It is worth mentioning that this simple model of PZT-structure interaction known as pin-force model represents the first order approximation of PZT interaction with the plate. It is expected to produce reasonable results at low actuation frequencies [1].

4.1.2. Experiment

To validate the results obtained from FE simulation, a plate with two piezoelectric transducers attached in a pitch-catch configuration is carried out. The dimensions of the plate and the piezoelectric transducers are similar to the ones given in the FE modeling section.

A waveform generator was used to excite the structure with a 5-peak modulated signal at 300 kHz carrier frequency and 54 Volt peak-to-peak voltage. The actuation signal obtained from the oscilloscope was plotted in Figure 4.2a. At this given frequency, the

first symmetric mode is expected to arrive first to the sensor. Thus, the main wave packet in Figure 4.5b is the S0 Lamb mode.

It has been discussed in Chapter 2 that Lamb waves are dispersive meaning that their speed depends on the frequency-thickness product, fh. However, the S0 Lamb mode hardly exhibits the dispersion effect and that is due to low actuation frequency. At low frequency, the S0 inherits the characteristics of axial waves in a plate which are non-dispersive waves. The A0 mode however exhibits the characteristics of flexural waves in plate which are highly dispersive. The concept of dispersion rate of fundamental Lamb modes is further discussed in the next sections.

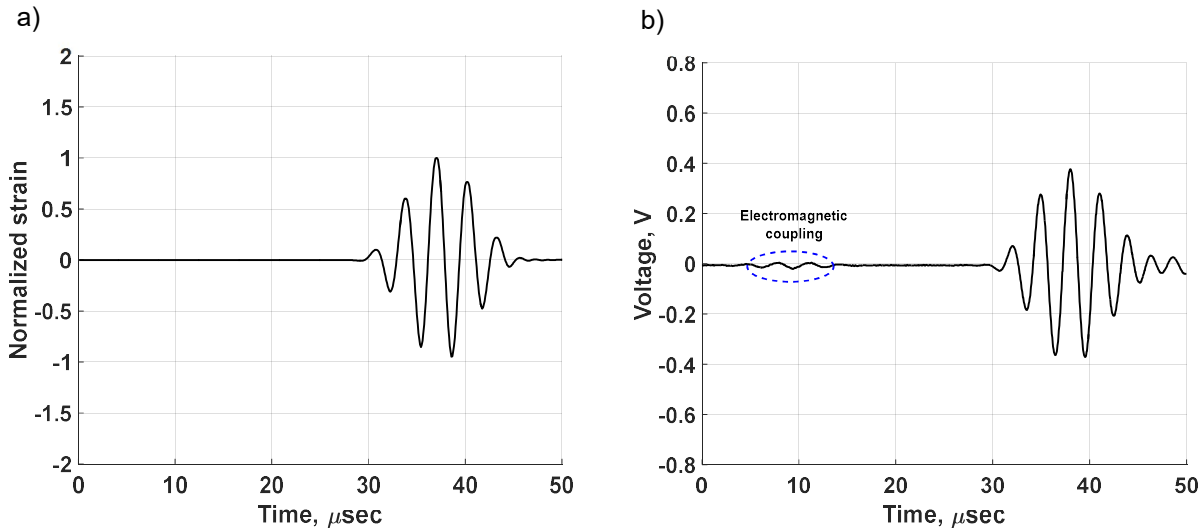

Figure 4.5: Pitch-catch method of aluminum plate with two d31 PZTs for waveform obtained from: a) 2D FE structural analysis; b) experiment.

The extra wave packet received at the beginning of the waveform (see Figure 4.5b) is induced due to electromagnetic coupling of the wires. This concept will not be discussed herein because of irrelevancy to the propagation of elastic waves. Comparing experimental response to the 3D FE response indicates a good agreement in the overall

shape of the wave packet. The experimental response is about twice in magnitude as compared to the FE. There are several factors including geometrical and electromechanical tolerances could contribute to this discrepancy.

Likewise, it can be observed from Figure 4.5a that 2D FE model exhibits no side peaks after the wave packet fully received and that is because waves reflected from the width boundaries which are expected to arrive next are omitted due to the nature of 2D analysis. Therefore, this causes the waveform response to have higher resolution compared to 3D multiphysics and experimental response. On the other hand, it may be realized that the FE method simulates the actual testing with reasonable accuracy that makes it a suitable approach to carry over to the subsequent analyses.

4.2. Pulse-echo Method with d31 PZT Transducers

To study the influence of damage on fundamental Lamb modes, a 2D aluminum plate was modeled in ANSYS17.0 with a pair of piezoelectric wafer active transducers mounted at the center in order to excite symmetric and antisymmetric Lamb modes. It is assumed that the ratio of width to thickness is large enough to satisfy the plain strain condition for 2D structural analysis.

In Figure 4.6, the structure is modeled with no damage to obtain a baseline signal. Another model is created with a single damage (notch 1) which is 0.5 mm deep and 0.25 mm wide located at 100 mm from the actuators. To investigate the effect of multiple defects on damage diagnostics, another identical damage (notch 2) is introduced at 50 mm to the right of notch 1. The generated signals are processed to study the concept of

scattered Lamb modes under the influence of damage. Additionally, the signals are further processed to identify the damage location using the time-of-flight method.

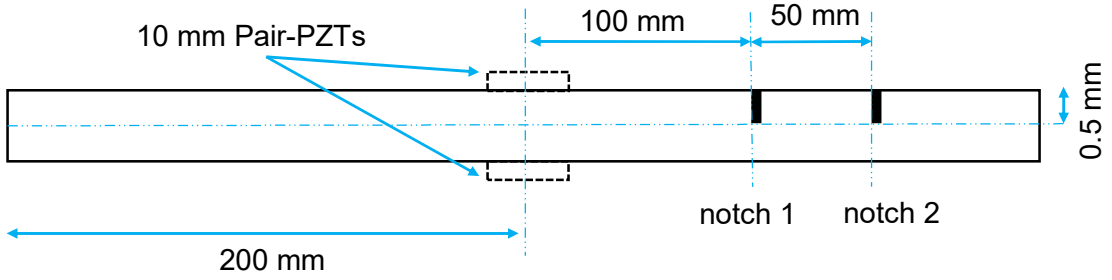

Figure 4.6: Notched plate with a pair of PZT transducers attached at the center.

4.2.1. Pulse-echo method: symmetric actuation

As mentioned earlier in Section 4.1, the mechanical strains induced by d31 piezoelectric actuators can effectively be simulated as shear forces. Therefore, nodal displacement components are applied on both sides to simulate the shear force exerted by the actuators at the center of the plate. They are excited symmetrically to propagate the S0 mode in the plate with 3-peak Hann windowed tone burst signal with a center frequency of 300 kHz. The Lamb wave dispersion curves in Figure 4.7 indicates two Lamb modes are predicted at this center frequency. As mentioned earlier, the actuation signal is modulated with Hann window yielding a wave packet that contains a group of waves traveling at different speeds. A wave packet with higher variation in wave speed, it is predicted to be more dispersive, becoming wide. The frequency of the actuation signal ranged between 100 kHz and 500 kHz.

In Figure 4.7c, the dispersion rate curve of group velocity shows the relation between excitation frequency and the dispersion rate of fundamental Lamb modes. The wave speeds of S0 and A0 are highlighted in the group velocity dispersion curves at the center

frequency of the modulated actuation signal, see Figure 4.7b. However, the dispersion rate curves in Figure 4.7c indicates the A0 mode is highly dispersive over the excitation frequency range and that reveals using the wave speed at the center frequency is not expected to produce accurate results. Therefore, the wave speed of A0 at 500 kHz should be used for the analysis of damage localization. The wave speed can be analytically determined using Lamb wave equation as 2.841 mm/μsec. On the contrary, the S0 exhibits negligible dispersion effect over the frequency range of the modulated signal. The wave speed of S0 at 100 kHz can be determined 5.062 mm/μsec.

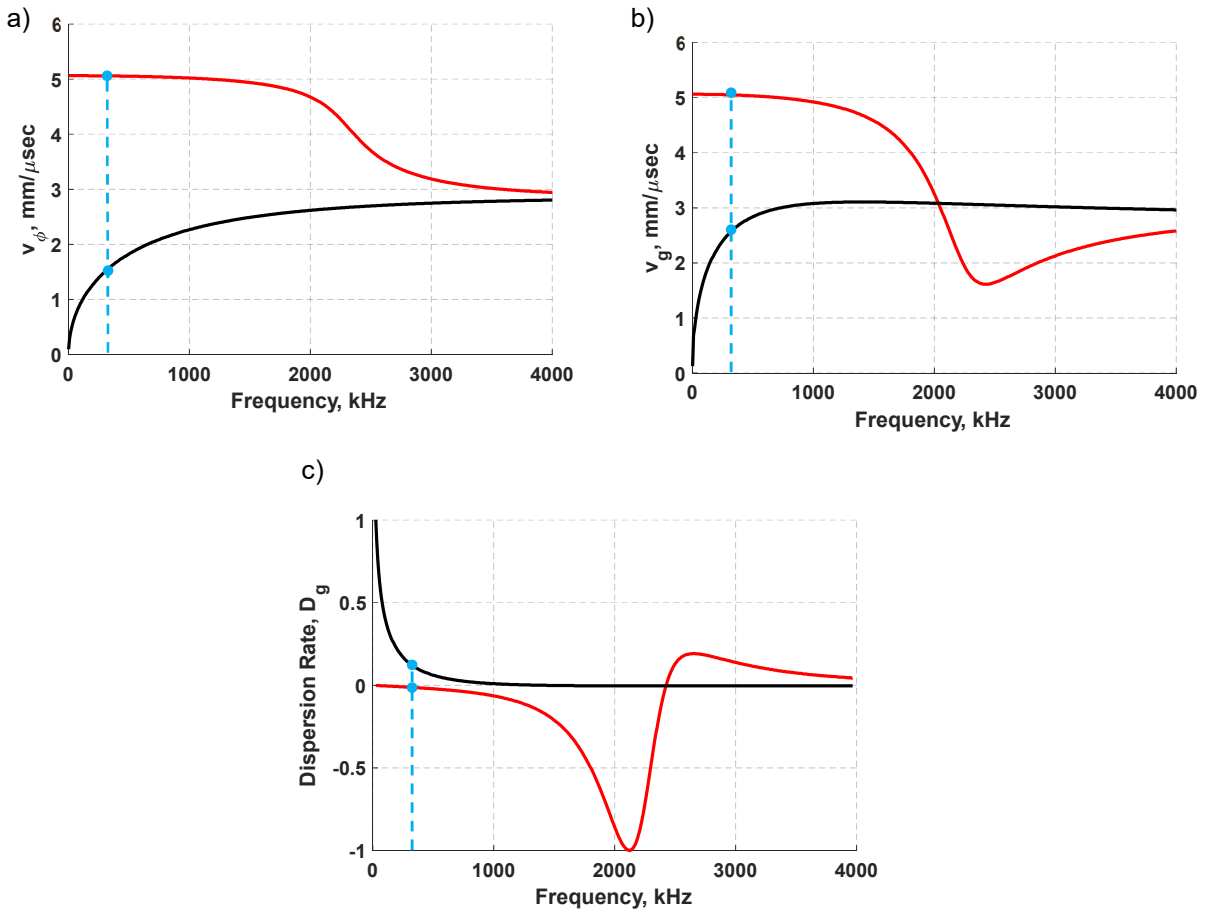

Figure 4.7: Dispersion curves of Lamb modes marked at 300 kHz: a) phase velocity; b) group velocity; c) normalized curves of dispersion rate.

The strain wave signals at the center were plotted for a pristine plate in Figure 4.8a-1. The first wave packet in the axial (longitudinal) strain wave is the actuation signal which is followed by the S0 mode reflection from the boundary. Similarly, these two wave packets are present in the axial strain signal from the damaged plate with a single notch in addition to two more wave packets induced by the notch. They are identified as the S0 mode reflection and the A0 mode reflection in Figure 4.8b-1.

Despite that S0 mode was only actuated, all possible modes at this center frequency exist in the plate due to the interaction of the incident wave with the inflicted damage causing mode conversion. The axial strain wave signals from both actuators are further processed to isolate the antisymmetric content and plot the shear strain wave signals. They are obtained by calculating the difference between the axial strain signal from the top and bottom sensors.

In Figure 4.8a-2, the shear strain indicates complete absence of antisymmetric modes for the pristine plate. On the other hand, the shear strain signal for the damaged plate with notch 1 exhibits the A0 reflection from the notch reaches the center first and the A0 reflection from the boundary reaches next as illustrated in Figure 4.8b-2.

Another case of damaged plate with double notch is also considered to investigate feasibility of the pulse-echo approach on identifying multiple damage via processing of fundamental Lamb modes. The second notch is introduced to the right of the first notch at 50 mm distance as shown in Figure 4.6. The plate is excited with the same actuation signal as the one used for the pristine plate and the damaged plate with a single notch. The axial strain signal and the shear strain signal are plotted in Figure 4.8c. The S0 reflection from notch 1 arrives first followed by a superposed wave packet of the A0

reflection from notch 1 and the S0 reflection from notch 2. The two modes are overlapped because the wave speed of S0 mode is higher than the wave speed of A0 mode.

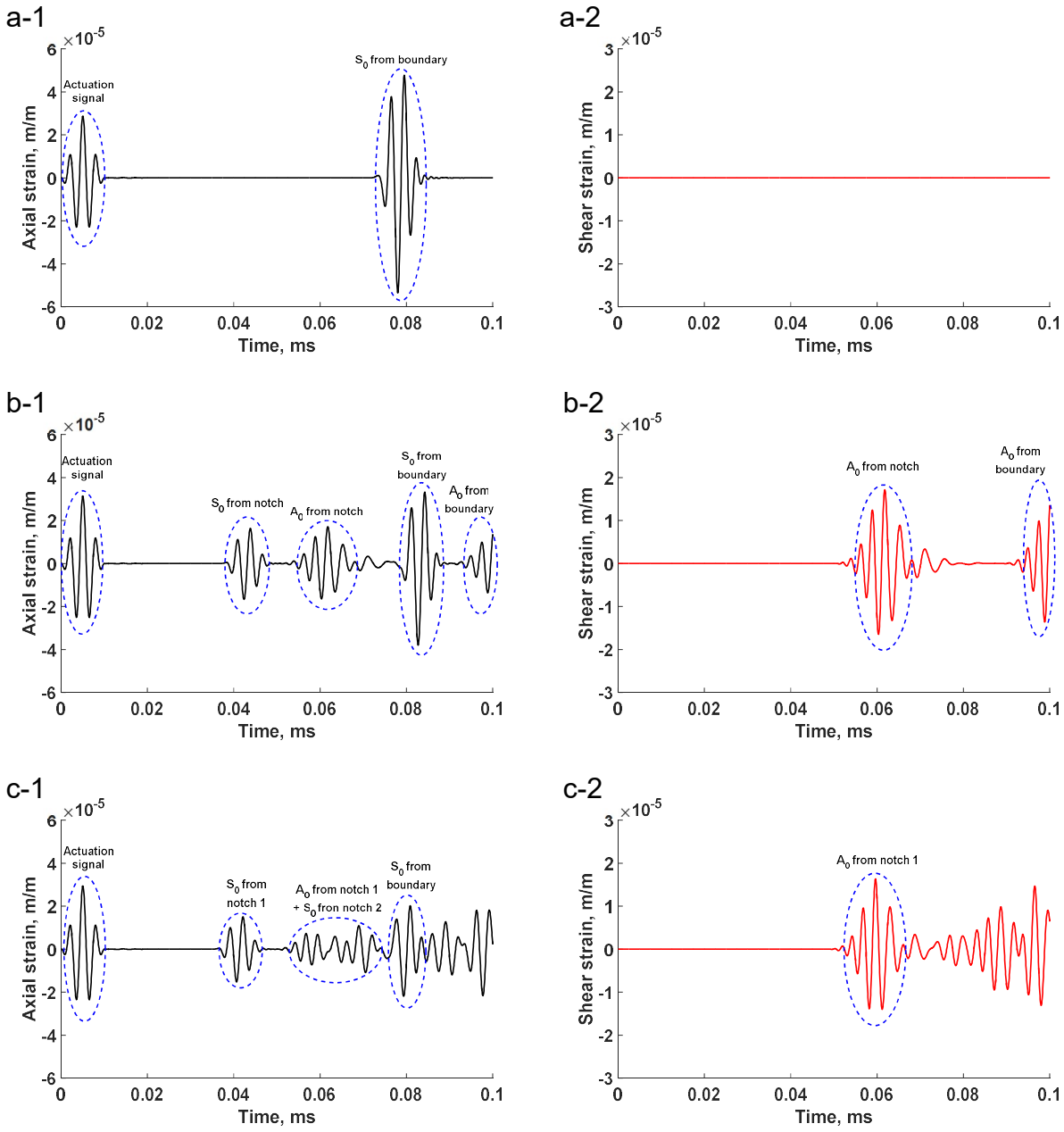

Figure 4.8: Axial (black) and shear (red) waveforms of a plate with a pair of PZTs at the center induced symmetric actuation: a) pristine plate; b) plate with single notch; c) plate with double notch.

In Figure 4.8c-2, the A0 mode from notch 1 is extracted from the superposed wave packet and exhibits very good agreement to the A0 mode obtained from case 2. The S0 reflection from the boundary arrives next and partially superposed of the A0 mode that is induced from the reflection and transmission of the actuation signal from both defects. Despite the location and size of damage being known beforehand, processing the signal of Lamb waves in structure with several defects poses a challenge to extract the damage characteristics.

4.2.2. Pulse-echo method: antisymmetric actuation

To propagate flexural waves in a plate, antisymmetric actuation is modeled by inducing surface traction at nodes corresponding the location of the actuators causing rotation about z - axis. The signal actuation is the same to the one used in the symmetric model analysis.

In Figure 4.9, the axial strain wave signals from both actuators are further processed to isolate symmetric contents (axial strain waves) and the antisymmetric contents (shear strain waves). The shear strain waveform at the center is plotted for the pristine plate in Figure 4.9a-1. The first wave packet in the pristine plate is the actuation signal which is followed by the reflection from the boundary while complete absence of symmetric modes is observed in Figure 4.9a-2.

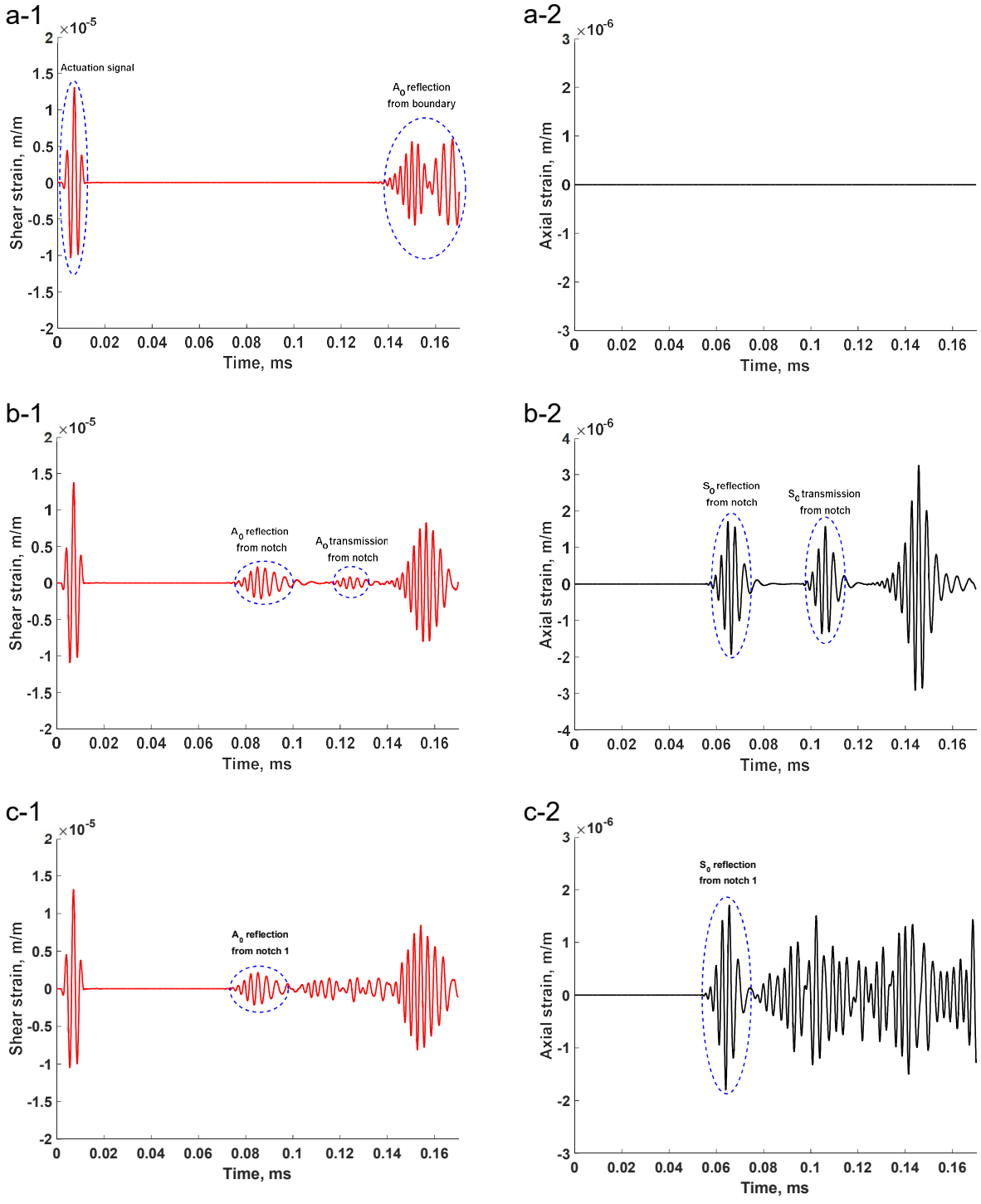

Figure 4.9: Shear (red) and axial (black) waveforms of a plate with a pair of PZTs at the center induced antisymmetric actuation: a) pristine plate; b) plate with single notch; c) plate with double notch.

In case of plate with single damage, two extra wave packets are generated due to the presence of damage as shown in Figure 4.9b-1. In Figure 4.9b-2, the first wave packet is S0 reflection which arrives first then followed by the second S0 mode which is transmitted through the notch, reflected back by the boundary and transmitted through the notch again then arrives at the center. Thus, the second A0 mode which is a scattered mode from the second transmitted S0 can be observed in Figure 4.9b-1. The A0 mode reflection from the notch arrives at the center then followed by the transmission A0 mode.

In Figure 4.9c, the first arrivals in a plate with double damage are the S0 and A0 from notch 1. The second damage caused multiple superposed wave packets to exist beyond the first arrivals in Figure 4.9c. This multimodal superposition phenomenon often imposes high uncertainty on the details of existing damage and the overall structural integrity.

4.2.3. Damage localization

The damage location can be calculated using either S0 reflection or A0 reflection. In order to predict the damage location from the waveform response, the ToF of A0 mode was used in symmetric actuation while the ToF of S0 used in antisymmetric actuation. Using displacement-velocity relation, the location of damage can be calculated as

$$L_d = ToF\left[\frac{1}{c_{S_0}} + \frac{1}{c_{A_0}}\right]^{-1} \tag{4.2}$$

In Eq.(4.2), ToF is the time of flight for the actuation signal to reach damage plus the time for a reflected scattered mode (S0 or A0 mode) to travel from damage to the transducer, c_{S_0} is the wave speed of S0, c_{A_0} is the wave speed of A0, and L_d is the distance between

the actuator and damage. It is worth mentioning that in case the actuation signal and the scattered mode have the same speed, Eq.(4.2) can be simplified as

$$L_d = ToF\left[2\frac{1}{c}\right]^{-1} \tag{4.3}$$

In Eq.(4.3), c is the wave speed.

A summary of results including ToF, damage location and error with respect to the actual damage location are listed in Table 4-1. A 5% threshold of the maximum voltage was used to determine the arrival time of scattered mode at which the wave packet signal reaches the sensor. The error was calculated with respect to the actual distance between the actuator and notch 1 which is 95 mm. In symmetric actuation, the damage location using the ToF of A0 in plate with single damage analysis is predicted at 97.7 mm from the source with 2.8% error. Likewise, there is about 1% error in the predicted location of notch 1 when notch 2 introduced on the surface of the plate. In antisymmetric actuation however, the results show higher error in damage location of notch 1 compared to symmetric actuation. Since the S0 and A0 mode travel the same distance in all model cases, the ToF is expected to be very similar. Therefore, the high error in antisymmetric actuation can be predominantly attributed to the thresholding method implemented herein to determine the arrival time.

Table 4-1: Damage localization of notch 1 in pulse-echo method.

	Symmetric Actuation			Antisymmetric Actuation		
Case	ToF(A0)	L_d	Error	ToF(S0)	L_d	Error
	μsec	mm	%	μsec	mm	%
Single damage	53.7	97.7	2.8	57.2	104.1	9.6
Double damage	52.7	95.9	1.0	58.4	106.1	11.7

4.3. Pitch-catch Method with d31 PZT Transducers

The pitch-catch method is another commonly used technique in SHM to detect changes in ultrasonic wave response that takes place between two piezoelectric transducers. The damage detection process is performed through the comparison of guided waves in terms of amplitude, phase, time of flight, and dispersion against a baseline signal. More details on this method were discussed in Chapter 2.

To study the guided Lamb waves scattering from a notch in a pitch-catch configuration, a 2D aluminum plate with piezoelectric transducers mounted in pair at 100 mm and at 300 mm is considered (see Figure 4.10). Therefore, symmetric and antisymmetric excitation can be performed to propagate axial (longitudinal) waves and flexural waves in the plate. It is assumed that the plain strain condition is satisfied for 2D structural analysis.

A 1 mm aluminum plate is modeled damage-free to obtain a baseline signal for comparison with two damage scenarios. The damage characteristics discussed in pulse-echo models are used in this method as well. Notch 1 located at the center of the plate is 0.5 mm in depth and 0.25 mm in width. Notch 2 is located 50 mm from the sensors. The signals obtained from the models are processed to study the traits of Lamb waves under symmetric and antisymmetric actuation for damage evaluation.

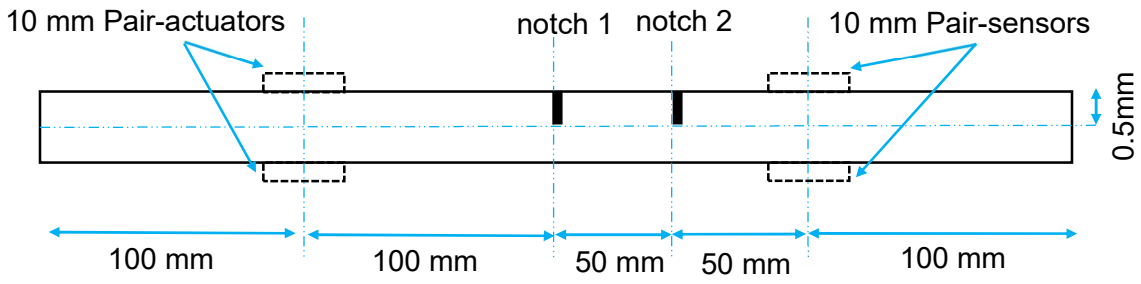

Figure 4.10: A notched plate with a pair of PZT transducers.

4.3.1. Pitch-catch method: symmetric actuation

The actuators are simulated herein as shear traction along the surface at the predefined locations. They are excited symmetrically to propagate the S0 mode in the plate with 3-peak Hann windowed tone burst signal with a center frequency of 300 kHz. The waveform responses of three cases including pristine plate, damaged plate with single notch, and damaged plate with double notch are obtained from the pair-sensors as shown in Figure 4.11. The excitation frequency shown in the group velocity dispersion curve in Figure 4.7b suggests the existence of fundamental Lamb modes at the given excitation frequency.

In Figure 4.11a-1, the first wave packet in the baseline response is the S0 actuation signal followed by the S0 reflection from the boundary. The waveform response from damaged plate with a single notch shows the S0 transmission from the notch reaches the sensors first then the A0 transmission followed by their corresponding reflections from the boundary as illustrated in Figure 4.11b-1. The shear strain signal exhibits the A0 wave packet from the notch and its corresponding reflection in Figure 4.11b-2 while a complete absence of shear waves in the pristine response in Figure 4.11a-2.

It can be noted from Figure 4.11c-1, introducing another notch at 50 mm to the right of the first notch yields the S0 transmission and two A0 modes from notch 2 and notch 1, respectively. The A0 modes extracted from the axial strain signals are labeled in Figure 4.11c-2. As can be observed, the resolution of waveform responses from the pitch-catch method is significantly higher as compared with the waveform responses from the pulse-echo method especially for identifying the number of defects present in the structure.

However, despite the scattered modes are partially superposed, this scenario could be made more challenging if the defects are further close together.

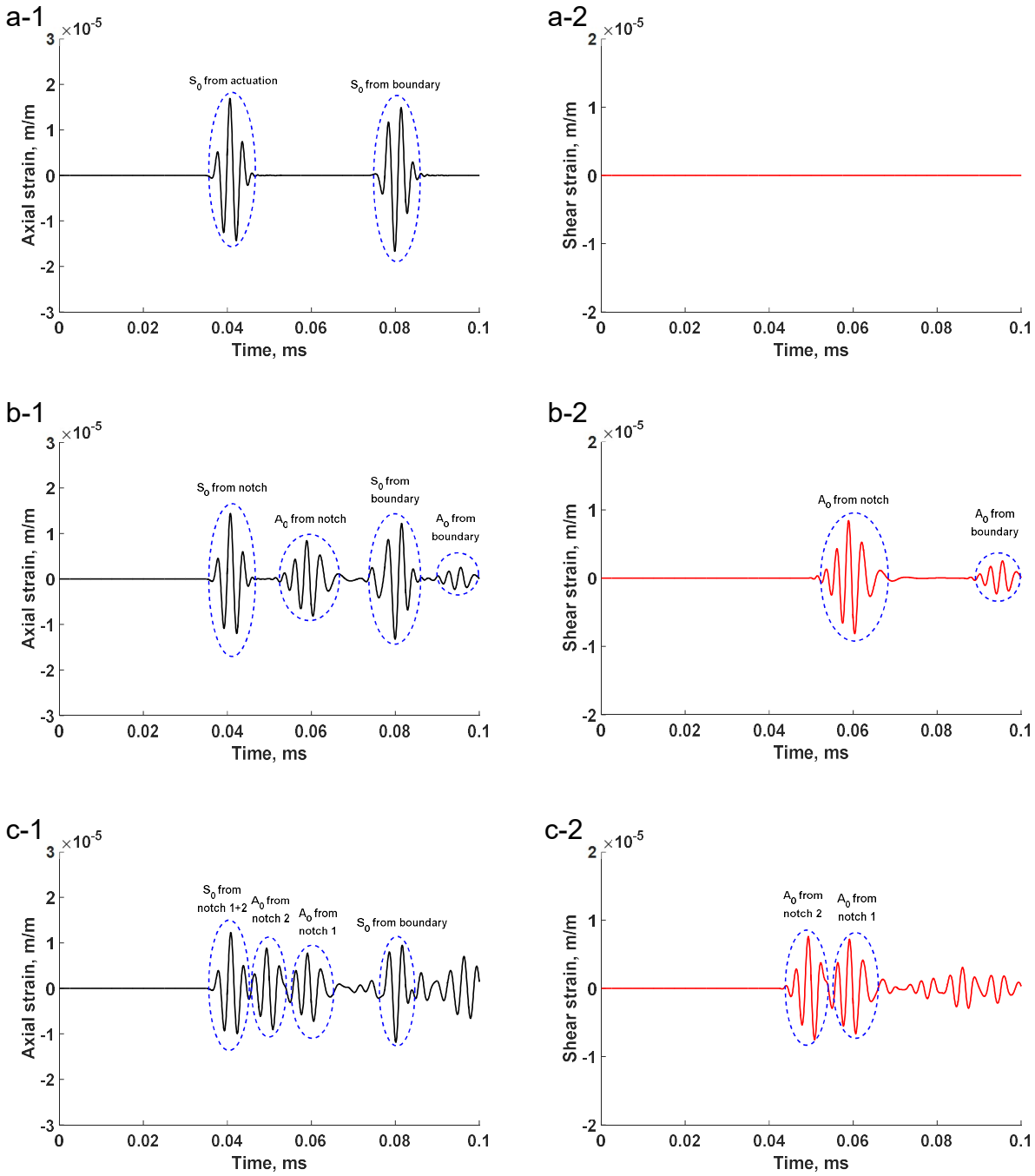

Figure 4.11: Axial (black) and shear (red) waveforms of a plate excited symmetrically with a pair of PZTs: a) pristine plate; b) plate with single notch; c) plate with double notch.

4.3.2. Pitch-catch method: antisymmetric actuation

In antisymmetric actuation, a pair of actuators located 100 mm are excited anti-symmetrically with the same actuation signal used in symmetric actuation with the exception of applying opposite nodal displacement to induce rotation about z - axis. Likewise, the waveform responses of three cases including pristine, damaged plate with single notch, and damaged plate with double notch are received by the pair-sensors after traveling 190 mm. In Figure 4.12a-1, the actuation signal received by the sensors exhibits the dispersion phenomenon with several counts. Similarly, the dispersed actuation signal of damaged plate with a single notch preserves its shape but exhibits some loss of energy in the form of attenuation due to wave scattering as displayed in Figure 4.12b-1. It can be observed from Figure 4.12b-2 the first mode reaches the pair-sensors is the S0 transmission from notch 1 followed by its reflection from the boundary.

The actuation signal is further attenuated in the waveform response of damaged plate with double notch in Figure 4.12c-1. The loss of energy converted into two S0 modes being produced for each notch as shown in Figure 4.12c-2. Because the distance between the two notches is relatively small, the wave packet of S0 modes exhibit overlap waves in the waveform response. However, identifying number of damage using a pitch-catch method depends on several parameters that can influence the resolution and accuracy of damage identification including distance among defects, distance between the defect and sensors, size of damage, signal actuation characteristics (excitation frequency, number of counts, number of samples, windowing method). As per the literature review, identifying number of damage using Lamb waves is still ongoing issue [45].

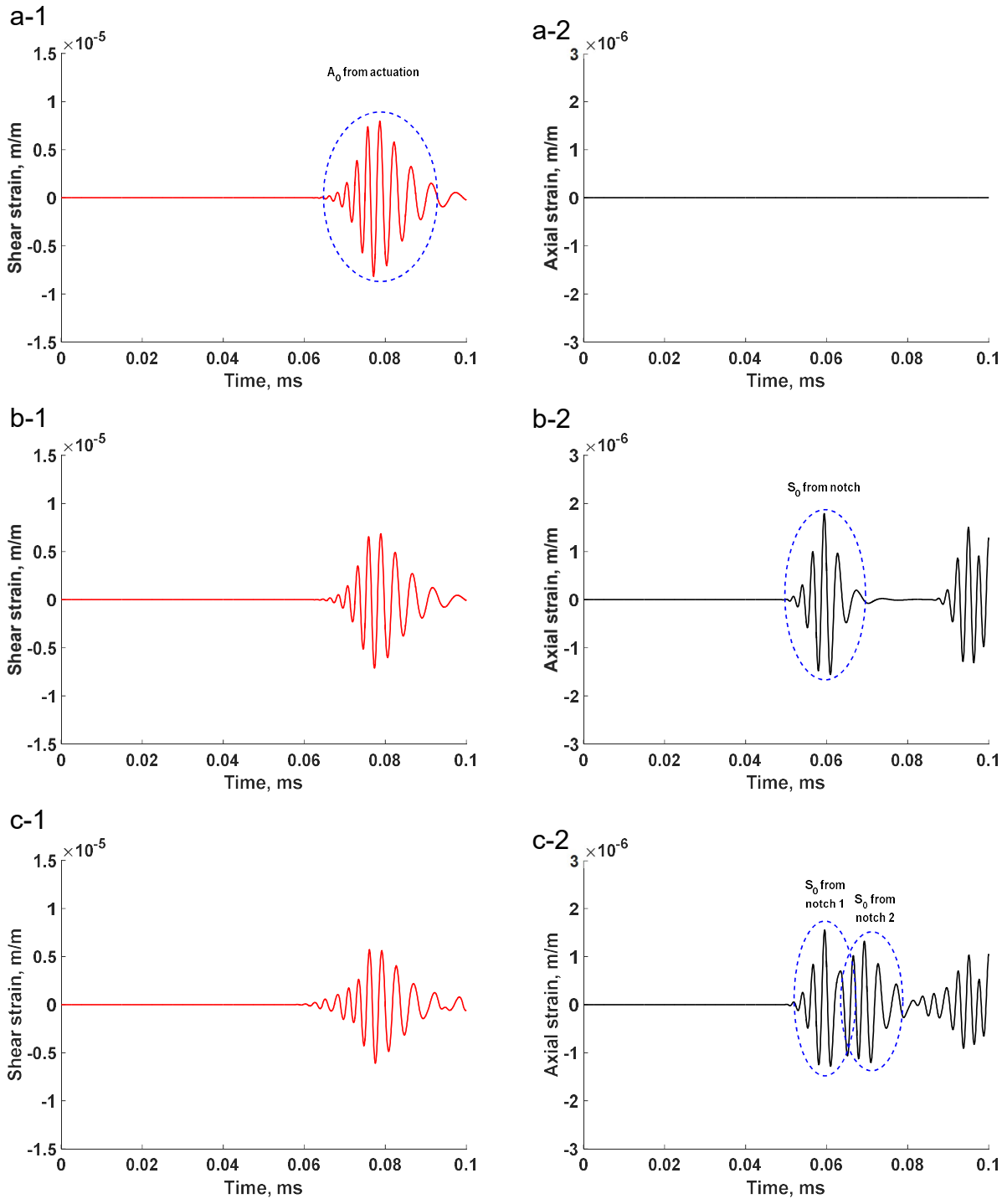

Figure 4.12: Shear (red) and axial (black) waveforms of a plate excited anti-symmetrically with a pair of PZTs: a) pristine plate; b) plate with single notch; c) plate with double notch.

4.3.3. Damage localization

In pitch-catch configuration, the transmitted scattered mode is of interest to predict damage location through the use of the ToF method. As earlier discussion on symmetric actuation, the S0 mode transmits through the notch accompanied with some (or negligible) distortion that is dependent on the characteristics of damage itself. However, it can be noted from Figure 4.11 that the ToF of the S0 mode in the pristine status and the damaged status are about the same which makes it not sensitive to the damage location. Therefore, the ToF of the scattered mode, A0, should be used to identify the damage location as

$$L_d^{A_0} = \frac{c_{A_0} ToF - l}{c_{A_0} / c_{S_0} - 1} \tag{4.4}$$

In Eq.(4.4), $L_d^{A_0}$ is the location of damage using the A0 mode, ToF is the total time for the S0 mode (actuation signal) to reach the damage plus the time of the A0 mode (transmitted scattered mode) to travel from the damage to the sensor, l is the distance between the transducers. On the other hand, the ToF of S0 should be used in case of antisymmetric actuation as

$$L_d^{S_0} = \frac{c_{S_0} ToF - l}{c_{S_0} / c_{A_0} - 1} \tag{4.5}$$

In Eq.(4.5), $L_d^{S_0}$ is the location of damage using the S0 mode, ToF is the total time for the A0 mode (actuation signal) to reach the damage plus the time of the S0 mode (transmitted scattered mode) to travel from the damage to the sensor.

The signal generated by the actuators travels 95 mm before it reaches notch 1 because each actuator has a length of 10 mm. Since the actuation signal predominantly

starts propagating in the plate at the edge of the actuator, the signal travels 95 mm to reach notch 1 (center of the plate) and another 95 mm to reach the sensor, $l =$ 190 mm. The error was calculated with respect to the actual distance between the damage and notch 1 which is 95 mm. Results summary for identifying the location of damage in a pitch-catch configuration are provided in Table 4-2. A 5% threshold of the maximum voltage was used to determine the arrival time. With the exception of symmetric actuation of plate with double damage, all other cases show the damage location is predicted with small error.

Table 4-2: Damage localization of notch 1 in pitch-catch method.

	Symmetric Actuation			Antisymmetric Actuation		
Case	ToF(A0)	L_d	Error	ToF(S0)	L_d	Error
	μsec	mm	%	μsec	mm	%
Single damage	52.2	95.1	0.1	52.5	96.8	1.9
Double damage	43.9	114.9	21	52.6	97.5	2.6

As can be observed from Figure 4.11c-2, the A0 mode from notch 2 arrives first followed by A0 mode from notch 1 with mode overlapping that results in difficulty to determine the arrival time for A0 from notch 1. Therefore, there is about 21% error in the predicted damage location of notch 1. This challenge, however, is not observed in antisymmetric actuation because the S0 from notch 1 arrives first. It is important to mention identifying the location of damage with reasonable accuracy is a challenging problem because there are several parameters involving material properties, numerical computation and signal processing have pronounced impact on the final outcomes. For instance, a little shift in the ToF predicted by a thresholding method or the wave speed using Lamb wave equation could result in erroneous findings. This problem investigated

herein is simplified enough to demonstrate some possible challenges that may be encountered to achieve this purpose using Lamb waves.

4.4. Summary and Conclusions

To validate the FE modeling procedure carried out throughout this chapter, ultrasonic guided waves in a thin aluminum plate were simulated by using 3D multiphysics analysis and 2D structural analysis for comparison with experimental wave signals. Additionally, a full-field distribution of wave propagation was also discussed to foster an understanding of Lamb modes interaction in plates. The waveform responses from FE methods and experiment were found comparable with reasonable agreement.

To study the concept of wave scattering under the influence of damage, two common methods were used pulse-echo method and pitch-catch method. d31 PZTs were simulated in pair to excite the structure symmetrically and anti-symmetrically. The actuation signal, 3-peak Hann windowed at 300 kHz, were kept the same in all models for comparison purposes. The waveform response of a pristine plate was compared against the response of a plate simulated with a single damage and another plate with double damage as well. The axial waves and the shear waves were plotted separately in order to identify the fundamental Lamb modes propagating in the plate. Despite a single mode of actuation was applied to excite the structure, all possible fundamental Lamb modes were present due to the characteristics of existing damage in both pitch-catch and pulse-echo analyses. Pitch-catch method, however, was found to produce higher resolution waveform responses compared to pulse-echo method. It was observed the superposition of multimode Lamb waves could present a challenge to isolate existing individual modes and analyze their characteristics. Therefore, extracting the damage

characteristics from multimode waveforms requires a robust signal processing algorithm to accomplish this purpose with minimal uncertainty. This challenge often escalates when multiple defects with different damage characteristics exist between two transducers in the structure.

The scattered Lamb modes were processed to identify the damage location of notch 1. The ToF method was implemented to identify the location of notch 1 from the actuators in both configurations. A 5% threshold was used to determine the arrival time of a scattered mode. It was observed using the wave speed determined from the Lamb wave equation in conjunction with FE waveform responses can yield accurate results. The majority of the error found in damage localization is attributed to the thresholding method while numerical convergence is expected to contribute little as well. A promising method to overcome this challenge is to use time-frequency approach in order to track the center frequency of a wave packet rather the arrival time. This method will be discussed in the next chapter.

Chapter 5
Properties of Ultrasonic Waves Induced by d35 PZT Actuators: Simulation Study

This chapter investigates the characteristics of ultrasonic waves generated by embedded shear-mode PZT transducers in structures. This study uses FE method throughout the analysis. The first section begins with FE modeling procedure of a multilayered structure using 3D multiphysics analysis followed by 2D multiphysics analysis in order to ensure appropriate modeling of ultrasonic antisymmetric (flexural) waves for the subsequent analyses in the following chapters. This chapter concludes with summary and conclusions which highlight the main findings of this study.

5.1. Numerical Simulations

This study begins with numerical analysis exploring the waveform generation and propagation of flexural waves in a laminate structure with shear-mode lead zirconate titanate (d35 PZT) piezoelectric transducers embedded in the bondline. Fundamental understanding of these waves generated and sensed by d35 PZT piezoelectric transducers in laminate structures is necessary to accurately model their behavior. This is crucial for effectively evaluating their capability to detect various joint defects and developing a robust signal processing algorithm for SHM.

The laminate structure consists of two d35 PZT piezoelectric transducers placed in the bondline of two aluminum substrates bonded together with a layer of adhesive. The overall geometry of the laminate structure is shown in Figure 5-1. The d35 PZT piezoelectric transducers with material properties given in Table 1 of the Appendix have

a square cross-section of 15 mm and a thickness of 1 mm. The two substrates made of aluminum 6061-T6 are 250 mm in length, 80 mm in width, and 1 mm in thickness. The d35 PZTs are placed 115 mm apart with 40 mm distance from top and bottom boundaries and 67.5 mm from left and right boundaries. The adhesive layer that assembles the laminate structure together is 1 mm thick with material properties provided in Table 1 of the Appendix. The configuration of d35 PZT transducers as well as the dimensions of the laminate structure were determined based on the wave reflection analysis to avoid reflection overlap with the first wave packet arrival. The FE simulation results were then processed using a signal processing algorithm based on time-frequency methods.

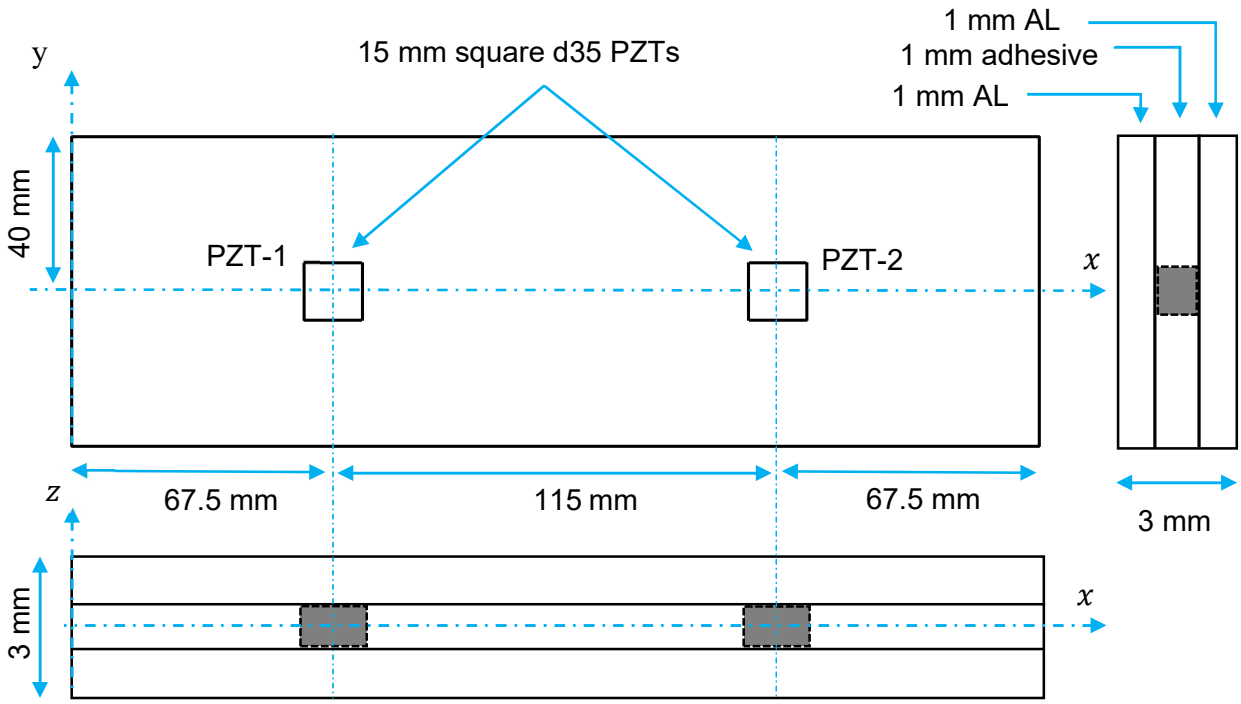

Figure 5-1: Schematic diagram of an aluminum multilayered structure with two shear-mode PZT transducers placed in the bondline.

5.1.1. 3-D Finite element modeling

A 3D numerical simulation of the laminate structure was implemented to simulate the propagation of flexural waves emitted from d35 PZT piezoelectric actuator. The numerical simulation was performed on ANSYS 17.0. The piezoelectricity of the PZT transducers was simulated by conducting a multiphysics analysis that couples electrical field and mechanical field simultaneously in the solution process. The piezoelectric elements are modeled as having a linear relation between the mechanical and the electrical properties. The material properties of a piezoelectric transducer polarized in x-direction given in IEEE standard format [51] were used to define the elasticity matrix, the piezoelectric stress coupling matrix, and the permittivity matrix in Eq.(1) of the Appendix.

To model the electromechanical behavior of the d35 PZT piezoelectric transducers, the FE multiphysics analysis was performed using a 20-node coupled-field solid element (SOLID226) which has piezoelectric capabilities including direct and converse piezoelectric effects. This element has five degrees of freedom (DOF) per node including voltage, temperature and nodal displacement in three coordinate directions. The aluminum plates and the adhesive layer were meshed with a structural solid element, SOLID185. The DOF of structural elements only include nodal displacement in coordinate directions.

The contact behavior between the adhesive and the aluminum layers were defined as fully bonded joints to prevent sliding and separation between the laminate layers. Contact elements (CONTA174) and target elements (TARGE170) were used to mesh all interface regions. In general, it is required to have a mesh size that is at least 1/10 of the wavelength to accurately simulate the wave propagation [53]. Thus, the element size of the couple-

field elements and structural elements were set 0.5 mm. The piezoelectric actuator defined as PZT-1 in Figure 5-1 was excited with a 5-peak Hann windowed signal at 30 kHz through the application of alternating voltage on all the nodes located on its top and bottom surfaces. The piezoelectric sensor defined as PZT-2 was simulated through the application of a voltage coupling on its top surface and a constant voltage on its bottom surface. To prevent rigid body motion, the bottom corners of the laminate structure were fixed in all directions. Furthermore, a numerical damping of 0.1 was set to stabilize the numerical integration scheme for the transient dynamic analysis. More details on multiphysics modeling are available in ANSYS17.0 documentation [54].

5.2. Actuation and Sensing of Flexural Waves

The actuation signal and the received signal by d35 PZT piezoelectric transducers were plotted in Figure 5-2. The first wave packet in the received signal can be identified as the actuation signal followed by its reflection from the boundaries. The time of flight (TOF) of the flexural waves to travel 115 mm from the actuator to the sensor was estimated 104 μsec by using 1% threshold of the maximum voltage. The group velocity of the flexural waves propagating in the laminate structure was calculated approximately 1105.8 m/sec.

The flexural waves are dispersive waves meaning that the wave speed changes with frequency. The effect of dispersion phenomenon is always manifested on the shape and amplitude of a propagating wave packet by being widened because the wave packet contains a range of frequencies introduced by the windowing process. Therefore, to qualitatively examine the dispersion effect of the flexural waves, the time-frequency spectrums of the actuation signal and the received signals were determined using the

Short-time Fourier Transform. The spectrums were displayed in Figure 5-3. By comparing the spectrums of the actuation signal with the first wave packet in the received signal, the dispersion effect on the first arrival is slightly noticeable and that can be attributed to the short distance between the PZT transducers.

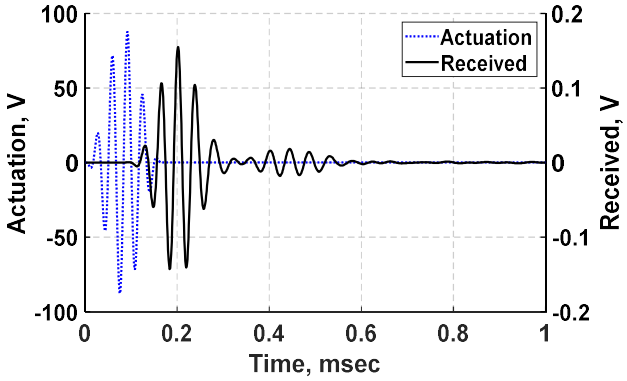

Figure 5-2: Simulation of laminate structure: a) actuation signal at 30 kHz; b) received signal.

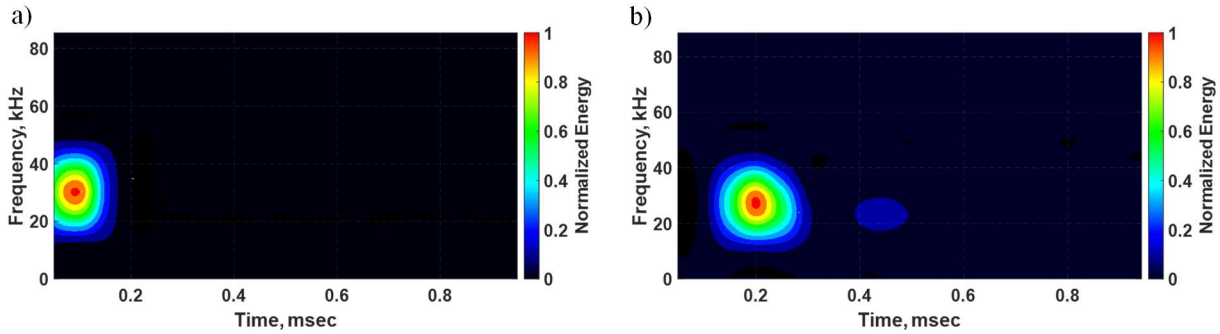

Figure 5-3: Time-frequency spectrums of: a) actuation signal, and b) received signal from d35 PZT sensor.

In Figure 5-4, the distributions of elastic strain wave propagation from the actuator to the sensor in x - direction are displayed at 80 μsec for each layer of the laminate structure: top plate, adhesive layer, and bottom plate. Each wave appears as a semicircle with different magnitudes traveling and spreading in a conic shape from the source actuator. It can also be observed from the simulation snapshots that the d35 PZT actuator creates directional waves which propagate in two opposite directions. Furthermore, there is

almost a complete absence of the flexural waves in the transverse direction (z - axis) with respect to the source reinforcing the directionality of d35 PZT actuators to generate flexural waves mainly concentrated along the direction of wave propagation. The amplitude of the strain waves in the substrates are the same but their distributions are antisymmetric about the adhesive layer.

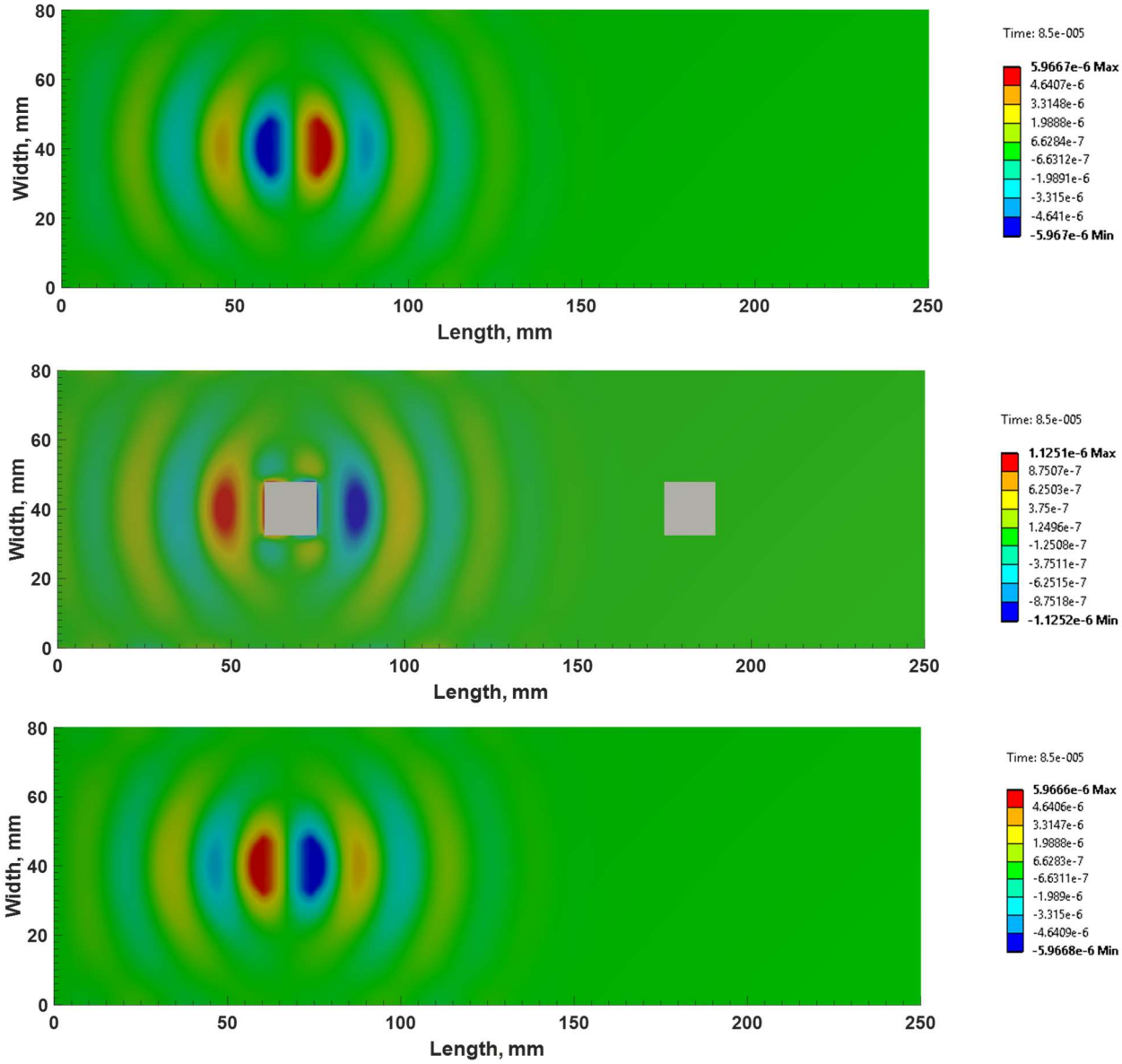

Figure 5-4: Full-field view of elastic strain wave propagation in x - direction at 80 μsec (top to bottom): top plate, adhesive, and bottom plate.

This behavior can also be observed from the distributions of normal displacements and in-plane shear stress of flexural waves at 30 kHz shown in Figure 5-5. The distributions of flexural waves were calculated for a set of nodes along the thickness located at 100 mm from the left vertical boundary and 40 mm from the horizontal boundary. The distributions were obtained at 80 μsec. The shaded region in Figure 5-5 represents the position of the adhesive layer with respect to the upper and lower substrates.

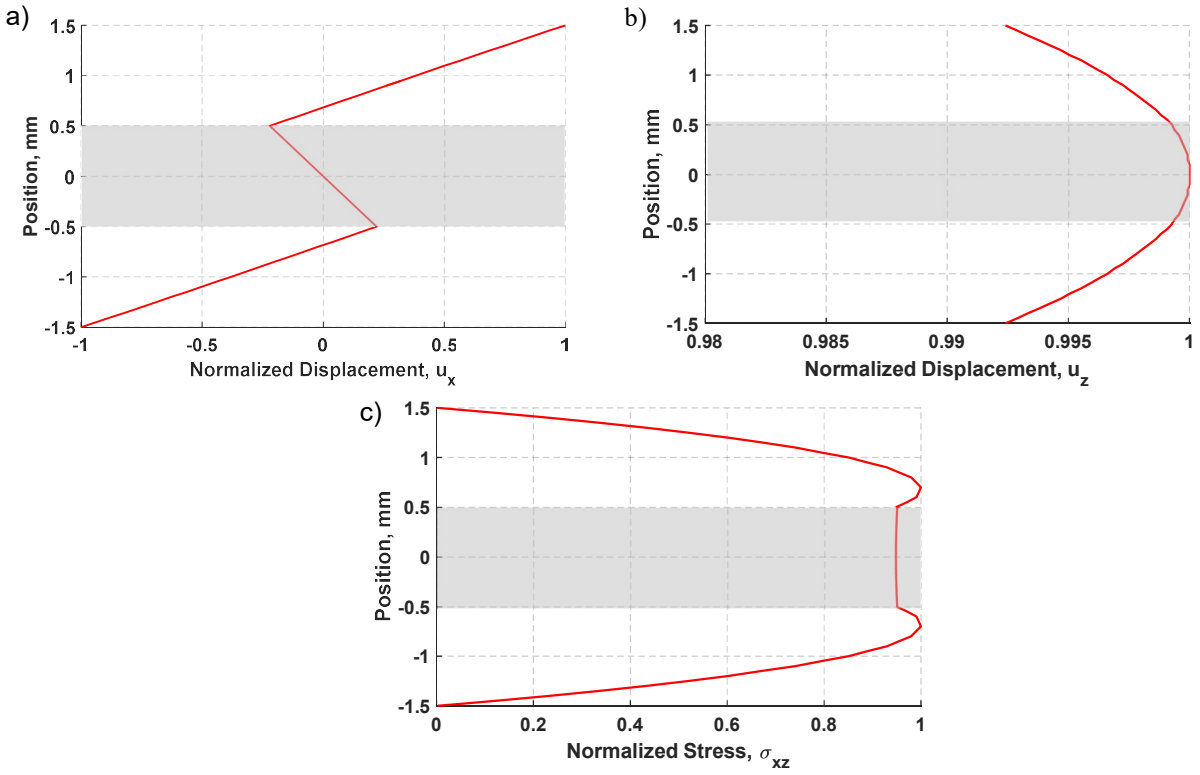

Figure 5-5: Through-thickness distributions of flexural waves in laminate structure at 80 μsec for normalized: a) axial displacement; b) vertical displacement; c) in-plane shear stress.

In Figure 5-5a, the normal distribution in the direction of wave propagation shows linear displacement through each layer indicating the top plate under maximum tension while the bottom plate under maximum compression. The adhesive layer and the whole

laminate structure undergo the action of flexural forces induced by the d35 PZT actuator embedded in the bondline. In Figure 5-5b, the distribution of lateral displacement is maximum at the neutral axis, but the difference between the extreme values is negligible suggesting a uniform sinusoidal lateral displacement over the period of wave propagation in the laminate plate.

The distribution of transverse shear stress in Figure 5-5c shows a constant and comparatively high stress over the thickness of the adhesive layer while an increasing shear stress profile from the outer surface to the interface region in the aluminum substrates making the location of d35 sensors within the bondline an optimal location to sense and actuate flexural waves with minimal loss of energy. The full-field distribution of laminate layers as well as the distributions of normal displacements and in-plane shear stress exhibit the profile of flexural waves demonstrating the capability of d35 PZT transducers to effectively actuate and sense flexural waves within the bondline of laminate structures.

In Figure 5-6, the distribution of elastic wave propagation in the adhesive layer from the actuator to the sensor is displayed at various time instances. It can be observed at 40 μsec, the shear-mode actuator creates directional waves which travel in two opposite directions predominantly along the centerline of the multilayered structure. The antisymmetric waves are expected to travel along x - direction with vertical displacement in z - direction. The symmetric Lamb waves however have the wave propagation and particle displacement in x - direction. It is worth noting the shear-mode PZT sensor predominantly captures antisymmetric waves in the media.

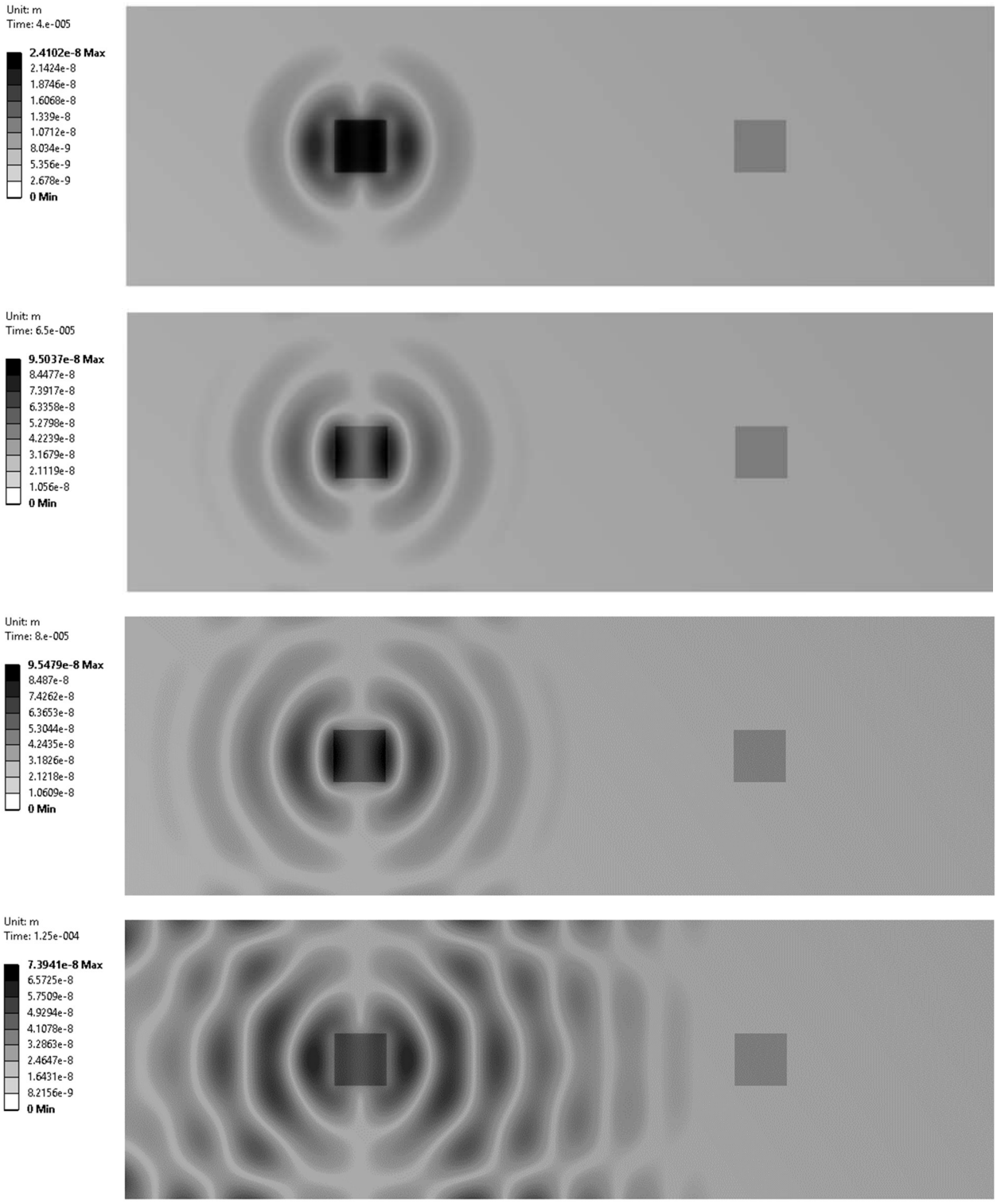

Figure 5-6: Total deflection full-field view of elastic waves propagation in the bondline at (top to bottom): 40 μsec, 65 μsec, 80 μsec, and 125 μsec.

The distribution of ultrasonic waves in the adhesive layer shows each wave is represented as a semicircle at different magnitudes and travels in a cone form from the source. It can be noted that the wave fronts of the outermost semicircle which has traveled farthest from the source reaches the horizontal and vertical boundaries at about 80 μsec. At about 125 μsec, the reflection from the boundaries interferes with the new emitted waves resulting in a profile distortion of the propagated waves.

Consequently, the interference in the outer waves caused the waves to alter their profile into a form of vertical lines at this time instance. Because the reflection from the right vertical boundary caused destructive interference, the intensity of the waves traveling towards the right vertical boundary appears to be reduced in magnitude as compared to the waves propagating in the other direction. Thus, the actuation signal and its intensity are persevered in the horizontal direction in which the wave is traveling towards the sensor. It is also worth noting from Figure 5-6 there is a complete absence of the antisymmetric waves in the transverse direction (y - axis) with respect to the source. Therefore, a damage located in the blind spot is not expected to be reflected on the received signal. On the other hand, there are shear horizontal waves excited by the actuator in y - direction. They are directional waves traveling in y - direction with a particle displacement in x - direction.

5.3. 2D FE Modeling

Multiphysics analysis: 3D multiphysics models often require high performance computing machines. Reducing the computational time while also maintaining reasonable accuracy is often a desirable choice in numerical analyses. To reduce the computational time, 2D multiphysics analysis was conducted for comparison of waveforms obtained

from 2D multiphysics and 3D multiphysics analysis. The width-to-thickness ratio of the multilayered structure shown in Figure 5-1 is relatively large such that the plane strain condition can be satisfied for the 2D analysis. The shear-mode PZTs were simulated as piezoelectric bodies using a coupled-field element, PLANE223. This element has 8 nodes with four degrees of freedom per node including temperature, voltage, and nodal translations in x and y directions. The modeling procedure of shear-mode PZT transducers is similar to the procedure of 3D multiphysics analysis discussed in the previous section. The actuator was modeled through the application of voltage coupling and alternating voltage on the nodes located at the top and bottom edges. The sensor was simulated by applying voltage coupling and a constant voltage on one edge.

The aluminum and the adhesive were meshed with a higher order 2D element, PLANE183. This element is well suited for this application because it has quadratic displacement behavior with 8 nodes having two degrees of freedom at each node (translations in x and y coordinates). The same actuation signal that was used in 3D multiphysics model was also used herein for comparison purposes.

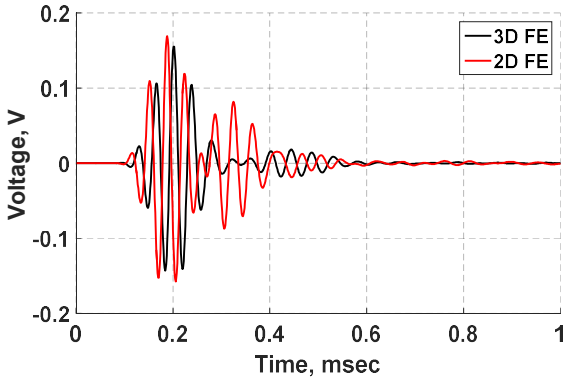

Figure 5-7: Comparison between 3D FE and 2D FE waveform signals received by bondline-embedded d35 PZTs.

The voltage signals produced by the bondline-embedded d35 sensor from 3D FE and 2D FE simulations are superimposed in Figure 5-7 for comparison. By simulating the laminate structure using a 2D model the computation time was reduced by a factor of 300. The two voltage signals shown in Figure 5-7 show a good agreement in their overall shape and amplitude of the first wave packet. The second wave packet in each signal was closely inspected and found to be due to reflection from the boundaries. The differences of the phase and amplitude of the second wave packet between the 3D and 2D models were attributed to the combination of the damping factor applied to the 3D model to ensure convergence and the modeling nature of 2D and 3D models. The 2D simulation inherently imposes a plane strain condition in the y - direction effectively modeling straight crested waves rather than conically propagating waves. The first arrival wave packet is very similar in form between the two simulation results. The phase lead in the 2D signal represents slightly faster wave propagation with a time difference of about 6 μsec resulting in 1169.5 m/sec group velocity for the FE flexural waves. The key result was that the signal from the first wave packet produced by 2D and 3D models were found to be comparable in shape and frequency content with minor time and amplitude differences.

Table 5-1: Comparison of computational resources for 2D and 3D models of laminate structures.

	2D Model	3D Model
Total number of DOF	720441	2258508
CPU time (sec)	3112	900161

By simulating the laminate structure using a 2D model, a significant reduction in computational time was reported in Table 5-1 as compared to 3D model. The overall

behavior of flexural waves obtained from 2D FE simulation and experiment was comparable indicating 2D model is reasonably accurate for detection of joint defects in laminate structures.

Structural analysis: For the sake of completeness, this section focuses on investigating the applicability of simulating the structural shear forces induced by shear-mode PZTs for comparison of waveforms obtained from multiphysics analyses. In Figure 5-8, the multilayered structure with two shear-mode PZTs placed in the bondline is considered herein for structural analysis. The shear strain induced by the actuator was calculated using the piezoelectric coupling relation given as

$$s_5 = d_{35} E_3 \tag{5.1}$$

This shear strain is transmitted in the bondline in a form of vertical shear waves propagating in x - direction and a particle displacement in z - direction. Therefore, the traction forces from the actuator were simulated via a nodal displacement applied to the nodes corresponding the location of the actuator. This modeling approach often known as pin-force model is the first order approximation of structural mode shape of a shear-mode PZT. Thus, it is only valid for low actuation frequencies that are below the first natural frequency of the shear-mode PZT. The antisymmetric Lamb waves which are of interest to this study are expected to be present in the 2D multilayered structure. On the other hand, shear horizontal waves are expected to be completely absent because their propagation direction in y - direction.

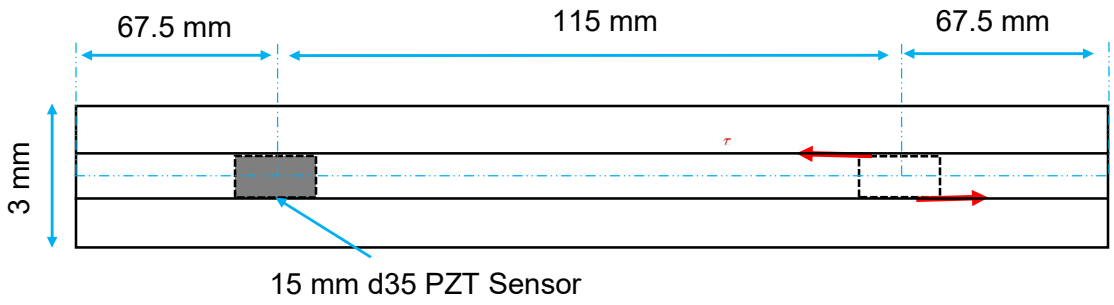

Figure 5-8: A laminate structure with shear traction simulating forces induced by a shear-mode PZT placed in the bondline.

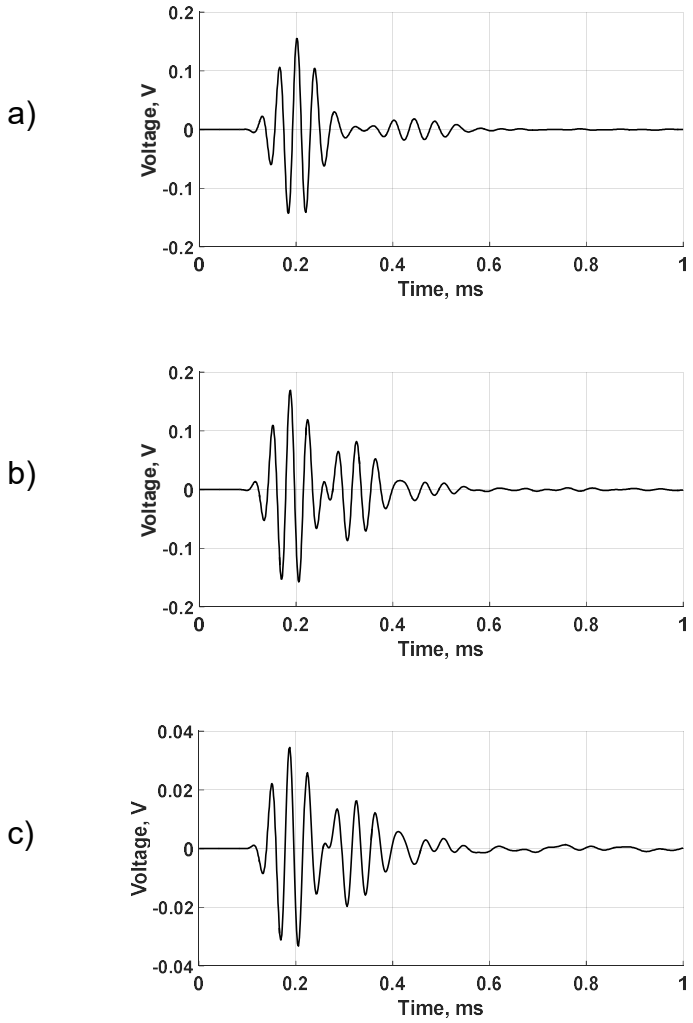

Figure 5-9: A laminate structure with shear-mode actuation for waveforms from: a) 3D multiphysics; b) 2D multiphysics; c) 2D structural analysis.

The actuation signal as well as waveform responses from structural analysis and multiphysics analyses are plotted in Figure 5-9. A 5-peak actuation signal modulated by

Hann window at 30 kHz was kept the same in all models to produce flexural waves in the bondline. Comparing the waveforms from 3D and 2D multiphysics models shows a good agreement in the overall shape of the first wave packet. The second wave packet which is a reflection from the left vertical boundary to the source is over-damped in 3D model. On the other hand, the Lamb waves which are of interest are represented with 2D analyses with reasonable accuracy. The overall behavior of flexural waves obtained from both models is comparable. The waveform response of a pin-force model is displayed in Figure 5-9c. It can be noted that the signals received from 2D structural model and 2D multiphysics model are in good agreement indicating both models are suitable.

5.4. Characteristics of Flexural Waves

From 2D FE multiphysics model, the distributions of normal displacements and stresses of flexural waves in the laminate structure induced by d35 PZT actuator at 30 kHz are displayed in Figure 5-10. The distributions were obtained at 138.3 μsec. The 1D through-thickness distributions were calculated for a set of nodes located at the middle of the structure (152.5 mm) and the shaded regions represent the position of the adhesive layer with respect to the upper and lower substrates. The 2D full-field views for stress components were calculated for a section of the laminate structure located between 147.5 mm and 157.5 mm.

In Figure 5-10a and Figure 5-10b, the normal displacement in x - direction shows linear displacement over each layer with zero displacement at the neutral axis resulting in maximum tension in the upper plate and maximum compression in the lower plate. The distribution of normal displacement in y - direction shown Figure 5-10c is maximum in the substrates and minimum in the adhesive layer, but due to negligible difference between

the extreme values the lateral (y) displacement , it can be considered uniform through the thickness over the period of wave propagation.

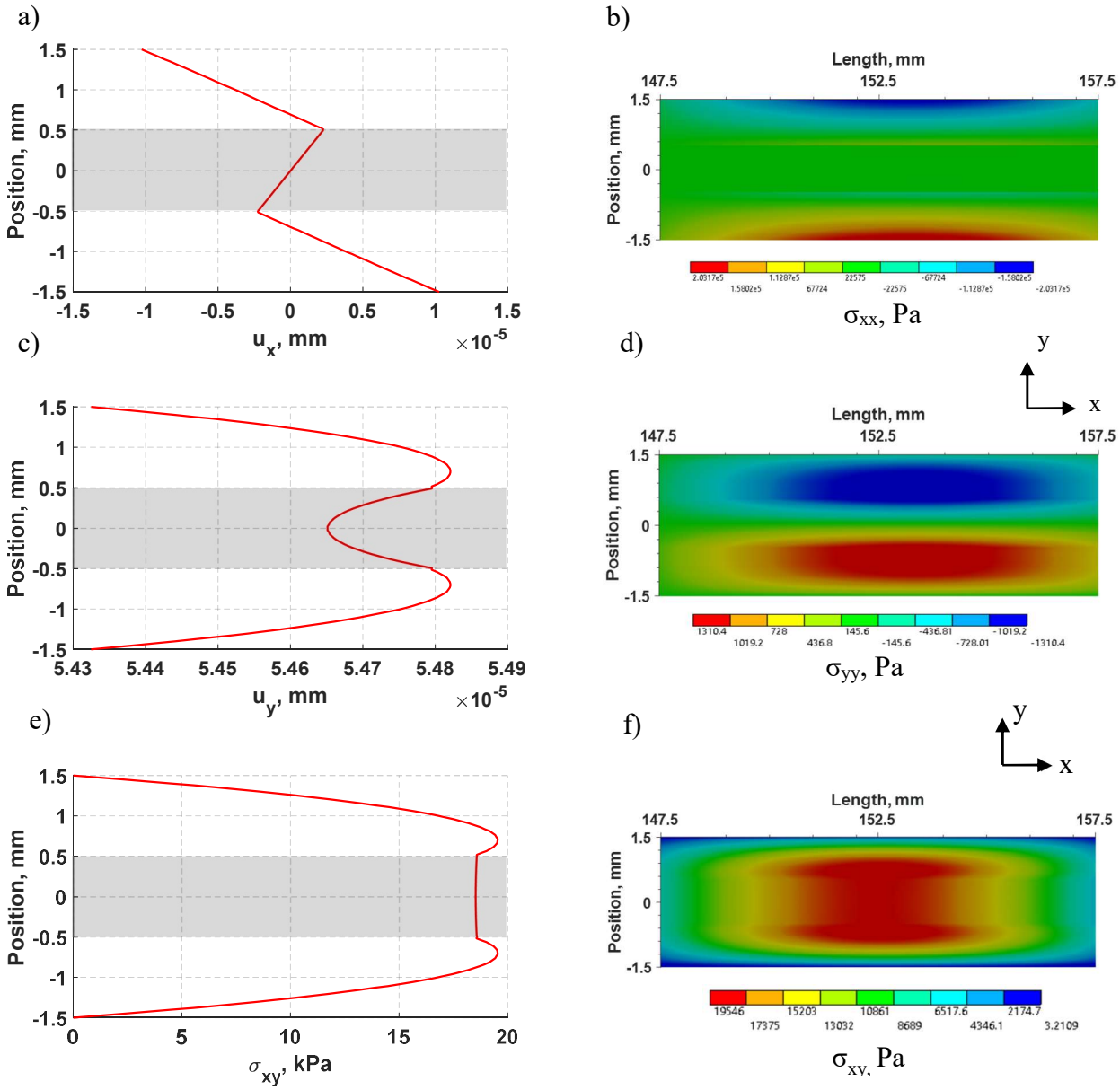

Figure 5-10: 1D through-thickness distributions (left) and 2D full-field view (right) of flexural waves in laminate: a) axial displacement; b) stress in x - direction; c) lateral displacement; d) stress in y - direction; e) and f) in-plane shear stress.

It may be noted from Figure 5-10a through Figure 5-10d that the magnitude of lateral (y) displacement is about five times larger than the axial (x) displacement, but the normal

lateral (y) stress is negligible compared to the axial (x) normal stress. The distribution of shear stress in Figure 5-10e and Figure 5-10f shows an increasing shear stress from the outer surface to the interface region in the aluminum substrates while the adhesive layer maintains a constant and comparatively high shear stress.

The propagating waves exhibit the characteristics of flexural waves which induce high lateral (y) displacement coupled with maximum axial (x) stress in the outer surface and maximum transverse shear stress near the neutral axis of the structure. In summary, a good agreement between experimental and FE voltage signals was achieved supporting the effectiveness of d35 PZT transducers to actuate and sense flexural waves while being embedded the bondline of laminate structures as well as validating the FE modeling procedure for the subsequent analyses throughout this study.

The tuning of a particular wave mode is of considerable importance in damage detection, thus flexural waves generated by shear-mode PZTs were tuned by varying the actuation frequency. In Figure 5-11, the distributions of through thickness displacements and in-plane stresses obtained from nodes located at the middle of the structure (152.5 mm) were plotted for three different frequencies including 20 kHz, 30 kHz, and 40 kHz. The shaded region in Figure 5-11 indicates the location of the adhesive layer with respect to the aluminum substrates. It can be observed from Figure 5-11 an increase in the actuation frequency resulted in magnitude reduction of all normal displacement and stress components. The voltage reduction observed from d35 PZT sensor signal is expected to be predominantly caused by reduction in in-plane shear stress specifically across the thickness of the adhesive layer. A decrease in frequency caused the shear stress distribution to have the maximum shear stress concentrated within the adhesive layer.

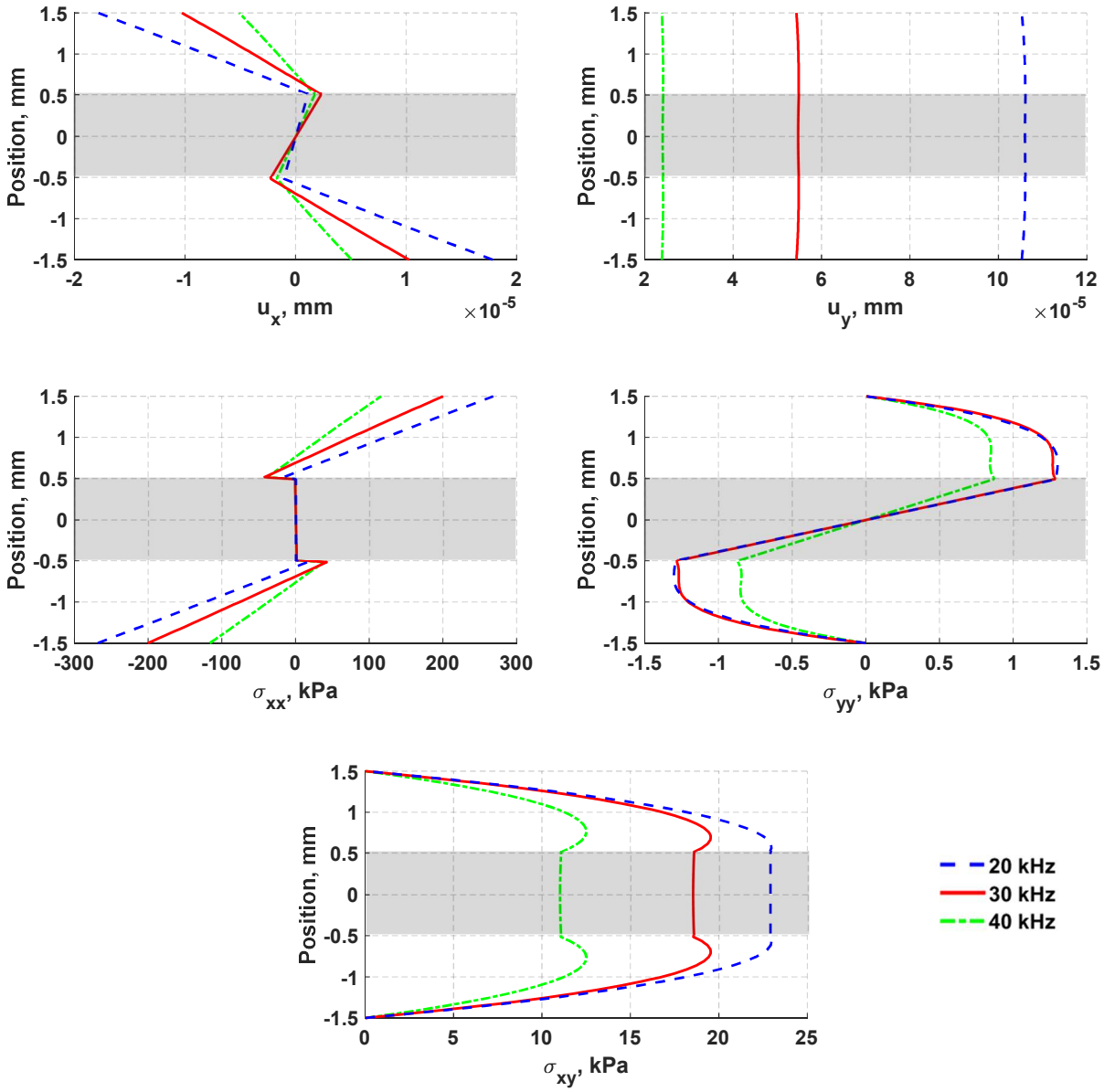

Figure 5-11: Comparison of through-thickness displacements and in-plane stresses of flexural waves at: 20 kHz, 30 kHz, and 40 kHz.

As previously mentioned in the literature, waveforms that generate shear strain have been found to be very effective for detecting joint defects by several researchers [20,22,55]. Therefore, it is important to note that the high level of change of shear stress in the bondline as compared with other existing stresses in the laminate structure provides

an opportunity to design d35 transducer such that the strength of the in-plane shear stress is focused along the thickness of the adhesive layer for inspection of bondlines.

5.5. Summary and Conclusions

A 3D multiphysics simulation of a laminate plate consisting of two d35 PZT transducers sandwiched between two aluminum layers was implemented. A signal processing algorithm based on time-frequency analysis was used to qualitatively examine the dispersion effect of the flexural waves. Full-field distribution of flexural waves in each layer was also investigated to identify the characteristics of propagating waves generated by d35 PZT actuators. The multilayered structure was also simulated using 2D multiphysics analysis and then compared with waveforms obtained from 3D multiphysics analysis and 2D structural analysis. The overall behavior of flexural waves obtained from all FE models was found comparable. The tuning analysis was performed by varying the actuation frequency and examining the distributions of normal displacement and stresses across the laminate thickness. It was also noted that the strength of shear stress can be concentrated across the thickness of adhesive layer at lower actuation frequencies. Therefore, this provides an opportunity to design d35 PZT actuators such that they generate strong in-plane shear strains that target the bondline region for adhesive joint evaluation.

Chapter 6
Properties of Ultrasonic Waves Induced by d35 PZT Actuators: Experimental Validation

This chapter presents an experimental study into the sensing and actuation properties of shear-mode (d35) piezoelectric transducers internally embedded in the bondline of laminate specimens. It begins with describing a signal processing algorithm used for de-noising and transform experimental waveform signals into time-frequency domain. The directionality of d35 PZT actuators was also investigated by comparing waveform signals from a plate-like specimen with a beam-like specimen. The results of this study indicate that d35 PZTs embedded in the bondline have multiple properties that can potentially be employed for ultrasonic SHM.

6.1. Signal Processing Algorithm

Waveform signals are processed using a signal processing algorithm based on time-frequency analysis. The time-frequency analysis is an essential approach in signal processing of non-stationary signals such as guided waves. They are used to provide local information of the processed signal that is of importance to monitor the integrity of a structure. The Short-time Fourier Transform (STFT) is a major algorithmic signal processing method that is commonly used in SHM to extract relevant details on the structural health. The basic concept of STFT is developed from the conventional Fourier Transform (FT). A non-stationary signal is divided into short enough time intervals using a fixed modulation window that are essentially stationary signals [56]. A windowing

process on a segment produces a modified signal at a fixed time. This windowing process is performed as follows

$$S_w(\tau - t) = s(\tau)w(\tau - t) \tag{6.1}$$

In Eq.(6.1), $s(\tau)$ is a short segment of the original signal, $w(\tau - t)$ is the modulation window, and $S_w(t,\tau)$ is the modulated signal at time, $\tau = t$. The FT of S_w yields

$$S_w(t,\omega) = \frac{1}{2\pi}\int_{-\infty}^{\infty} e^{j\omega t} S_w(t,\tau)dt \tag{6.2}$$

In Eq.(6.2), $S_w(t,\omega)$ is called the Short-time Fourier Transform. By squaring the magnitude of the STFTs, the time-frequency distribution can be obtained as [56]

$$P_w(t,\omega) = \left|S_w(t,\omega)\right|^2 = \frac{1}{2\pi}\int_{-\infty}^{\infty} s(\tau)w(\tau - t)e^{-j\omega\tau}d\tau \tag{6.3}$$

In Eq.(6.3), $P_w(t,\omega)$ is also called the spectrogram which contains all time-frequency spectra over the entire time domain. The STFT is a popular time-frequency method in SHM due to its simplicity, robustness, and ease of implementation. Discrete Wavelet Transform was also integrated into this algorithm to improve the signal to noise ratio for experimental signals. The continuous wavelet transform of a function, $f(x)$, with independent space variable, x , can be defined as [50]

$$C(u,s) = \frac{1}{\sqrt{s}}\int_{-\infty}^{\infty} f(x)\psi\left(\frac{x-u}{s}\right)dx \tag{6.4}$$

In Eq.(6.4), $C(u,s)$ is the wavelet coefficients and ψ is the analyzing wavelet. The function, $f(x)$ is decomposed by the mother wavelet, ψ that is translated/shifted by a

factor of *u* and dilated/scaled by a factor of *s*. In practice, the discrete wavelet transform is used to transform a discrete signal to discrete wavelet coefficients in the wavelet domain. Herein, the de-noising process was conducted by decomposing the signal into wavelet coefficients using Coiflet family. There are extensive number of wavelet bases and choosing the appropriate wavelet depends on its ability to efficiently produce maximum number of wavelet coefficients that are close to zero [50].

6.2. Plate-like Specimen

6.2.1. Specimen preparation and experimental setup

This experiment was performed as a proof of concept that validates the capability of bondline-embedded d35 PZT transducers to effectively sense and actuate flexural waves in laminate structures. A schematic diagram of the laminate specimen is shown in Figure 5-1. The laminated specimen considered here is also consisted of two d35 PZTs sandwiched between two 1 mm thick aluminum sheets which were bonded together with an approximately 1 mm thick adhesive layer. The 6061-T6 aluminum sheets were machined to 250 mm x 80 mm in size. The shear-mode PZTs were 15 mm square with a thickness of 1 mm. The selection of these PZTs was based on their affordable cost as well as adequate geometrical and electromechanical tolerances. With the current technology, the availability of thinner PZTs can be achieved with high precision without compromising their mechanical and electrical characteristics. The PZTs were adhered to one aluminum sheet that would serve as a common ground using CW2400 conductive epoxy which has an excellent electrical conductivity and strong mechanical properties [57].

The d35 PZTs were placed 115 mm apart with their polarization direction aligned along x-direction as shown in Figure 5-1. A factor in selecting this design layout was the desire to avoid overlapping signals from reflections. A 30 AWG magnet wire was used for the leads and adhered to the individual terminals of the PZTs using the same conductive epoxy. A two-part paste adhesive Hysol EA9394 with material properties given in Table 1 of the Appendix was then used to bond the aluminum sheets together [58]. This epoxy also served as an insulator protecting the hot terminals of the PZTs from shorting against the second aluminum plate. The thickness of the adhesive layer was controlled by placing 1 mm thick spacers on the corners and applying pressure on the specimen while curing. The final assembly was cured at 66°C for one hour. The thickness of the adhesive layer after curing was measured at approximately 1 ± 0.2 mm.

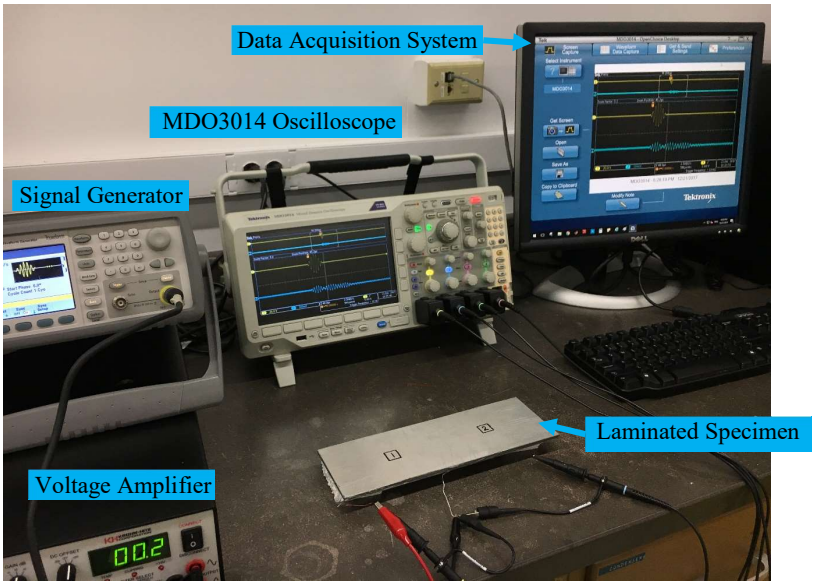

Figure 6-1: Experimental setup of plate-like laminate specimen.

The specimen was supported by small foam blocks placed at its ends to isolate the floor noise from transmitting to the specimen during testing. The full setup is shown in

Figure 6-1. The actuating transducer, labeled as PZT-1, was connected to a KEYSIGHT 33500B Series waveform generator with a Krohn-Hite 7602M Wideband Amplifier to boost the applied voltage. Both d35 PZT transducers were connected to a Tektronix MDO3014 Mixed Domain Oscilloscope to simultaneously record voltage signals across the actuator and the sensor. The specimen was tested in pitch-catch orientation by the 5-peak tone burst signal at 30 kHz. That is the same actuation signal used in FE analysis for comparison purposes.

6.2.2. Comparison of experimental and numerical results

Validation of 3D FE model: The specimen was tested with 5-peak tone burst signal modulated with Hann window with a center frequency of 30 kHz as displayed in Figure 6-2. The received signals from experiment and 3D FE simulation were superimposed in Figure 6-2 in a single plot for comparison. There are two main flexural wave packets in the received signals and they are the actuation wave packet and the reflection from the boundaries. The first arrival ripples are expected to be electromagnetic waves transmitted to the sensor through the wires. By comparing experimental and FE waveform signals in Figure 6-2, it is obvious these ripples do not appear in FE signal because the FE multiphysics model only supports the analysis of piezoelectricity which combines the electrical and structural fields in the laminate structure.

The first wave packet in the FE signal is slightly attenuated as compared to the one in the experimental signal, but their frequency and arrival time match well. On the other hand, the reflection wave packet is significantly over-damped in the FE signal, and this may be due to the numerical damping factor that was imposed on the 3D model to ensure the solver's convergence to the correct solution with a reasonable number (5-10) of

iterations. It is worth noting from Figure 6-2 that the difference between the baseline signals from experiment and simulation is relatively significant to indicate damage presence especially when both signals are obtained from presumably pristine structures.

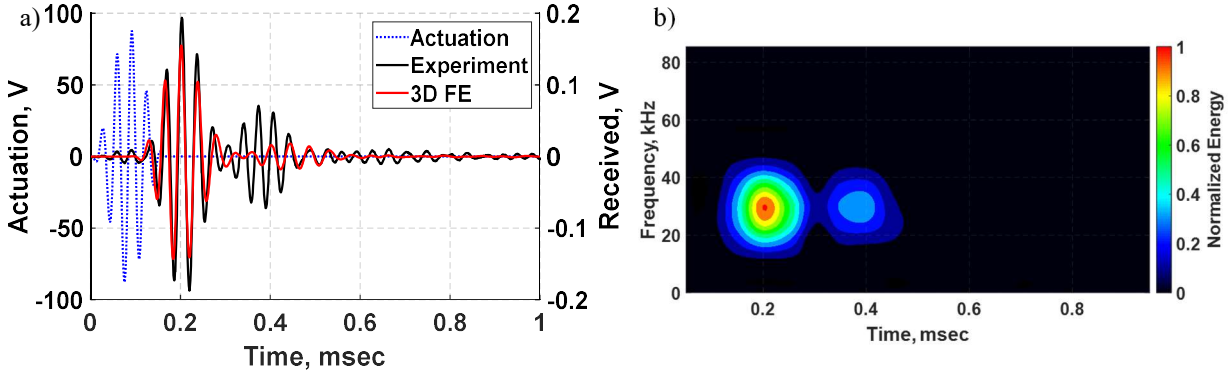

Figure 6-2: Comparison between experimental and 3D FE waveform signals: a) time domain; b) experimental time-frequency spectrum.

The experimental received waveform signal and its time-frequency spectrum were plotted in Figure 6-2. The time-frequency spectrum shows the center frequency of the first wave packet at about 30 kHz with a frequency range of about ±10 kHz. The frequency range was maintained while the signal was slightly dispersed especially for the first wave packet as it traveled a short distance than the reflection wave packet.

Validation of 2D FE model: Ultrasonic multiphysics models often require high computational time due to the necessity for a fine mesh to capture high-frequency waves. Reducing the computational time while also maintaining reasonable accuracy is often a desirable choice in numerical analyses. Therefore, 2D multiphysics analysis of the laminated structure conducted in Chapter 5 is validated here.

The waveform signals received by the bondline-embedded d35 sensor from experiment and 2D FE simulation were superimposed in Figure 6-3. The first arrival packet was represented with reasonable accuracy in 2D analysis. The FE signal however

reached the sensor faster than the experimental signal with a time difference of about 6.8 μsec resulting in 1169.5 m/sec group velocity for the FE flexural waves. Several factors can potentially contribute to various discrepancies between numerical simulation and experiment. A possible factor that may have contributed to the lead time of the FE signal is the assumption of plain strain state which yields z - invariant flexural waves, straight-crested flexural waves in the laminate structure. Therefore, a beam-like specimen is also considered in the subsequent section to further investigate this difference as well as the directionality of flexural wave mode.

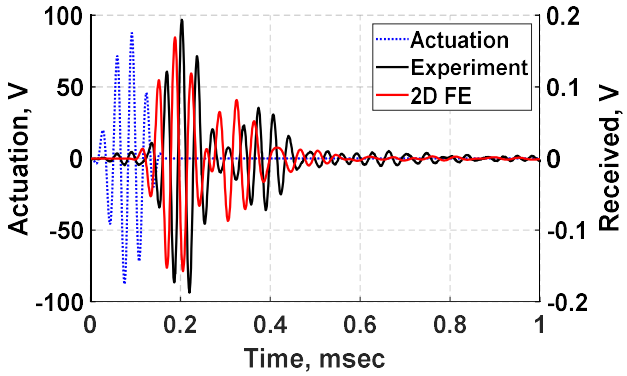

Figure 6-3: Comparison between experimental and 2D FE waveform signals received by d35 PZT sensors.

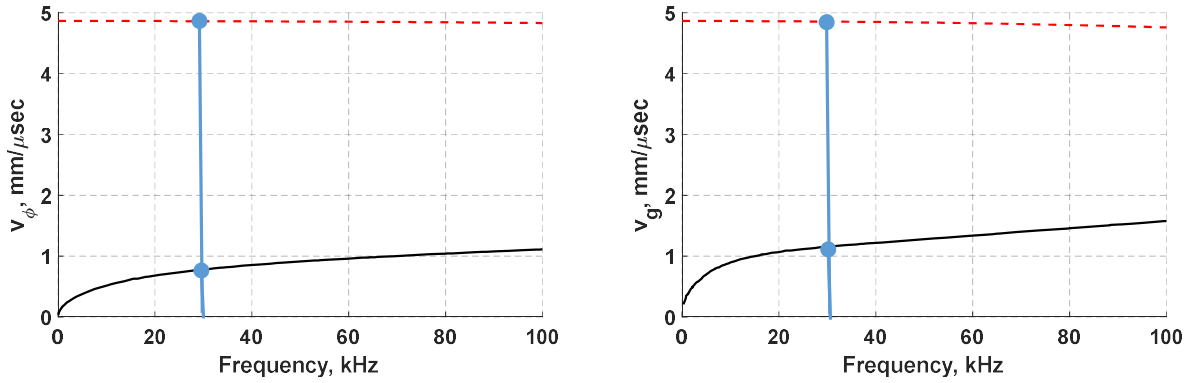

Figure 6-4: Phase velocity (left) and group velocity dispersion curves of a laminate plate with 3 mm thickness.

The dispersion curves of the laminate structure given in Figure 6-4 were calculated using the commercial program, DISPERSE. The ToF and associated group velocity for flexural waves from analytical calculation, experimental measurement, 3D FE simulation and 2D FE simulation are shown in Table 6-1. The ToFs from all methods match very closely, confirming the propagation of flexural waves in the structure.

Table 6-1: Properties of flexural wave propagation.

	ToF (μsec)	Group Velocity (m/sec)
Analytical	103.4	1112.7
Experiment	105.1	1094.2
3D Model	104.5	1100.5
2D Model	98.33	1169.5

The overall behavior of flexural waves obtained from 2D FE simulation and experiment was comparable indicating 2D model is reasonably accurate for detection analyses of joint defects in laminate structures. A good agreement between analytical, FE, and experimental results was achieved supporting the capability of FE modeling to represent the dynamics of the laminate structure with bondline-embedded d35 piezoelectric transducers. Numerical FE and experimental results all indicate an antisymmetric (flexural) wave propagation mode generated by a shear-mode PZT in the bondline of a laminate structure.

6.3. Beam-like Specimen

6.3.1. Specimen preparation and experimental setup

In this experiment, the laminate specimen consisted of two d35 PZTs sandwiched between two 6061-T6 aluminum sheets that were bonded together with a layer of

adhesive. The aluminum sheets were machined to 305 mm x 15 mm x 1 mm in size to study the directionality of flexural wave mode by comparing the voltage signals. This experiment was intended to validate the directionality of flexural waves experimentally.

Shear-mode d35 PZTs were adhered to one aluminum sheet that would serve as a common ground using the conductive epoxy. The d35 PZTs were placed 130 mm apart with their polarization direction align along the aluminum length. The same conductive epoxy was used to attach thin wires to the individual hot terminals of the PZTs. The adhesive thickness was controlled by placing 1 mm thick spacers on the short edges (vertical boundaries) and applying pressure on the specimen while curing. The adhesive layer thickness was measured after curing at 1 ± 0.2 mm. A fully prepared specimen is shown in Figure 6-5.

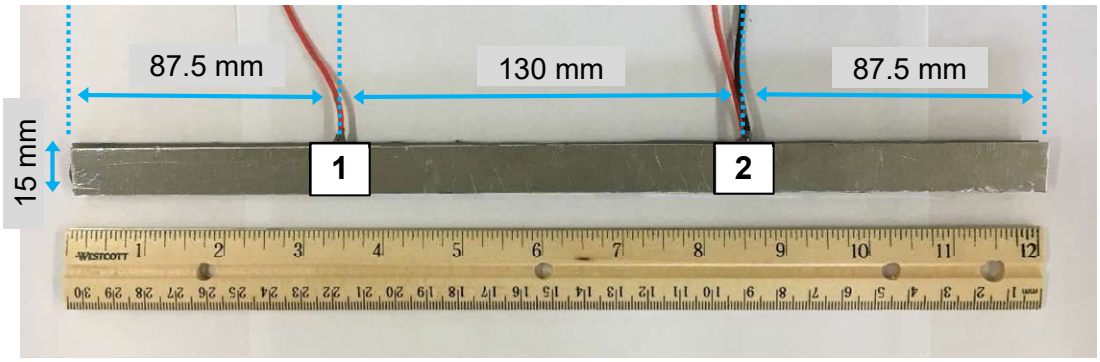

Figure 6-5: Fully prepared sample with two square d35 PZTs embedded within the bondline.

The experimental setup to test the beam-like laminate specimen is shown in Figure 6-6. The d35 PZT transducer labeled as PZT-1 was connected to the waveform generator and the output signal was amplified using the voltage Amplifier. Also, both d35 PZTs were again connected to the Oscilloscope to simultaneously record voltage signals across the actuator and the sensors.

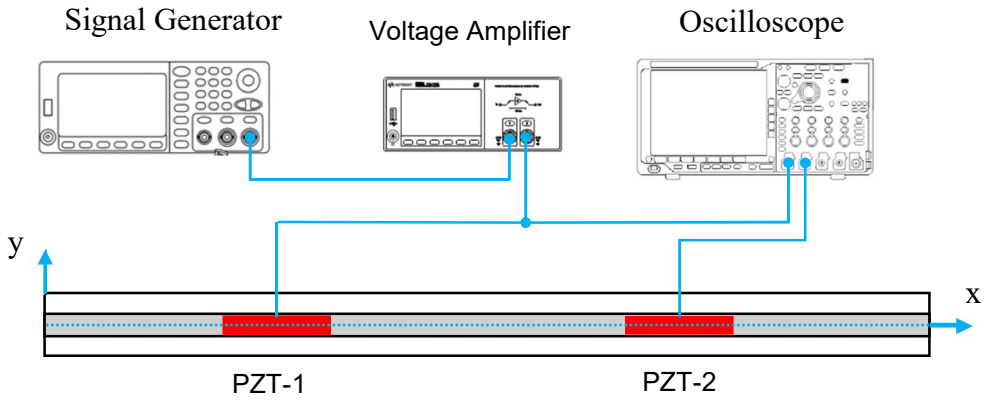

Figure 6-6: Experimental setup for testing a laminate specimen.

6.3.2. Directionality of flexural waves

Throughout this analysis, a 5-peak Hann windowed tone burst signal at 30 kHz was applied to the actuator. The waveform signals produced by the bondline-embedded d35 PZT sensors from experiment and 2D simulation are provided in Figure 6-7. The elastic waves traveled 130 mm and the time of flight for the first arrival wave packet from the actuator to the sensor was measured to be 119.2 μsec and 110.1 μsec for simulation and experiment respectively. Furthermore, the experimental signal also reached the sensor slightly faster than the FE signal with a time difference of about 9.1 μsec resulting in 1089.5 m/sec group velocity for the FE first arrival and 1180.7 m/sec group velocity for the experimental first arrival respectively. As expected, the waveform signals obtained from the beam-like specimen show better agreement to the 2D FE model signals. This analysis combined with the previous wave propagation analysis confirms that flexural waves have strong directionality in laminate structures.

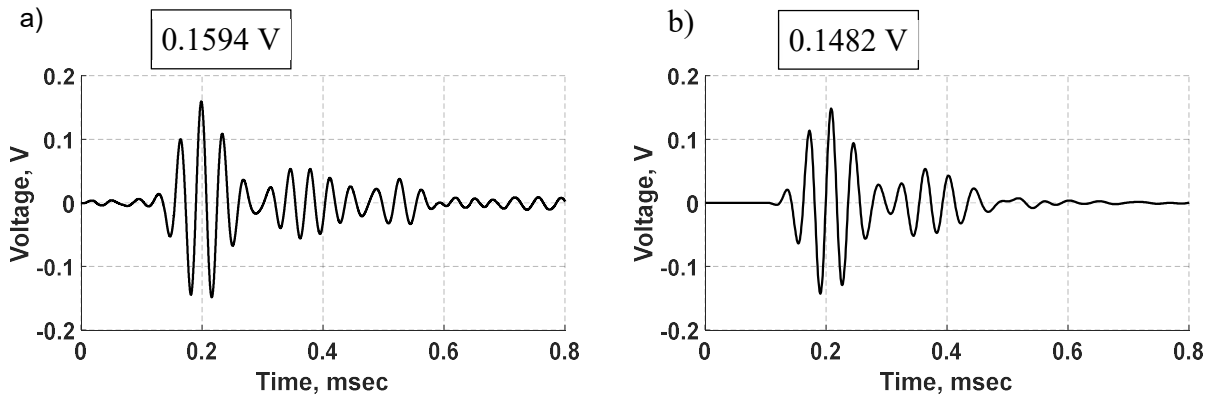

Figure 6-7: Waveform signals sensed by d35 PZT transducers: a) experiment; b) simulation.

Dispersive effects on wave propagation are dependent on the frequencies of both the carrier signal and the modulation window resulting in distortions of both the shape and magnitude of the propagating signal. To qualitatively examine the dispersion effect in this analysis, the time-frequency spectrums of sensed signals were determined and displayed in Figure 6-8. The dispersion effect is slightly noticeable in the spectrums due to the short distance between the PZT transducers. By closely inspecting the spectrums, it can be observed that the dispersion effect is more noticeable on the second wave packet than on the first wave packet and that because the reflection wave packet traveled longer distance than the first major arrival wave packet.

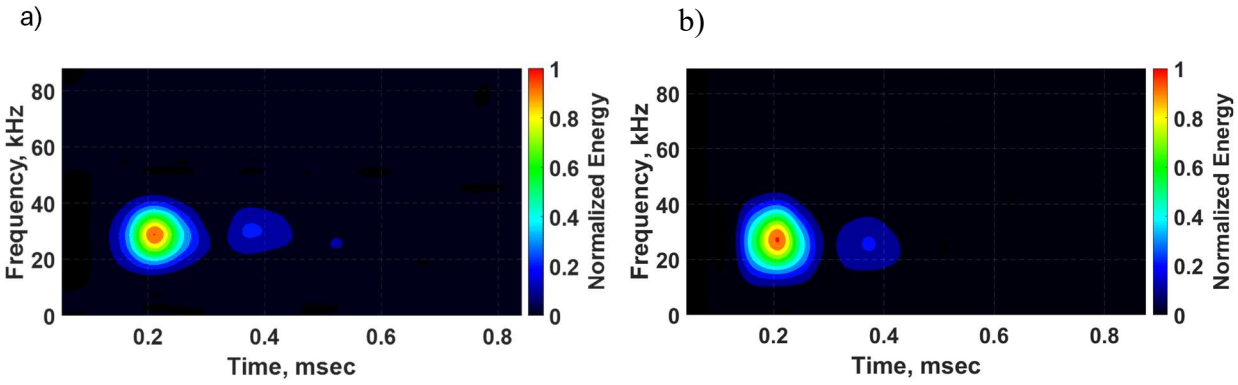

Figure 6-8: Time-frequency spectrums of voltage signals sensed by d35 PZT transducers: a) beam-like specimen; and b) 2D simulation

6.4. Frequency vs. Sensing Voltage Relation

There are several factors that can influence the behavior of actuated flexural waves in laminate structures such as actuation frequency, structural stiffness, and geometry of PZT transducer including its thickness and area. A parametric study was performed investigating the relation between the actuation frequency and the senor output voltage using the validated model. The actuation voltage was kept constant throughout this study and structural deformation was inspected in the model. This was performed by keeping the geometry constant and varying the frequency using simulation and experiments. In this analysis, the beam-like specimen was used.

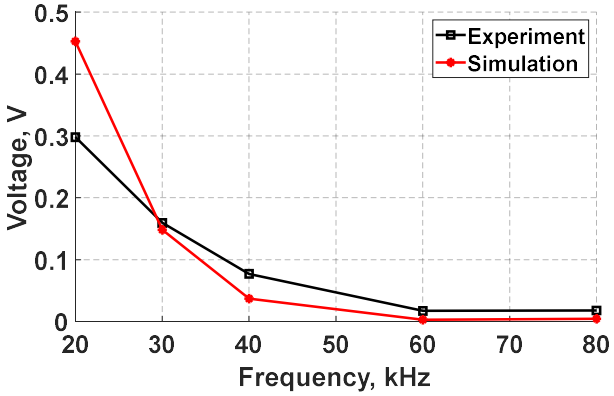

Figure 6-9: Maximum sensor voltage amplitude versus actuation frequency.

The results for the maximum voltage in the sensed signals from simulation and experiment are plotted in Figure 6-9 for comparison. The experimental results were obtained from the same specimen presented in Figure 6-5. Likewise, the simulation results were based on a 2D FE model that was performed by following the modeling procedure discussed in Chapter 5. It can be noted from Figure 6-9 that as the actuation frequency increases, the amplitude of the voltage decreases resulting in weaker voltage signals. The flexural mode was found strongly attenuated above approximately 40 kHz in

the received signals. This frequency range is considered relatively small and that can be attributed to the structural stiffness constraining the movement of d35 PZT actuator as well as the size and shape of the actuator. Structural damping can potentially attenuate the signal, but the distance between the transducers considered too short to cause significant reduction in the magnitude of voltage signals.

6.5. Summary and Conclusions

The sensing and actuation properties of d35 PZT piezoelectric transducers internally embedded within the bondline of laminate structures were investigated experimentally. A plate-like laminate specimen with two d35 PZT transducers embedded within the bondline in a pitch-catch configuration was prepared and tested. The wave propagation analysis validated the results from multiphysics FE simulations for the ability of shear-mode PZTs to actuate and sense flexural waves in laminate structures. The group velocities of experimental and FE voltage signals showed that the elastic waves generated by the d35 PZT actuator exhibit the characteristics of flexural waves across the thickness of the adhesive layer. Furthermore, the voltage signals obtained from experiment and simulation were found in good agreement supporting the effectiveness of d35 PZT transducers to actuate and sense flexural waves while being embedded in the bondline of laminate structures.

A beam-like specimen was also prepared to examine the directionality of flexural wave mode. The results from this specimen and plate-like specimen were found to be comparable confirming the ability of bondline-embedded d35 PZTs for generating directional waves. The frequency versus sensing voltage relation was also investigated by varying the actuation frequency and monitoring the amplitude of the received signals

using FE simulations and then validating the results experimentally. The results from experiment and simulation indicated that there is an inverse relation between the actuation frequency and the maximum sensor voltage.

Chapter 7
Selectivity and Parametric Study of Bondline-embedded d35 PZT Transducers

This chapter presents a parametric study into the sensing and actuation properties of d35 PZT piezoelectric transducers that are embedded inside laminate structures. The parametric study includes the effects of d35 PZT transducer size on the strength of actuation and sensing output signal. The selectivity of d35 PZT sensors was also investigated by generating multiple wave modes in the laminate structure and inspecting the output signals.

7.1. Parametric Study

In Figure 7.1, a doubled-layered aluminum structure with two d35 PZT transducers were simulated. The modeling procedure discussed in Section 5.3 was followed here in to conduct the parametric study. The aluminum substrates have a thickness of 1 mm and a length of 300 mm. The d35 PZTs are placed 130 mm apart and 125 mm from the boundaries with their polarization direction aligned along the length.

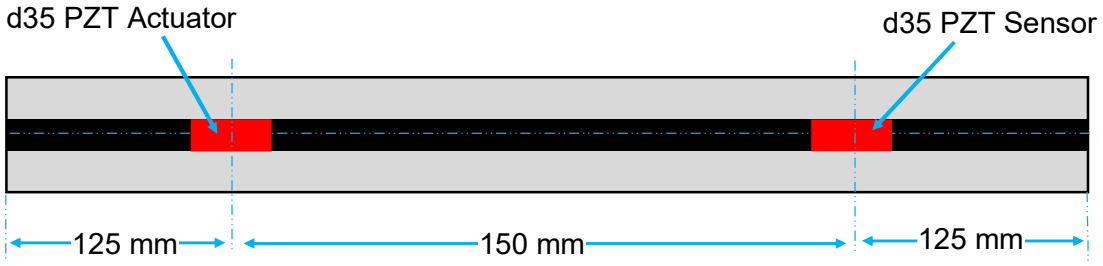

Figure 7.1: A double-layered aluminum structure with two d35 PZT transducers placed in the bondline.

The thickness of the adhesive was kept constant in this analysis in order to maintain constant structural stiffness throughout the analyses while varying the thickness and

length of d35 PZT transducers. However, the geometry of both transducers was varied simultaneously for each simulation. A 5-peak Hann windowed tone burst signal with a center frequency of 30 kHz was used throughout this study.

7.1.1. d35 PZT thickness

To analyze the thickness effects on sensing and actuation of bondline-embedded d35 PZTs, the maximum in-plane shear stress generated by the actuator and the maximum voltage produced by the sensor were plotted against the PZT thickness as the thickness was varied from 0.1 mm to 1 mm in 0.1 mm increments. Inspection of Figure 7.2a reveal that the actuation strength of d35 PZT shows complex behavior. Small thicknesses show the strongest actuation which diminishes as thickness increases until a thickness of 0.5 mm is reached. At this point there is an abrupt drop in actuation strength with minimal variation as thickness continues to increase. In Figure 7.2b, an opposite behavior was observed from d35 PZT sensor for the same thickness indicating that thicker d35 PZT sensors can produce stronger output voltage signals than thinner d35 PZTs.

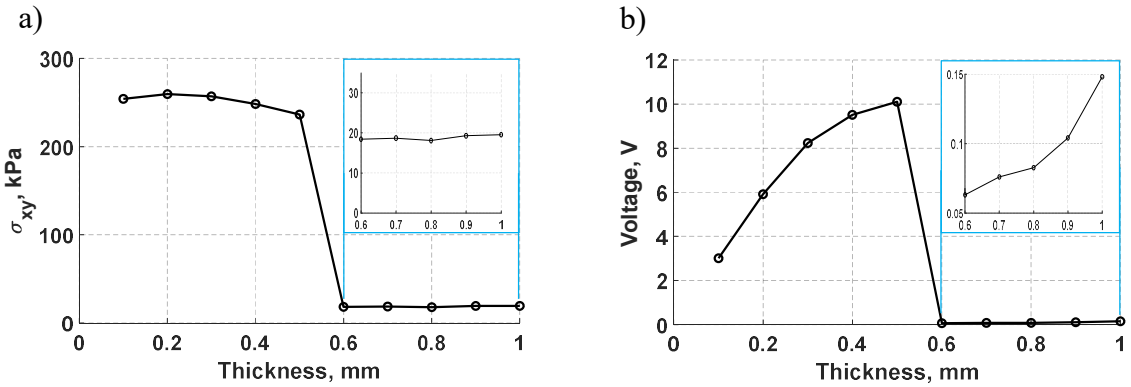

Figure 7.2: Influence of thickness: a) maximum in-plane shear-stress generated by d35 PZT actuator, and b) maximum voltage produced by d35 PZT sensor.

The low voltage amplitudes at thickness greater than 0.5 mm in Figure 7.2b can be attributed to the low actuation strength of thick d35 PZT actuators. The abrupt shift in actuation shown in Figure 7.2a was further examined by analyzing the structural deformation of 1 mm and 0.5 mm d35 PZT actuators. The normal displacements displayed in Figure 7.3 were obtained from a set of nodes located at the left vertical edge of both d35 PZT actuators. It can be observed from Figure 7.3 that 1 mm d35 PZT actuator generates higher axial (x) displacement but lower lateral (y) displacement than 0.5 mm d35 PZT actuator indicating a radical change in the response of bondline-embedded d35 PZT actuator when its thickness reduced below 0.5 mm.

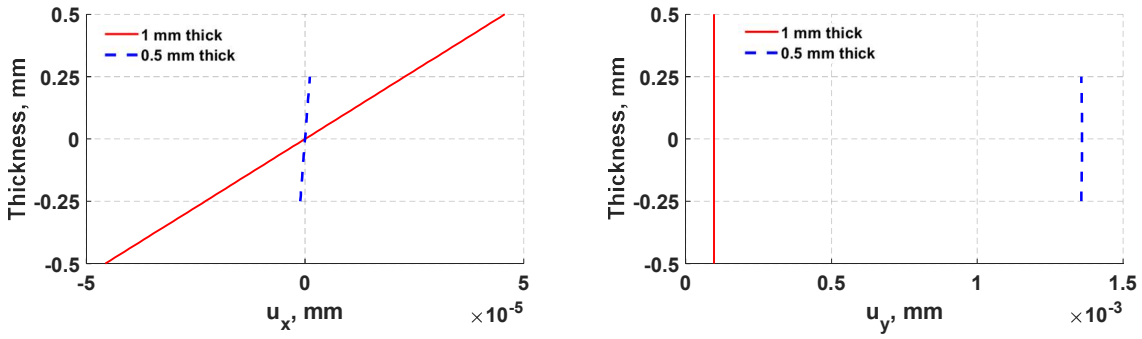

Figure 7.3: Comparison of through-PZT thickness displacements for 1 mm actuator (red solid line) and 0.5 mm actuator (blue dashed line).

Furthermore, the total deformation of the actuators embedded in the bondline of the laminate structure are displayed in Figure 7.4. The results indicate that 1 mm d35 PZT primarily exhibits shear mode actuation to produce flexural waves while 0.5 mm d35 PZT shows flexural mode actuation. This general behavior is believed to be a combined effect of the change in electric field intensity in the actuator as the thickness changes along with the stiffness ratio of the actuator relative to the structure. The results indicate that the stiffness ratio is the main factor for the transition in the behavior of the bondline-embedded PZT transducer at 0.5 mm. It should be noted from Figure 7.2 that there is an optimal

stiffness ratio for which d35 PZT actuators generate strong flexural waves in a laminate structure. Further investigation is necessary as outlined in Chapter 10.

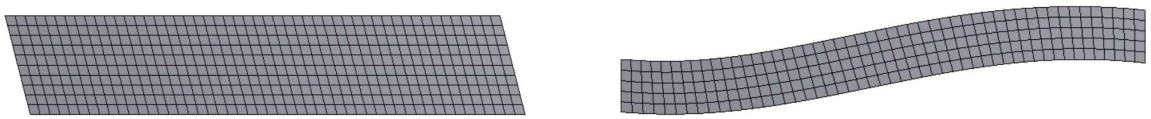

Figure 7.4: Total deformation of bondline-embedded d35 PZT actuators with thicknesses of 1 mm (left) and 0.5 mm (right).

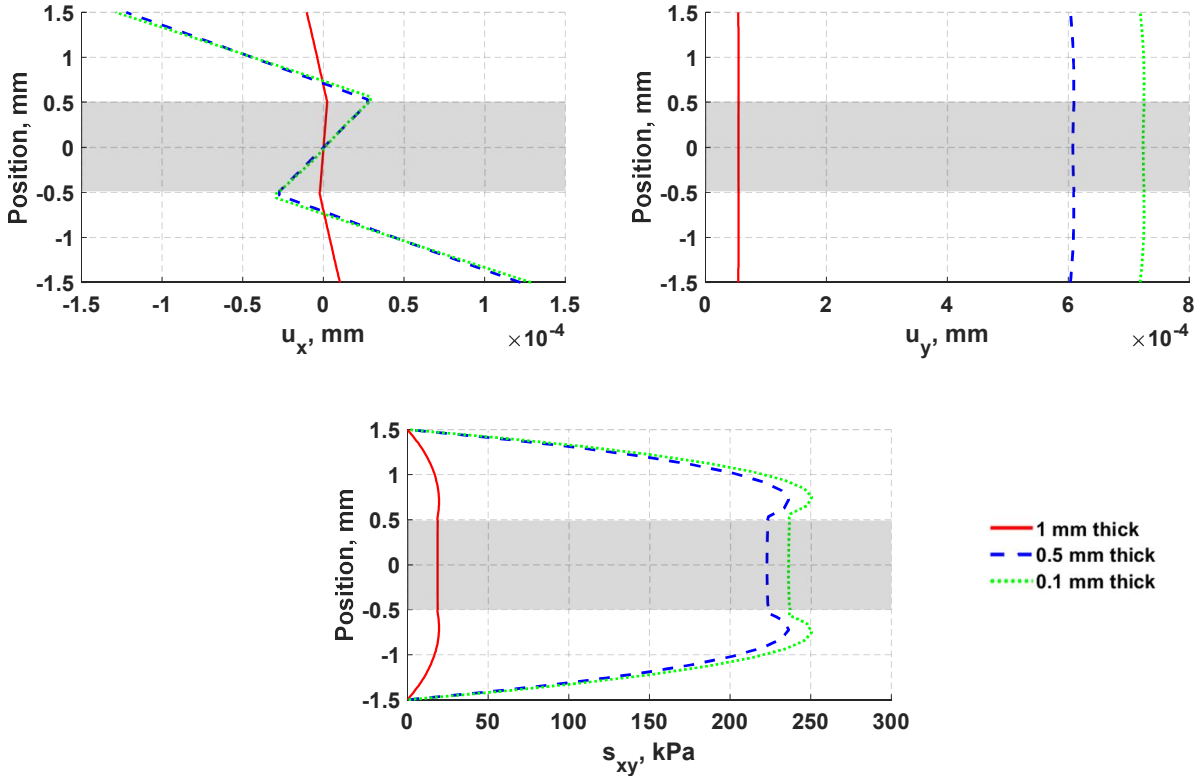

Figure 7.5: Comparison of through thickness displacements and in-plane stresses of flexural waves at 30 kHz with varying the thickness of d35 PZTs.

The distributions of through thickness normal displacements and in-plane shear stress for 0.1 mm, 0.5 mm, and 1 mm actuators are also provided in Figure 7.5. The effect of varying PZT thickness on each normal displacement component is not linear showing higher change on lateral (y) displacement than axial (x) displacement. However, the

lateral (y) displacement of flexural waves is expected to have little influence on d35 PZT sensors especially when the propagating waves have a long wavelength of 39 mm as in this case. A d35 PZT sensor is fundamentally efficient in sensing in-plane shear stress because these waves align well with its natural vibration mode as shown in Figure 3.18. Therefore, d35 PZT sensors are not expected to be capable of sensing in-plane symmetric axial (x) displacement. This concept will be further examined in the next section.

7.1.2. d35 PZT length

The length of bondline-embedded d35 PZT transducers was also varied from 1 mm to 15 mm. The maximum shear stress which represents the actuation strength herein was monitored while varying the PZT length and plotted in Figure 7.6.

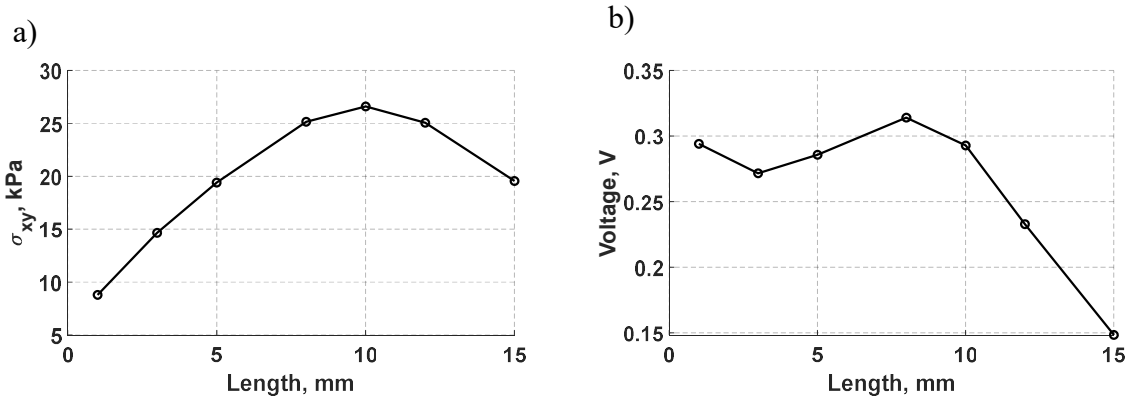

Figure 7.6: Influence of length on: a) maximum in-plane shear-stress generated by d35 PZT actuator, and b) maximum voltage produced by d35 PZT sensor.

As can be noted from Figure 7.6a, the actuation strength increases and reaches its maximum level at 10 mm and then decreases as the actuator approaching 15 mm in length. To analyze the sensing performance, the maximum voltage produced by d35 PZT sensors were recorded and plotted against their length in Figure 7.6. d35 PZT sensors

have higher sensitivity for the propagating waves when shorter d35 PZT sensors are used as can be discerned from Figure 7.6b.

7.2. Selectivity of d35 PZT Sensors

When ultrasonic waves propagate through a structural defect, the interaction of waves and the defect often cause wave scattering and mode conversion. Therefore, a laminate structure with a surface notch was simulated using FE multiphysics analysis to demonstrate the selectivity of bondline-embedded d35 PZT sensors to different modes propagating simultaneously in a structure. In Figure 7.7, a laminate specimen with two d35 PZT transducers (3 mm x 0.1 mm) internally embedded in the bondline and d31 PZT sensor (6 mm x 0.25 mm) mounted on the surface.

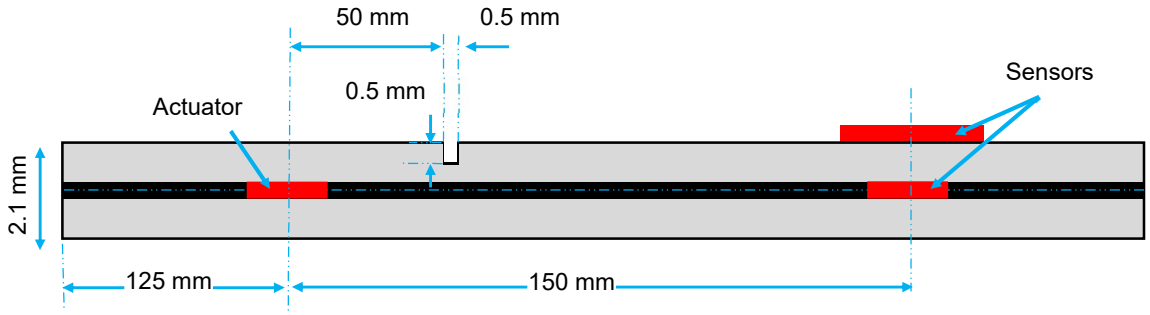

Figure 7.7: Notched laminate structure with two d35 PZT transducers embedded in the bondline and d31 PZT sensor mounted on the surface.

A square surface notch of 0.5 mm width and depth was introduced at 50 mm from the actuator. The distance between the transducers and the location of the notch was determined such that the scattered modes would not overlap for demonstration purposes of d35 sensor's selectivity. The d31 PZT was integrated in the model to highlight the selectivity characteristics of d35 PZT sensor by comparing the sensed waveform signals obtained from both d35 PZT and d31 PZT sensors. The material properties of the laminate

structure are given in Table 1 of the Appendix. A 5-peak Hann windowed actuation signal at 250 kHz was applied to the actuator to generate flexural (antisymmetric) waves in the laminate structure. The dispersion curves including phase velocities and group velocities of the fundamental Lamb modes were calculated using DISPERSE. It can be noted from the dispersion curves in Figure 7.8 that at 250 kHz actuation frequency, the symmetric mode is expected to travel faster than the antisymmetric mode.

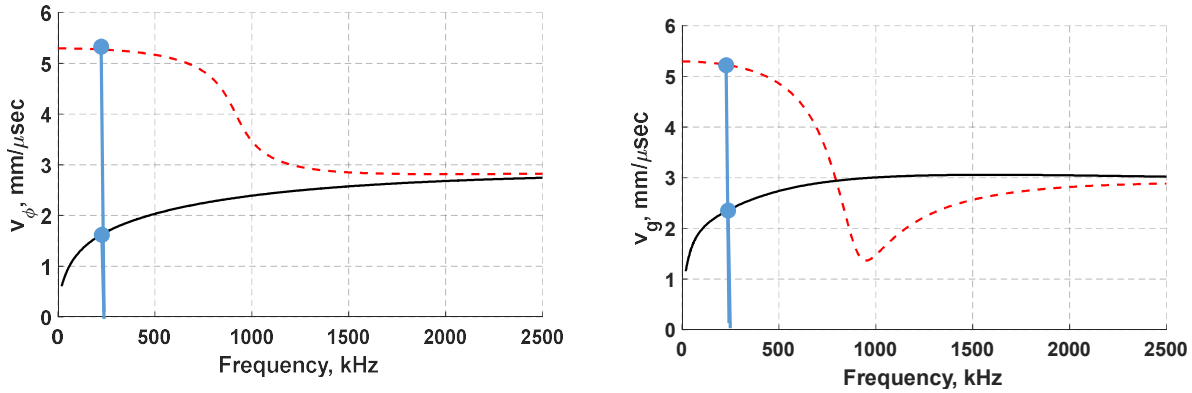

Figure 7.8: Phase velocity (left) and group velocity dispersion curves of a laminate plate with 2.1 mm thickness.

In Figure 7.9, the voltage signals from pristine state (black) and damaged state (red) are superimposed for comparison purposes. The propagating waves were collected without a notch identifying this state as pristine state and the damaged state defined with the notch being inflicted on the surface. As can be quickly noticed, the signals from surface-mounted d31 PZT sensor exhibit multiple modes propagating in the structure whereas the signals from bondline-embedded d35 sensor only shows sensitivity to the antisymmetric signal that was present in both pristine and damaged states. In the d31 sensor signal, two extra wave packets were generated due to the presence of notch as shown in Figure 7.9a. The first wave packet did not appear in the signal from the pristine

sample and was identified as a symmetric mode that resulted from mode conversion, that occurred at the notch. The next wave packet was very similar to the pristine signal and was an antisymmetric mode. The third wave packet was the reflection of the symmetric mode from the boundary.

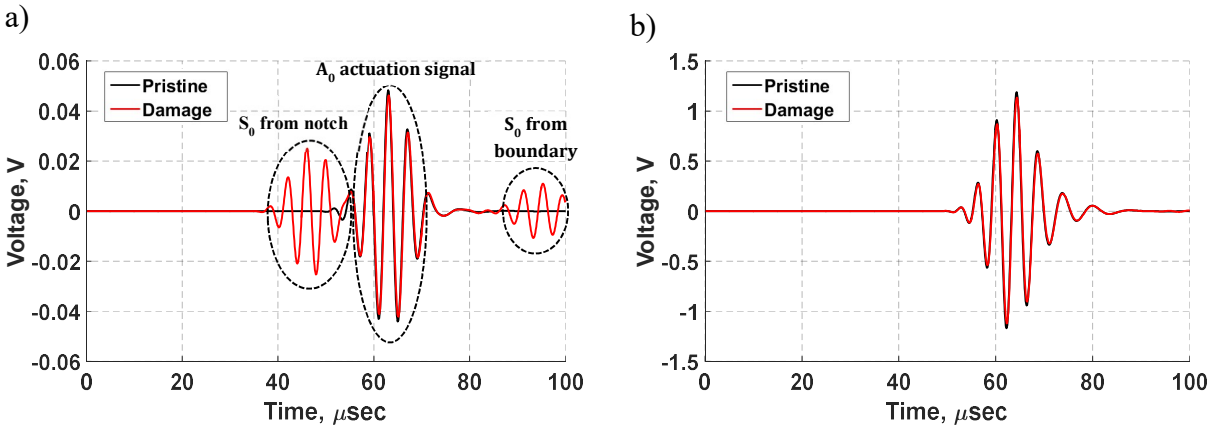

Figure 7.9: Sensor signals from pristine state (black) and damaged state (red) at 250 kHz from: a) d31 PZT sensor; b) d35 PZT sensor.

The time-frequency spectrum for damaged state in Figure 7.10a shows that all wave packets had about the same center frequency. The results of d35 PZT sensor in Figure 7.9b and Figure 7.10b shows a complete absence of the symmetric modes in voltage signals and in the time-frequency spectrum. This observation suggests that d35 PZT sensors have strong selectivity to sense antisymmetric waves while rejecting symmetric waves. The d35 PZT sensors are mainly sensitive to in-plane shear stress that are found to be negligible on the surface of the structure. As a result, the interaction between shear and the notch is expected to be small as shown in Figure 7.9b. The damage effect in the d35 signal is relatively small and manifested in the form of phase shift and magnitude reduction. On the contrary, normal displacements are found to be significant on the surface of the structure. This makes surface-mounted d31 (and d33) PZT sensors sensitive to any distortion in the profile of normal displacements indicating the location of

d31 sensor on the surface very effective. Based on this observation, joint defects are also expected to interact with stronger in-plane shear in the bondline yielding more accurate information about the integrity of bondline than surface mounted PZTs.

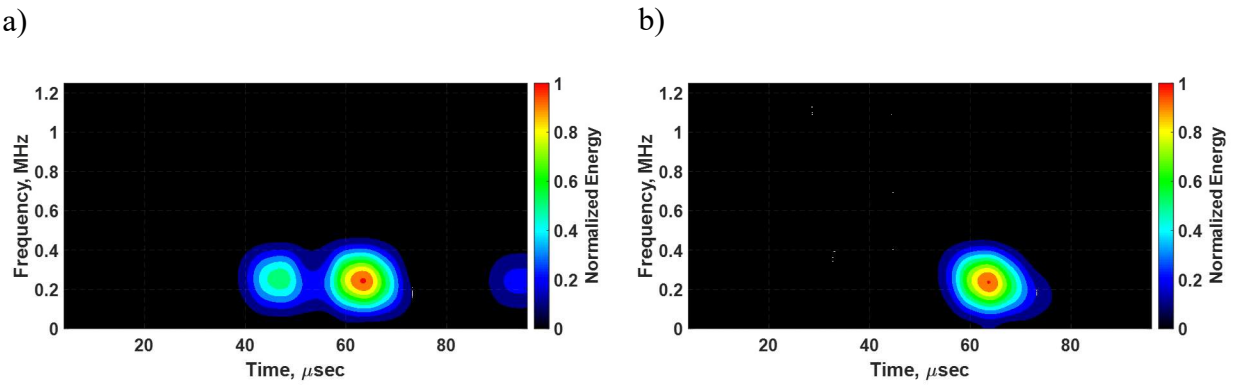

Figure 7.10: Time-frequency spectrums of voltage signals obtained at 250 kHz from a) d31 PZT sensor and b) d35 PZT sensor.

In summary, the results suggest that d35 PZT sensors offer a valuable merit by largely capturing antisymmetric wave modes in the media. Multimodal superposed waves of differing modes can coexist in the plate resulting in complex patterns that make interpreting the data to characterize defects a challenging task [16,59]. The selectivity of d35 sensors give them a useful advantage in signal processing because it makes the interpretation of the data more efficient and the outcomes more reliable. This advantage also enables a simple comparison between reflected and transmitted waves from pristine state and damaged state. Filtering symmetric modes in received signals significantly reduced the complexity of signal processing and this could potentially enhance the process of SHM as well.

7.3. Summary and Conclusions

A parametric study was performed where the thickness and length of d35 PZT transducers were varied while monitoring the actuation strength and the sensed voltage signal. The size of bondline-embedded d35 PZT transducers was found to have a significant influence on the actuation strength and the sensing ability of d35 PZT transducers. It was found that thicker and shorter d35 PZT sensors can produce stronger signals compared to thinner and longer d35 PZT sensors.

On the contrary, d35 PZT actuators were noticed to exhibit the opposite response to d35 PZT sensors with more complex behavior when thickness and length were varied. This demonstrated that the design of d35 PZT sensors and actuators to be embedded within a bondline for ultrasonic inspection favor differing geometries. This created an optimization challenge if a given transducer is intended to function as both an actuator and a sensor generating strong actuation without compromising sensing ability. Therefore, finding the optimum pair of d35 PZT transducers can maximize signal to noise ratio and the wave propagation distances which are essential in building a robust structural health monitoring system.

The selectivity of d35 PZT sensors was also investigated in simulation by comparing voltage signals obtained from a bondline-embedded d35 PZT sensor and surface-mounted d31 PZT sensor. Mode conversion from wave interaction with a surface notch provided a collection of symmetric and antisymmetric waves in the laminate structure. It was found that d35 PZT sensors offer a selective hardware filter that primarily captures antisymmetric wave modes in the laminate structure while suppressing symmetric wave modes. It is known that complex superposition of wave modes often results in difficulties

in damage detection and signal analysis. The selectivity of d35 PZT sensors could be employed in signal processing to make the interpretation of the data more efficient, reducing uncertainty and leading to more reliable analysis outcomes.

Chapter 8
Detection of Joint Defects in Laminate Structures

This chapter investigates the effectiveness of flexural waves to detect joint defects in laminate structures using bondline-embedded d35 PZT transducers in the bondlines. Finite element (FE) method was used to simulate multilayered structures with various defects including void, crack, and disbond in order to study the influence of damage on the propagation of flexural waves in bondlines. The sensitivity of flexural waves to damage is then quantified through the calculation of damage index for each damage case. The relation between flexural wave sensitivity to damage and actuation frequency is considered next. An experimental specimen with void was also considered to validate FE simulations. This chapter concludes with summary of the main findings.

8.1. Introducing Damage in Bondlines

In Figure 8.1, the modeling procedure of 3D multiphysics analysis discussed in section 5.3 was followed here to simulate laminate structures with various joint defects. The material properties of the multilayered structure and the bondline-embedded piezoelectric transducers are given in Table 1 of the Appendix. Three damage cases including void, vertical crack, and disbond introduced in the bondline were considered to study the influence of damage on antisymmetric waves generated by d35 PZT actuators. The amount of interaction between the propagating waves and the inflicted damage was quantified using a damage index based on root mean square deviation method. More details on the modeling for each damage type is discussed in the next section.

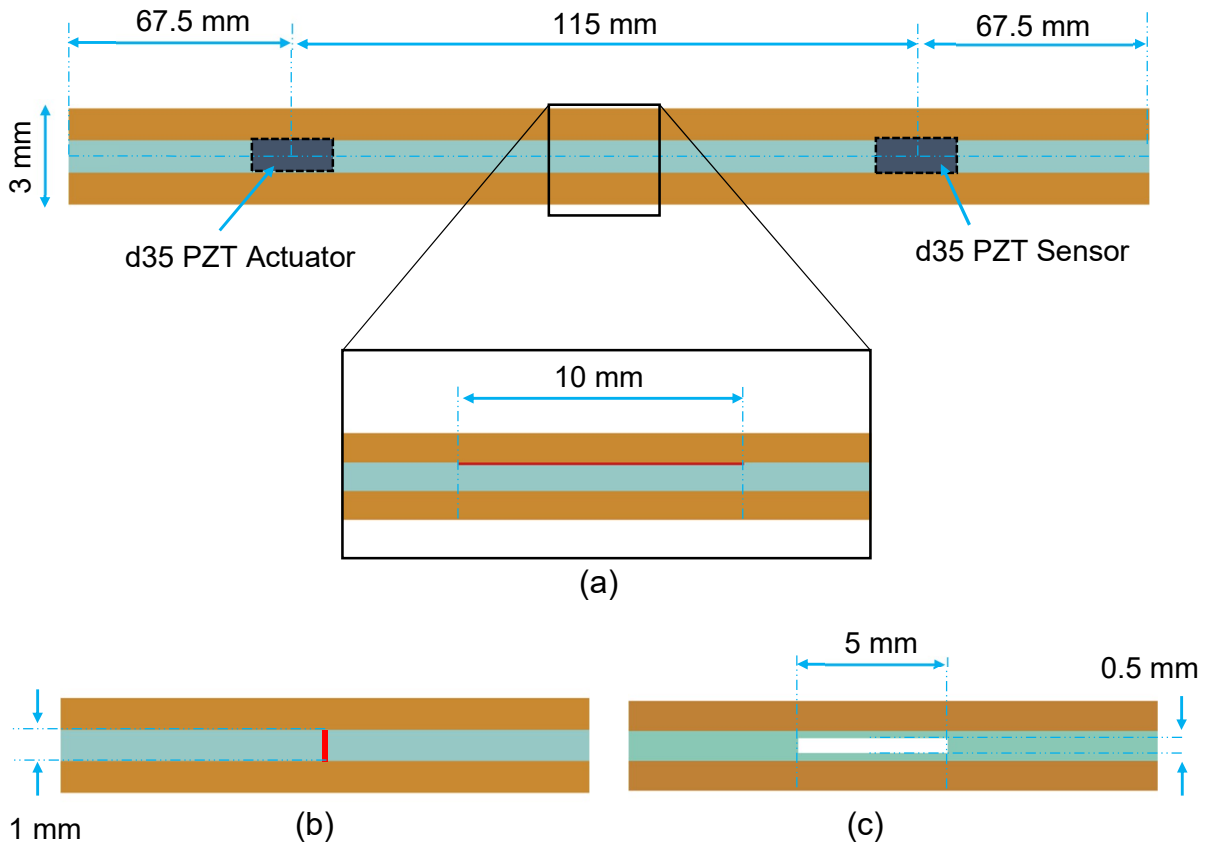

Figure 8.1: 2D model of a multilayered structure with a damage located at an equal distance from d35 PZTs: a) disbond, b) vertical crack, and c) center void.

8.1.1. Damage modeling

In Figure 8.1, the structure was modeled with no damage to obtain a baseline signal for comparison with damaged state. The modeling procedure of the three damage cases are discussed in this section with some details. In conventional ultrasonic testing, disbonds often produce very low ultrasonic contrast meaning low reflection and high transmission resulted from close contact between the adjacent parts even though they have little or no bond strength [21].

To simulate a disbond in the adhesive joint, a group of contact elements highlighted in Figure 8.1a was defined to allow joint separation via setting unilateral contact option

on. The disbond at the interface region is 10 mm long located at 50 mm from the transducers. Because a gap can form and the contact area at the interface disbond may change as the waves propagate through the media, that renders the problem to be nonlinear.

Mode-I crack (opening crack) was also considered in this study through the application of infinite friction on a group of contact elements in the bondline creating a vertical crack with rough contact. Due to infinite friction coefficient, there is no sliding among the adjacent elements. The crack was made through the thickness of the adhesive layer as shown in Figure 8.1b.

A common damage in adhesive joints is a void. In Figure 8.1c, a group of structural elements located at 50 mm from the transducers were removed introducing a 0.5 mm x 5 mm void at the center of the bondline.

8.1.2. Damage index

A damage index was calculated for each damage case to quantify the distortion in received signals due to the presence of damage using Eq.(8.1). The damage index used for this analysis is based on the root mean square deviation (RMSD) method [39] and can be expressed as

$$DI_{dam} = \sqrt{\sum_{i=1}^{N} \left(X_i - x_i \right)^2 \Big/ \sum_{i=1}^{N} X_i^{\,2}} \tag{8.1}$$

In Eq.(8.1), X_i is the pristine state at the i^{th} measurement point, x_i is the damaged state at the i^{th} measurement point. The results from the FE models discussed herein are presented in the next section.

8.2. Results

In all damage cases, the actuation signal was kept the same throughout the analysis for comparison study. In Figure 8.1, the 5-peak tone burst signal was emitted from the d35 PZT actuator. The waveform signal obtained from the laminate structure with no damage being introduced in the bondline was used as a baseline signal (pristine signal) and plotted as pristine state in Figure 8.2. Similarly, the signal from a damaged state was denoted as damaged signal in the waveform plots. The scatter signal which was determined by calculating the difference between the pristine signal and the damaged signal was also displayed in Figure 8.2.

To quantify the sensitivity of flexural waves to joint defects, three parameters including damage index, signal attenuation, and phase shift were calculated for each damage case by considering the first wave packet in the pristine and damaged signals. Reflections were disregarded in the analyses because they are often complex superposed waves yielding higher uncertainties in the analysis of damage characteristics. Results summary of each damage case is provided in Table 8-1.

The normal displacements and in-plane stresses of flexural waves were also calculated for a set of nodes along the thickness located at 100 mm from the left boundary to capture the effect of damage on the propagating wave mode while also avoiding local damage defects on the response. Distributions of flexural waves for pristine state and damaged states are plotted in Figure 8.3. The shaded region in Figure 8.3 represents the position of the adhesive layer with respect to the upper and lower substrates. When flexural waves propagate through a defect, it may cause wave scattering, mode conversion, phase shift, and attenuation yielding distortion in received waveform signals.

The amount of distortion from such a defect depends on several factors such damage type, location, size, shape, and characteristics of actuation signal including frequency and modulation method.

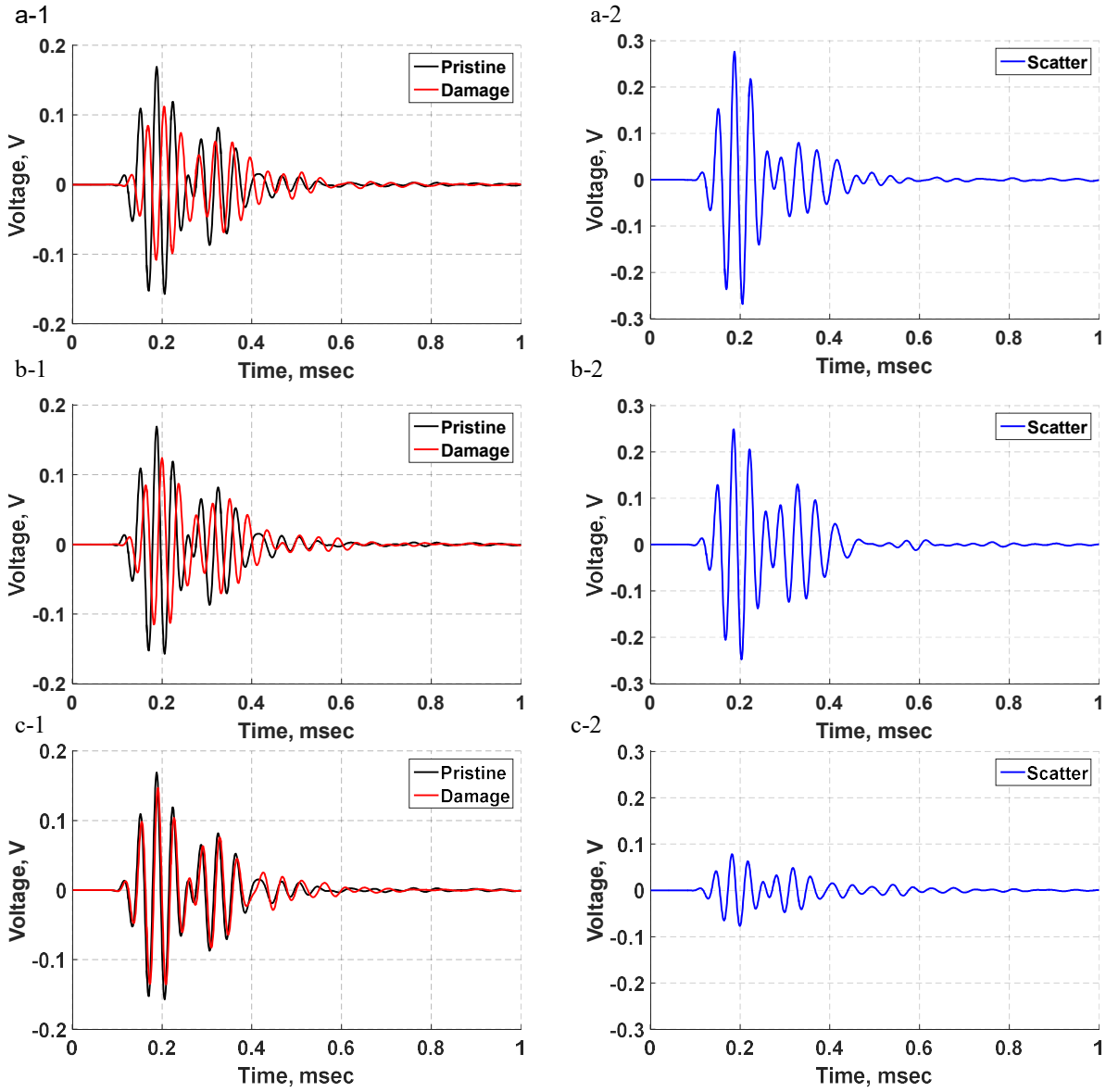

Figure 8.2: Comparison of signals (right) between pristine state and damaged state, and scattered signals (Left): a) disbond, b) vertical crack, and c) void.

Table 8-1: Results summary for each damage state of laminate structure.

Joint Defect	Damage Index	Signal Attenuation	Phase Shift
Disbond	1.647	33.66%	154.6°
Crack	1.500	26.75%	113.4°
Void	0.468	13.11%	20.6°

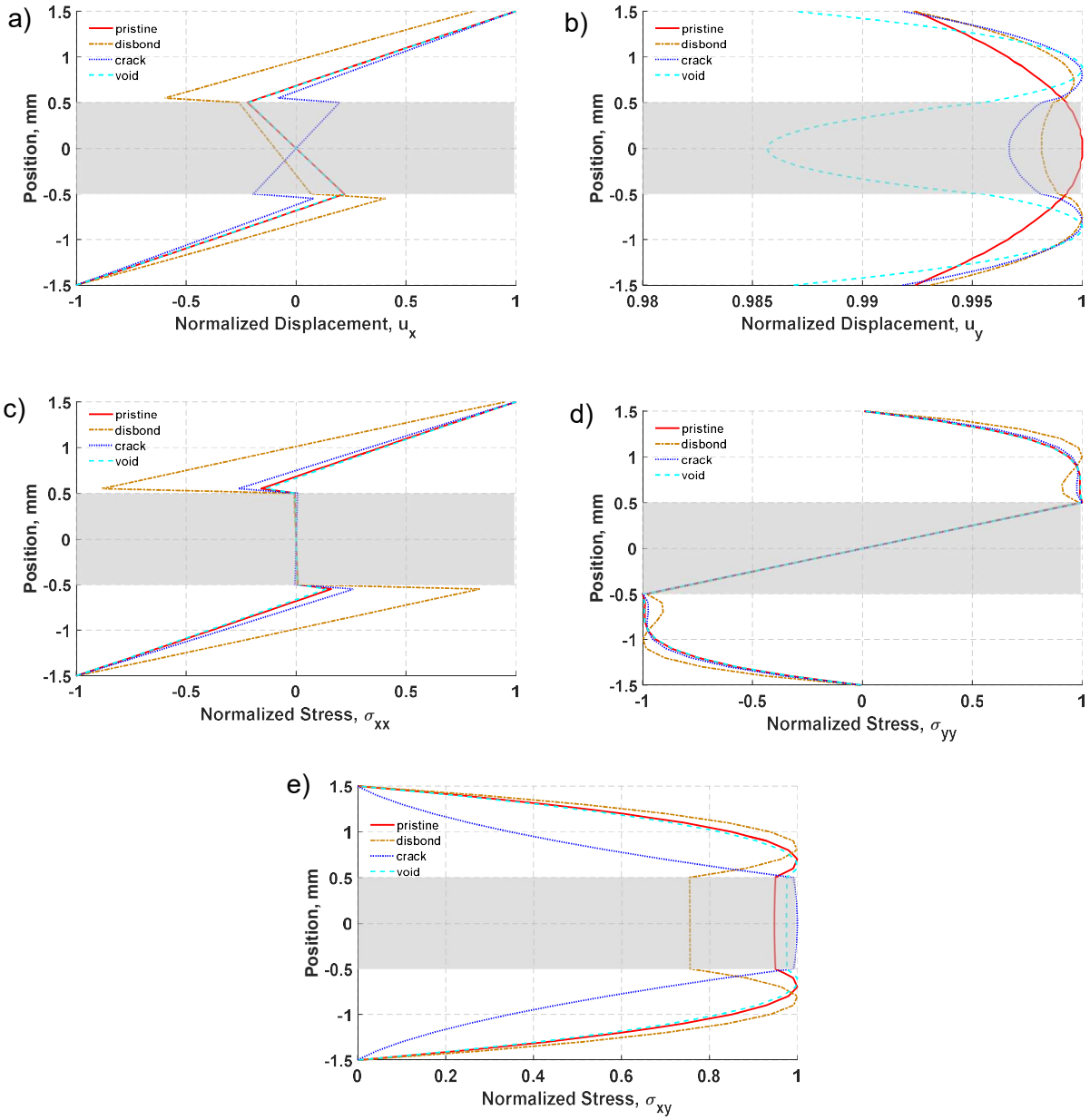

Figure 8.3: Comparison of through-thickness displacements and in-plane stresses of flexural waves at 30 kHz for four states: pristine, disbond, crack, and void.

A common trend can be observed from the results in Figure 8.2 that flexural waves are sensitive to all investigated types of joint defects discussed herein but at various levels. In Figure 8.2a, it can be noted that flexural waves exhibit high sensitivity to disbond causing significant phase shift and attenuation in the received signal resulting in high magnitude scattered signal. The waveform signal obtained from the laminate structure with disbond has a phase shift of 154.6^{o} and attenuation of about 33% of the pristine signal. The damage index which lumps the effects of damage on flexural waves was calculated 1.647 showing a strong interaction between the flexural waves and disbond. By inspecting the distributions of flexural waves in Figure 8.3, disbond in the bondline of the laminate structure disrupted the antisymmetric profile of axial displacement resulting in nonlinear effects in the normal axial stress especially near the interface region.

Because flexural waves are governed by axial particle motion in the direction of wave propagation, the lateral displacement shows negligible effect with little distortion in the normal lateral stress. The distribution of in-plane shear stress indicates disbond caused shear stress reduction of 10% in the adhesive layer counterbalanced with increase in the substrates. This high sensitivity can be attributed due to the nonlinear effect of disbond resulted from the nonlinear friction between the crack surfaces. The two surfaces of the disbond interact with each other repeatedly in axial motion when the flexural waves transmit through the disbond. The amount of interaction between the two sides of disbond can dictate the amount of distortion in the propagating flexural waves. The results suggest that flexural waves are effective in detecting this type of defect.

The waveform signal obtained from laminate structure with vertical crack was noticeably attenuated and delayed as can be seen in Figure 8.2b. The mechanism

responsible for noticeable distortion in the signal is the intermittent opening and closing of the crack surfaces varying in the contact length during the propagation of flexural waves. This phenomenon is often referred to as breathing crack. The two surfaces of the crack close when the compression part of the signal transmits through the crack and open during the transmission of the tensile part. As a result, the velocity of flexural waves changes while transmitting through the crack due to variation in the contact stiffness between the crack surfaces. The damage index was determined 1.5 with signal attenuation of 26.75% and phase shift of 113.4°. The nonlinear effect of the contact stiffness due to intermittent opening and closing of crack surfaces yields unique characteristics manifested in the distributions of flexural waves.

In Figure 8.3, the axial distribution shows vertical crack caused a profile inversion of flexural waves along the thickness and noticeable distortion near the interface regions. Similarly, it caused a significant reduction in shear stress along the thickness of the aluminum substrates whereas the adhesive layer received the maximum shear stress. On the other hand, the distributions of lateral displacement and normal stresses show little effect of vertical crack on the propagation of flexural waves. One common behavior between disbond and vertical crack which has contributed to their high damage index is the nonlinear interaction of flexural waves with these defects yielding nonlinear effects and varying compatibility conditions at the interface that can be used as mean for damage detection.

Despite the fact void damage appears severe in the laminate plate, the flexural waves show less sensitivity to the presence of voids compared to other considered defects. It can be seen in Figure 8.2c that the received signal from laminate structure was attenuated

and slightly shifted due the presence of center void. The damage index of void is 0.468. The attenuation and the phase shift in the received signal are 13.11% and 20.5^{o}, respectively. As can be also observed from Figure 8.2c, the signal attenuation has most of the contribution to the damage index value while the phase shift considered comparatively small.

Furthermore, this is reflected on the distributions of axial displacement and normal stresses in Figure 8.3 showing no difference between pristine state and void state. On the other hand, the center void in bondline caused the maximum distortion among joint defects in the later displacement profile, but that distortion is not significant either because the difference between the extreme values is very small. Furthermore, the lateral displacement of flexural waves is expected to have little influence on d35 PZT sensor especially when the waves has a long wavelength such as 39 mm in this case. Also, d35 PZT sensors fundamentally are not capable of sensing in-plane symmetric axial displacement.

On the other hand, the distribution of in-plane shear stresses in Figure 8.3 indicates the presence of void increased the magnitude of shear stress along the adhesive layer while the aluminum substrates experienced the opposite effect. Because flexural waves exhibit flexural particle motion with minimal displacement (zero) at the neutral axis, placing void off center is not expected to significantly improve the sensitivity because the interaction of flexural waves with voids is constrained by the wavelength of the actuation signal. Smaller sensitivity to void can be attributed to the long wavelength (39 mm) resulting in weak interaction between the flexural waves and the 5 mm-void. Actuation signal with shorter wavelength is expected to enhance the interaction between flexural

waves and defects with linear effects such as voids and notches while longer wavelength is more effective for defects with nonlinear effects such as disbonds and cracks [60].

Among all distributions, the in-plane shear stress consistently shows noticeable distortion for all joint defects considered herein supporting the suitability of using d35 PZT transducers for detection of joint defects. Joint defects with nonlinear effects such as disbond and vertical crack resulted in complex profile of flexural waves in the adhesive layer and near the interface regions making the location of d35 PZT sensors in the bondline to capture these effects very effective. A d35 PZT sensor is fundamentally efficient in sensing in-plane shear waves because these waves align with its natural vibration modes. Any disturbances in the antisymmetric profile of in-plane shear waves is expected to yield distortion in the sensed signal.

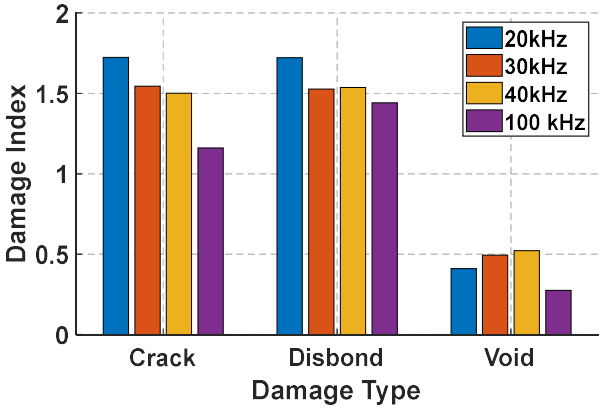

Figure 8.4: Damage index for void, vertical crack and disbond at different actuation frequencies.

Another important parameter to damage sensitivity is the characteristics of actuation signal including number of counts, frequency, windowing method, etc. To investigate the relation between the actuation frequency and damage sensitivity, the 5-peak actuation signal was used in the simulation along with four different center frequencies: 20 kHz, 30

kHz, 40 kHz, and 100 kHz. This analysis was conducted for all four damage cases. The damage index for the selected actuation frequencies are displayed in Figure 8.4. It is obvious that type of damage and actuation frequency are strongly related to the value of damage index.

Similar findings were reported by Kundu et al [20] in which they found the first antisymmetric mode was the only Lamb mode that can sense the presence of weak bonds. Also, it was noted the A0 mode was only sensitive when the phase velocity was less than a certain value. The phase velocity dispersion curve of a multilayered structure can reveal the relation between the actuation frequency and phase velocity and that can further verify this finding [1].

Additionally, it can be observed from Figure 8.4 the actuation frequency is inversely proportional to the sensitivity of flexural waves towards damage with the exception for the center void. The response of disbond and vertical crack to flexural waves is quite the same. The void however tends to show different behavior compared with other damage cases, but this behavior is also expected to vary according to its location, size and shape

8.3. Void Specimen

According to the results discussed in Section 8.2, voids were found the most challenging to detect using low frequency flexural waves. Therefore, an experimental specimen with void for damage detection analysis. This specimen was proposed to be utilized for a pristine state and damaged state because it has been shown in the literature that creating two identical specimens is a challenge due to variation in manufacturing and material properties [61]. Thus, before adhering the aluminum substrates together, two

PTFE (Teflon) wedges were puffed with graphite powder to weaken the bond between the wedges and the adhesive. They were implanted at the middle of the adhesive joint at an equal distance from the d35 PZT transducers to create artificial void through the width of the laminate specimen. The PTFE wedges are 55 mm x 5 mm x 0.762 mm. The shape of wedges found the optimum to reduce the friction (shear force) to break the joint bond as well as to increase the grip area while minimizing the chance of ripping the wedges. The thickness of the adhesive layer was controlled by placing 1 mm thick spacers on the corners and applying pressure on the specimen while curing. The final assembly was cured at 66^{o}C for one hour. The thickness of the adhesive layer after curing was measured at approximately 1 ± 0.2 mm. A fully prepared sample is shown in Figure 8.5.

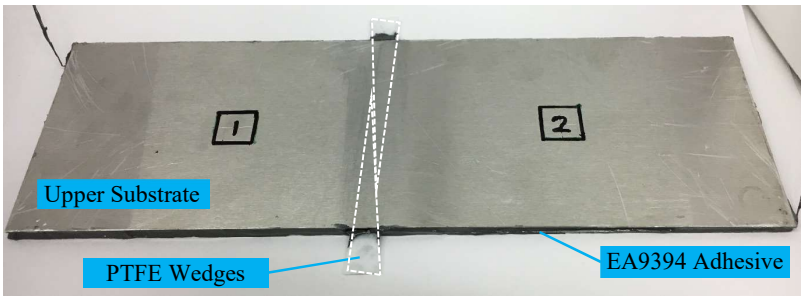

Figure 8.5: Fully prepared sample with PTFE wedges to simulate void in the bondline.

The laminate specimen with joint defect is shown under test in Figure 8.6. The actuating transducer, labeled as PZT-1 was actuated with the 5-peak tone burst signal at 30 kHz that is the same actuation signal used throughout this study for comparison purposes. The voltage signals received from the sensor were processed to de-noise the signals and produce the time-frequency response for pristine state and damaged state. The specimen with PTFE wedges was considered as a pristine state, and the damaged

state was introduced to the specimen by removing the wedges and actuating with the same signals used in the pristine state for damage identification analysis.

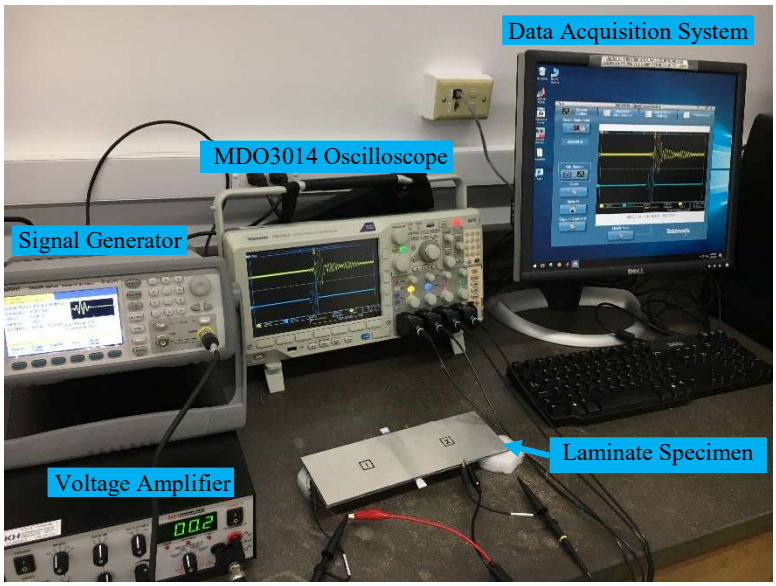

Figure 8.6: Experimental setup for testing a laminate specimen with a joint defect.

The waveform signal obtained from the specimen with PTFE wedges was used as a baseline signal (pristine signal) and plotted as pristine state in Figure 8.7a. Similarly, the signal from the specimen without the wedges was denoted as damaged signal in the waveform plots. The pristine and damaged waveform signals were plotted together in Figure 8.7a. The scatter signal which is the difference between the pristine signal and the damaged signal is also displayed in Figure 8.7b. It can be seen from sensed signals in Figure 8.7a, there are two main flexural wave packets which are the actuation wave packet and the reflection from the boundaries.

Damage index, signal attenuation, and phase shift were also calculated by considering the first wave packet in the pristine and damaged signals. It can be noted that the flexural waves exhibit noticeable sensitivity to a bondline void resulting in attenuation across the

damage signal with a value of 8.7% of the pristine signal. The phase shift was calculated small of about 11.57°. This finding was further verified in 2D FE multiphysics simulation of the laminate structure with center void in the bondline.

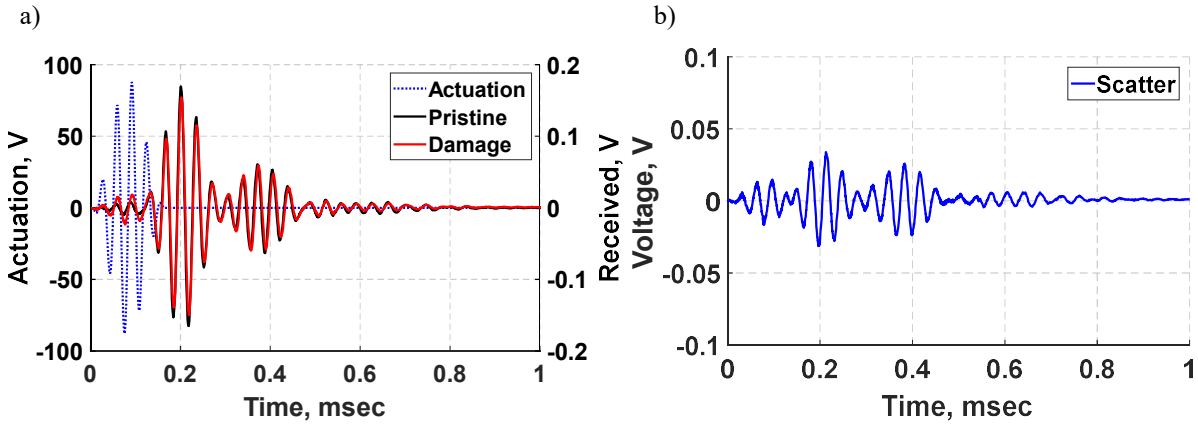

Figure 8.7: a) Comparison of experimental signals between pristine state and damaged state of laminate specimen with void excited at 30 kHz; b) scattered signal.

Comparing the effect of a void on the propagation of flexural waves from simulation and experiment shows that the presence of a void is primarily reflected in the received signals as magnitude attenuation. The void was found to mainly cause signal attenuation with little phase shift in the sensed signal. The magnitude of the scattered signal indicates the amount of distortion that void has inflicted on the flexural waves while propagating through it. The damage index for the signal obtained from the laminate specimen with void was calculated about 0.205 validating the effectiveness of flexural waves to detect void in the bondline of laminate structures.

8.4. Summary and Conclusions

Three damage cases including disbond, vertical crack, and void were introduced in the bondline of the laminate structure to investigate the effectiveness of flexural waves to detect joint defects using bondline-embedded d35 PZT transducers. Damage index

based on the root mean square deviation method was calculated to quantify the sensitivity of flexural waves to joint defects. A common trend was observed in the results that flexural waves were found sensitive to all investigated types of joint defects but at various levels. Flexural waves were observed to exhibit high sensitivity to disbond and vertical crack causing significant phase shift and attenuation in the received signal. This high sensitivity was attributed due to the nonlinear effect of these defects resulting from the change in the contact length during the propagation of flexural waves. The flexural waves were found to show less sensitivity to void compared to other considered defects.

Among all distributions of flexural waves, in-plane shear stress consistently showed noticeable distortion for all joint defects supporting the suitability of using d35 PZT sensors for detection of joint defects. It was also observed that joint defects with nonlinear effects such as disbond and vertical crack result in a complex profile of flexural waves in the adhesive layer and near the interface regions making the location of d35 PZT sensors in the bondline an optimal location to capture these effects with minimal loss of energy. By placing the transducers within the bondline, it provided a direct coupling between the bondline and the d35 PZT transducers and that has improved the transmission and sensitivity of flexural waves to joint defects.

A laminate specimen with void for damage detection analysis was tested. By comparing the effect of void on the propagation of flexural waves from simulation and experiment, it was noted that the presence of void has mainly caused attenuation in the received signals. The overall behavior of flexural waves obtained from FE simulation and experiment was comparable. The results presented in this chapter provide a fundamental work towards creating embedded, automated damage detection systems for adhesive

bondlines using flexural waves generated by d35 PZT piezoelectric transducers embedded within the bondline of laminate structures.

Chapter 9
Health Monitoring of Bondline Integrity

This chapter investigates the effectiveness of d35 piezoelectric transducers for health monitoring of bondline integrity using ultrasonic inspection. It begins with describing the fabrication process of a laminate specimen, and then three-point bending test that was used to create joint defects in the specimen. The chapter also discusses a flowchart of the ultrasonic health monitoring experiment that summarizes the methodology used herein. The sensitivity of flexural waves to joint defects was also investigated using two damage indices.

9.1. Ultrasonic Inspection

To evaluate the effectiveness of the proposed approach for ultrasonic inspection of joint defects, a laminate specimen was designed and fabricated with bondline-embedded d35 PZT piezoelectric transducers. A surface-mounted d31 PZT was also considered in this experiment for the purposes of comparison. A quasi-static three-point bending test was performed cyclically to create joint defects. The waveform signals obtained from bondline-embedded and surface-mounted sensors were analyzed to evaluate the sensitivity of flexural waves to combined joint defects. The EMI of d35 PZTs was continuously monitored during this experiment in order to ensure their pristine condition is maintained throughout the experiment.

9.1.1. Specimen design and fabrication

A schematic diagram of a laminate specimen is shown in Figure 9.1. The specimen consisted of two adhesively bonded aluminum sheets and two d35 PZT transducers

embedded inside the bondline. A surface-mounted d31 PZT sensor was also mounted on the surface of the specimen for purposes of comparison.

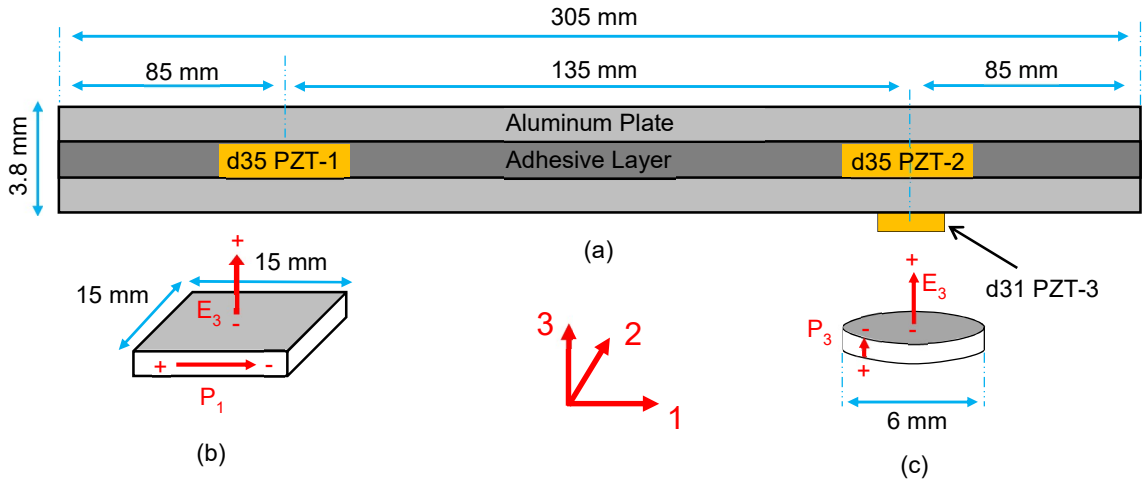

Figure 9.1: Laminate specimen with two d35 PZT transducers embedded in the bondline and d31 PZT sensor mounted on the bottom surface.

In this experiment, the aluminum sheets made of 6061-T6 aluminum material have geometric dimensions of 305 mm x 15 mm x 1 mm. The d35 PZT and d31 PZT transducers are made of APC 850 piezoceramic material (equivalent to Navy II). Material properties of the laminate specimen including shear-mode PZT transducers are given in Table 1 of the Appendix. The d35 PZT transducers which are 15 mm x 15 mm square plates with 1 mm thickness were adhered on the surface of one aluminum sheet using CW2400 conductive epoxy. This aluminum sheet also served as a common ground for the PZT transducers. The d35 PZTs were placed 135 mm apart and 85 mm from the left and right boundaries with their polarization direction aligned along the length of aluminum sheet. Thin wires attached to the hot terminals of the d35 PZTs using the same conductive epoxy. The aluminum sheets were then bonded together using Hysol EA 9394 nonconductive epoxy in order to protect the hot terminals from shorting against the ground terminal (the bottom aluminum sheet). The adhesive layer thickness was controlled by

placing 1.75 mm thick spacers and applying small uniform pressure on the specimen while curing. The adhesive thickness was measured at 1.8 ± 0.2 mm after curing. A round d31 PZT with 6 mm diameter and 0.25 mm thickness was then attached on the surface of the bottom aluminum sheet (ground terminal) using CW2400 conductive epoxy. The center of d31 PZT was set to coincide with the center of d35 PZT-2 making both transducers equidistant from d35 PZT-1.

9.1.2. Quasi-static three-point bending

A quasi-static three-point bending test was performed cyclically on the laminate specimen to investigate the capability of bondline-embedded d35 PZTs for health monitoring of laminate structures. The experimental setup, including the laminate specimen loaded in a three-point bending fixture with cylindrical rollers for the loading nose and supports, is shown in Figure 9.2. The specimen was tested in a pitch-catch configuration by actuating d35 PZT-1 and sensing with both PZT-2 and surface-mounted d31 PZT-3 sensors. The reversed path of actuation in which the waves propagate from d35 PZT-2 to d35 PZT-1 was also conducted for comparison analyses. In Figure 9.2, the transducers were connected to a Tektronix MDO3014 Domain Oscilloscope to collect voltage signals across the transducers at no-load condition. The d35 PZT actuator was excited with a 5-peak Hann windowed signal centered at 30 kHz using a KEYSIGHT 33500B Series waveform generator which also connected to a Krohn-Hite 7602M Wideband Amplifier to amplify the output actuation signal.

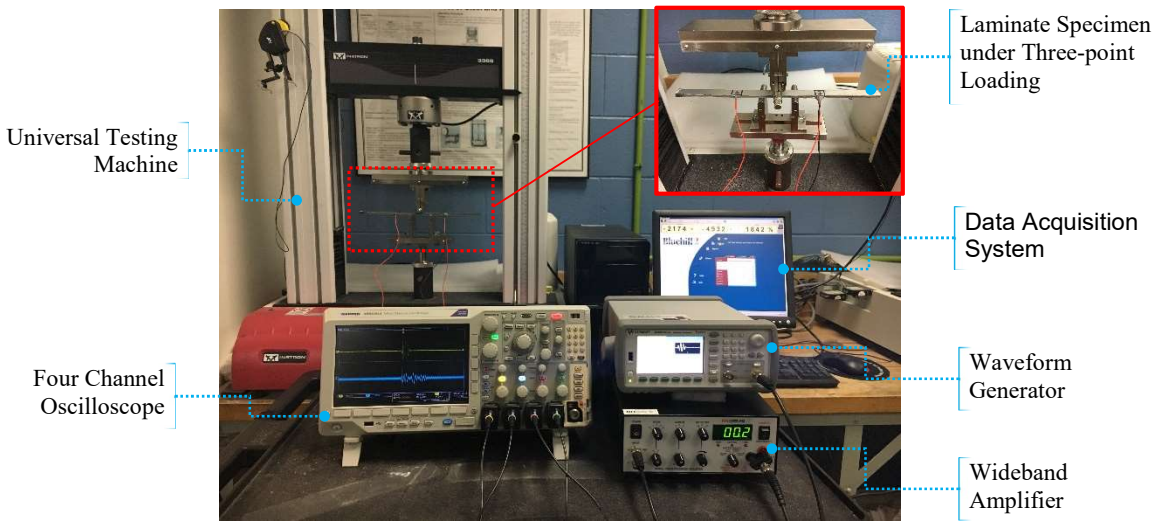

Figure 9.2: Experimental setup and magnified view of laminate specimen under three-point bending test.

A close-up view of the laminate specimen under three-point bending fixture is given in Figure 9.2 along with a schematic diagram shown in Figure 9.3. A quasi-static downward force was applied cyclically at mid-span to degrade the adhesive joint using a mechanical test machine (3369 Instron Universal Machine). The load was applied at a constant displacement rate of 1.35 mm/min (quasi-static). The displacement at mid-span was measured constantly throughout the experiment using the displacement transducer embedded in the mechanical test machine. After the load was quasi-statically applied and the mid-deflection reached a certain threshold, the load was gradually removed at the same rate. The test was then paused to obtain the electromechanical impedance response of d35 PZT transducers and to perform ultrasonic inspection. This cycle was repeated while incrementally increasing the mid-span deflection by 0.1 mm till 3.3 mm mid-span deflection was achieved. After each loading cycle, the specimen was then unloaded but was not removed from the fixture to maintain accurate and consistent displacement measurements throughout the experiment.

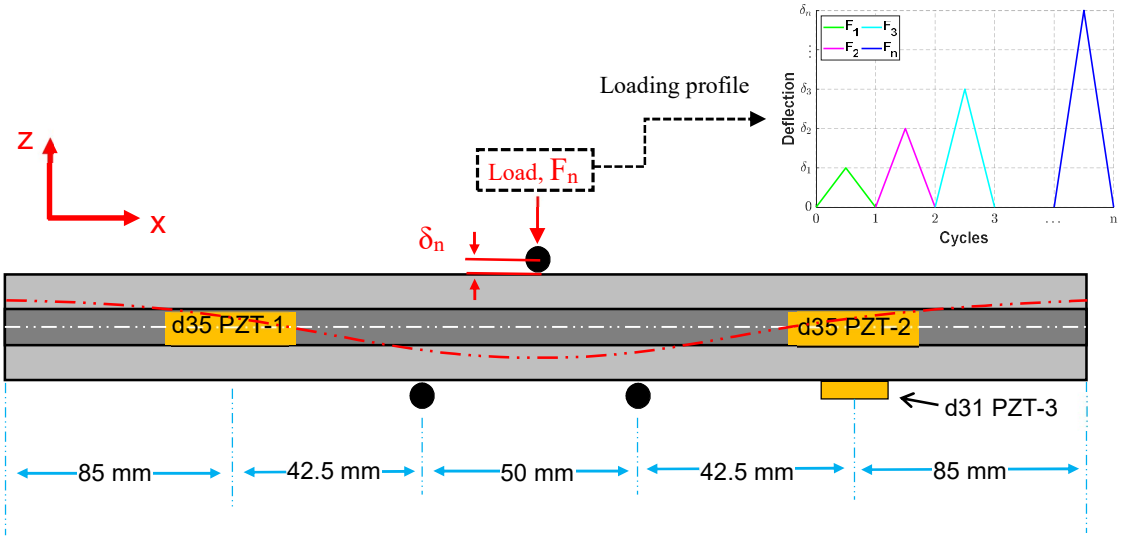

Figure 9.3: Laminate specimen under a quasi-static three-point bending force applied cyclically at mid-span.

As shown in Figure 9.3, the specimen was subjected to a quasi-static load at mid-span. The applied load was expected to induce bending stresses coupled to transverse shear stress in the laminate specimen. Thus, to maintain a pristine condition for the d35 PZTs and their surrounding bonding region during the test, the span between loading supports was set 50 mm and 42.5 mm distance from the PZT transducers. Flexural rigidity was used to define the failure state of the laminate specimen and consequently to set a threshold for terminating the test. The flexural rigidity of a beam under a three-point bending configuration similar to the laminate shown in Figure 9.3 is given as [62]

$$G_{fn} = \left(\frac{L^3}{48}\right)\left(\frac{F_n}{\delta_n}\right) \tag{9.1}$$

where: G_{fn} is the combined flexural rigidity of the laminate specimen at n^{th} loading cycle , L is the length between loading supports, F is the mid-span load at n^{th} loading cycle, and δ is the mid-span deflection at n^{th} loading cycle. The applied load to the specimen was defined by controlling mid-span deflection in order to avoid high crack propagation rate

and catastrophic failure of the specimen while increasing the damage severity. In this experiment, the deflection at the mid-span was increased to failure with increments of 0.1 mm while voltage measurements captured the PZT sensors at no-load condition.

9.1.3. Experiment flowchart

Figure 9.4 shows a flowchart of the ultrasonic health monitoring experiment that summarizes the methodology implemented herein to investigate the ability of d35 PZTs to monitor and assess bondline integrity. The experiment consists of three major tests which are performed sequentially starting with the application of three-point bending load followed by a sine-sweep for measuring the EM impedance of d35 PZTs and concluded with ultrasonic inspection in a pitch-catch orientation. The next cycle is then repeated with higher mid-span deflection, and the test continues until failure.

The health monitoring experiment was automated to sequentially perform all tests cyclically and the tests are succinctly described in the following steps:

1. Apply an increasing quasi-static load on the specimen until mid-span deflection reaches δ_n, then remove the applied mid-span load.
2. At no-load condition state, actuate d35 PZTs with a voltage frequency sweep (V_i) from 200 kHz to 1600 kHz by measuring the voltage (V_o) across a sensing resistor (R_s = 100 Ω) and the PZT element, then calculate the impedance ($Z = R_s \frac{V_i}{V_o}$).
3. Apply Fast Fourier Transform method and band-pass filter to the harmonic signals and identify the first EM frequency, f_1^{EM}, for each d35 PZT.
4. Continue the test if the difference between the baseline frequency and the measured frequency is less than α which is set 1% of the baseline frequency.

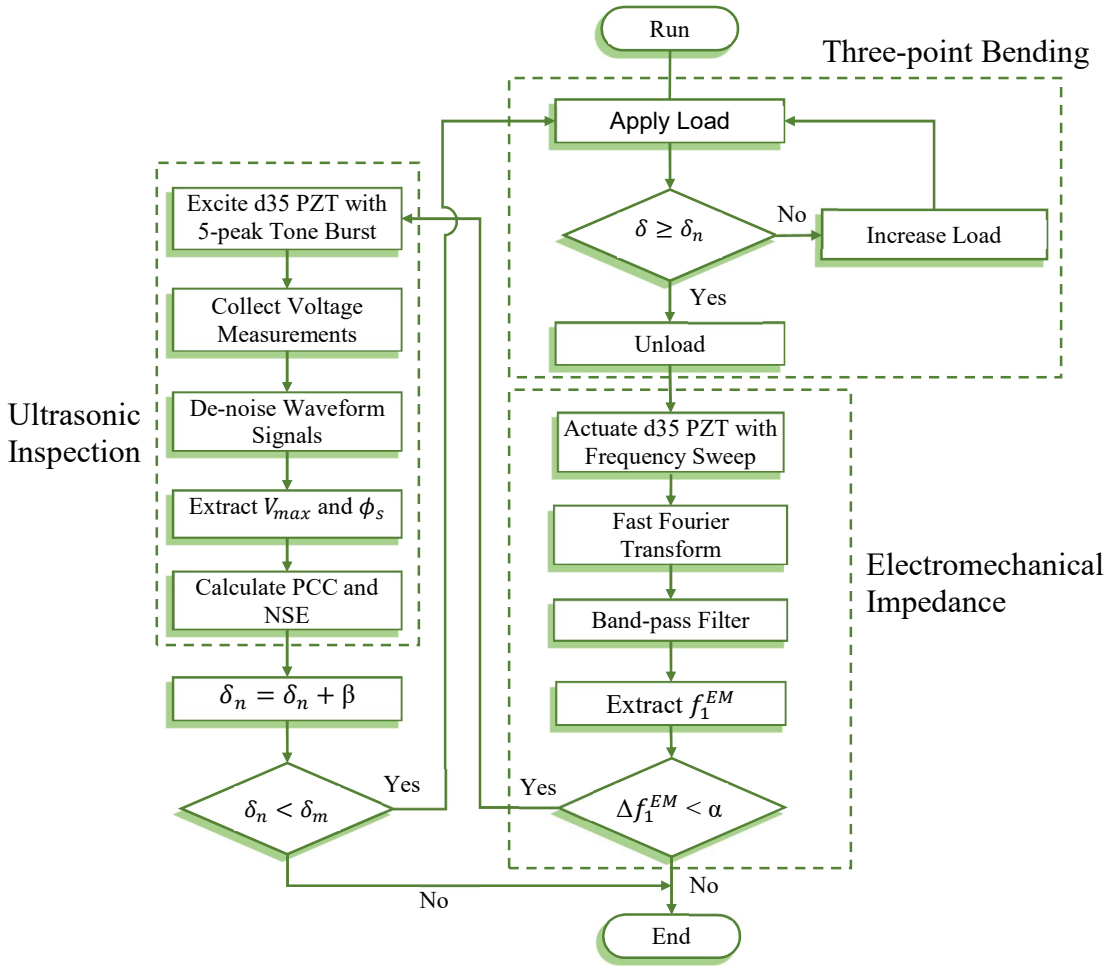

Figure 9.4: Flowchart of ultrasonic health monitoring experiment.

5. Perform ultrasonic inspection by actuating bondline-embedded d35 PZTs with a 5-peak signal centered at 30 kHz.
6. De-noise senor signals using Discrete Wavelet Transform with Coiflet wavelet performed at level 6 wavelet decomposition and applying the universal threshold $\sqrt{2\ln(.)}$, to the wavelet coefficients.
7. Determine the maximum voltage, V_{max} of the first arrival in sensor signals and the phase shift, ϕ_{max} with respect to baseline signals.
8. Calculate damage index values based on PCC and NSE methods using equations given in Table 2-1.

9. Repeat loading the specimen at a higher mid-span deflection by β increment, given 0.1 mm herein.
10. Stop the test when mid-span deflection reaches δ_{max} that is calculated based flexural rigidity of the laminate specimen.

For analysis of bondline integrity, the first wave packet was selected because later waves represent reflections that are often complex superposed waves yielding higher uncertainties in the outcomes. It should be mentioned that the width of the first wave packet was identified by assuming the width of the actuation signal is close to the width of the first arrival. Despite flexural waves being highly dispersive, the dispersion effects are expected to be relatively small given the short distance between the transducers.

9.2. Results and Discussion

9.2.1. Wave propagation analysis

Health monitoring of real-life systems such as structures often requires a cluster of baseline signals that represent normal operating conditions. To mitigate environmental effects, the experiment was performed at near constant conditions to perform health monitoring of the laminate specimen. The experiment was also performed at no-load condition to produce baseline signals that can be utilized for the analysis of damage detection in the subsequent sections. The first propagation path (PZT-1 → PZT-2) is dictated by exciting d35 PZT-1 and sensing via d35 PZT-2 as shown in Figure 9.1. The elastic waves generated by d35 PZT-1 are simultaneously sensed by d31 PZT-3 and this propagation path is labeled as (PZT-1 → PZT-3). The opposite propagation path (PZT-2

→ PZT-1) is also considered by actuating d35 PZT-2 and receiving signals via d35 PZT-1.

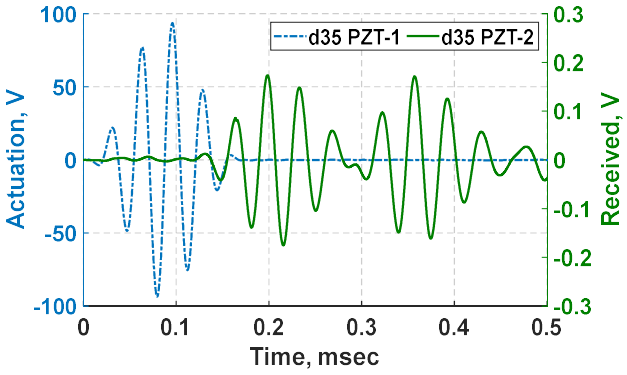

(a)

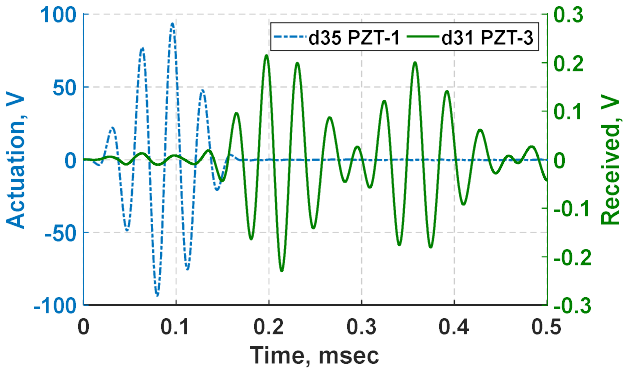

(b)

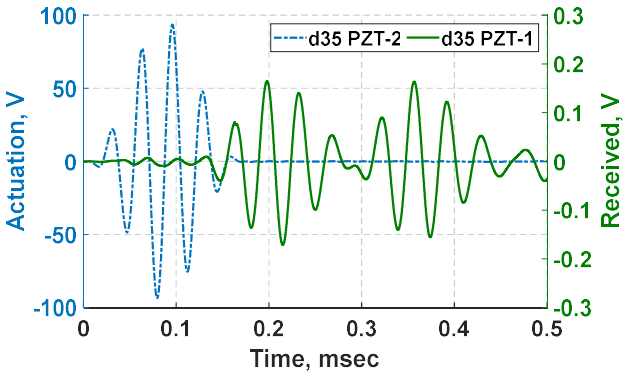

(c)

Figure 9.5: Waveform signals obtained for wave propagation paths: (a) PZT-1 → PZT-2; (b) PZT-1 → PZT-3; (c) PZT-2 → PZT-1.

In this experiment, a 5-peak Hann windowed voltage signal centered at 30 kHz was used to actuate bondline-embedded d35 PZT piezoelectric transducers and was kept the same throughout the pitch-catch ultrasonic inspection. The received signals by PZT sensors mounted on the surface and within the bondline of the laminate specimen were captured at a sampling rate of 10 MHz. The sensor signals are shown in Figure 9.5.

The bondline-embedded d35 PZT actuators are expected to generate antisymmetric (flexural) waves which are coupled with transverse shear strain. As can be observed from the received signals in Figure 9.5, there are two main wave packets. The first wave packet which travels the shortest distance to the sensor is the first arrival followed by its reflection. Signals from both d35 PZT and d31 PZT sensors appear to have similar response, but they were intrinsically generated with different dynamic mechanisms. The d35 PZT sensor signal was a result of shear strains induced by the flexural waves across the thickness. The shear strain however is negligible at the proximity of free surfaces.

On the contrary, the signal received by d31 PZT sensor primarily resulted from the normal strains carrying the energy of the flexural waves on the free surfaces. A 1% threshold of the maximum voltage was used to determine the ToF of the flexural waves. The ToF and group velocity were calculated for the waveform signals received by PZT sensors and are summarized in Table 9-1. The ToF of d35 PZT signal sensor shown in Figure 9.5a is 116.6 μsec with a group velocity of 1157.8 m/sec. The same propagating waves were also captured simultaneously by the surface-mounted d31 PZT sensor showing slightly slower signal with a ToF of 118.2 μsec. This indicates that the same wave mode being captured by both d35 PZT and d31 PZT sensors. The small difference

in ToFs captured by d35 PZT and d31 PZT sensors is attributed to different geometric and electromechanical properties among the sensors.

Table 9-1: Summary of wave propagation results at no-load condition.

Wave propagation path	Time of flight (μsec)	Group velocity (m/sec)
PZT-1 → PZT-2	116.6	1157.8
PZT-1 → PZT-3	118.1	1143.1
PZT-2 → PZT-1	116.4	1159.8

The reversed wave propagation (PZT-2 → PZT-1) for bondline-embedded d35 PZTs in Figure 9.5c shows the flexural waves have a ToF reaching the sensor at about 116.4 μsec which matches well ToFs obtained for other sensors. The variation in sensing mechanisms between surface mounted and bondline-embedded d35 PZT sensors further justifies the small difference in ToFs between d35 PZT and d31 PZT sensors.

9.2.2. Joint degradation

As previously mentioned, the laminate specimen was subject to a three-point bending to initiate and propagate joint defects in the bondline. The bending load applied at mid-span was controlled through known mid-span deflection of the laminate specimen. The load is expected to induce bending stresses across the thickness of the laminate with maximum normal stresses in the surface and maximum transverse shear stress at the neutral axis. A plot of the applied load versus deflection is shown in Figure 9.6. The downward mid-span deflection was increased from 0 to 3.3 mm in 0.1 mm increments. It can be noted from Figure 9.6 that the laminate specimen has an initial peak indicating flexural strength of about 1450 N at which a mixed-mode (flexural) crack developed and located 21 mm from the applied load. The mixed-mode crack was formed at about 45

degrees plane as result of the adhesive layer between loading supports being subjected to both normal and transverse shear stresses.

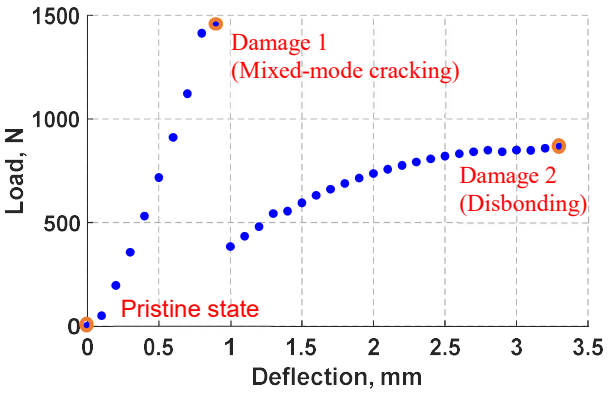

(a)

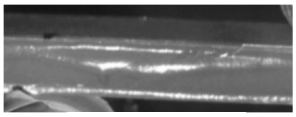

(b) Pristine state

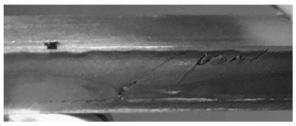

(c) Flexural cracking

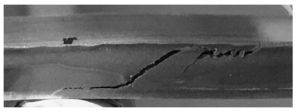

(d) Disbonding

Figure 9.6: (a) Load-deflection response at: (b) pristine state, (c) flexural cracking at 0.9 mm mid-span deflection, (d) disbonding at 3.3 mm mid-span deflection.

The purpose of this test is to degrade the adhesive joint beyond the mixed-mode crack, accumulating higher level of combined damage. For this reason, the test continued and past the initial peak, producing disbonds (slippage) among the laminate layers. While loading the specimen to the next cycle at 1 mm mid-deflection, a small disbond of about 5 mm was also observed along the bondlines. As can be noted from Figure 9.6c and d, the disbond initiated at the onsets of the mixed-mode crack and propagated further while increasing the mid-span deflection. In Figure 9.6a, the slope (F/δ) of load-deflection data which dictates the flexural rigidity of the specimen was calculated 2.6 N-m^2 via linear regression analysis in the deflection range between 0 – 0.9 mm. This has been followed by a significant drop in the flexural strength by more than 65%. By increasing mid-span deflection from 1 mm to 3.3 mm, its flexural rigidity significantly reduced and continuously decreased beyond 1 mm mid-deflection. Furthermore, flexural rigidity provides an

indication of damage severity, particularly disbonding among the laminate layers. The three-point bending test was stopped when flexural rigidity reached almost zero.

9.2.3. Electromechanical impedance

EMI method was used to inspect and ensure that no damage occurred to bondline-embedded d35 PZTs and their bonding regions during the three-point bending test. This analysis is of considerable importance, as the subsequent analyses involved the same PZT transducers for detection of joint defects.

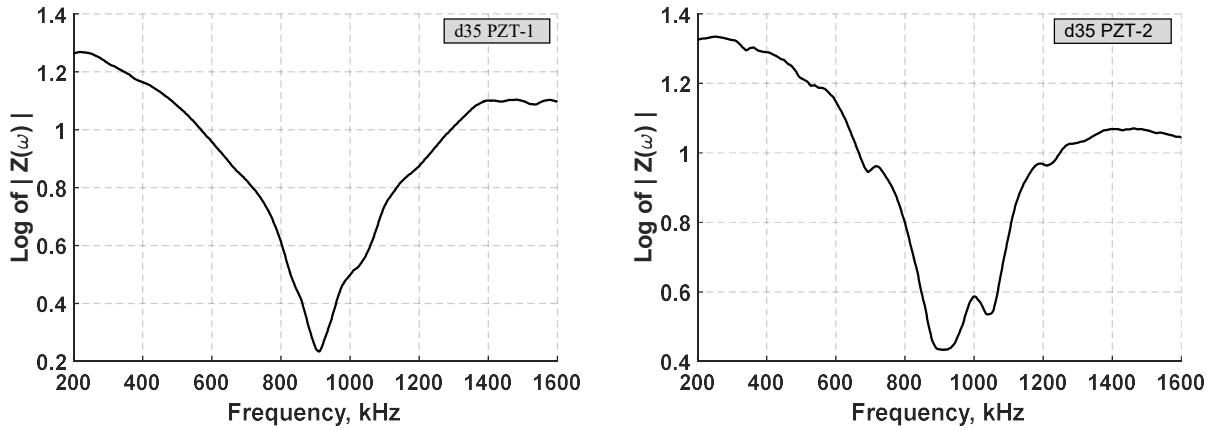

(a) (b)

Figure 9.7: EMI response of bondline-embedded d35 PZTs with a frequency range containing the first EM resonance for: (a) d35 PZT-1, (b) d35 PZT-2.

The EM impedance of bondline-embedded d35 PZT transducers were recorded after each individual cycle at no-load condition. By assuring pristine state for d35 PZTs, distortions in received signals can be mainly attributed to bondline integrity. Despite residual stresses that accompany plastic deformation in localized areas such as at the applied load or at the loading supports can modulate the propagating waves in the laminate, the distortion in received signals is expected to be relatively small when compared to the effects that may be caused by joint defects. In this analysis, the first EM

frequency was monitored, therefore each d35 PZT transducer was excited with a frequency sweep from 200 kHz to 1600 kHz. The impedance response from both transducers are shown in Figure 9.7. The first EM resonance was collected repeatedly after each loading cycle from bondline-embedded d35 PZTs throughout the experiment. The mean and standard deviation of the first EM resonance were calculated for d35 PZT-1 to be 912.8 kHz and 0.0194 kHz respectively. Likewise, d35 PZT-2 has a mean of 918.8 kHz and standard deviation of 0.114 kHz. The results indicate that the d35 PZTs have maintained a pristine state throughout the three-point bending test.

9.2.4. Ultrasonic inspection of joint defects

As shown in the flowchart in Figure 9.4, the EM impedance is followed by ultrasonic inspection in a pitch-catch scheme of actuating d35 PZT-1 with 5-peak signal centered at 30 kHz and sensing voltage signals simultaneously via surface-mounted d31 PZT-3 and bondline-embedded d35 PZT-2 sensors. The same actuation signal was then used to excite d35 PZT-2 and the propagating waves were picked up by d35 PZT-1. The sensed waveforms were first de-noised using Discrete Wavelet Transform with Coiflet mother wavelet performed at level 7 wavelet decomposition. After identifying the first wave packet, the maximum voltage and the phase shift with respect to baseline signals were determined for each individual cycle of mid-span deflection.

The waveform signals at 1 mm and 3.3 mm mid-span deflections were compared against the baseline signals for each corresponding PZT sensor and are given in Figure 9.8. The results show that the signals received at 1 mm mid-span deflection lead the baseline signals by about 60 degrees but associated with relatively small attenuation compared to baseline signals. At 3.3 mm mid-span deflection, an opposite behavior was

observed in which the recorded signals lag the baseline signals with about 80 degrees and with substantial attenuation in amplitudes.

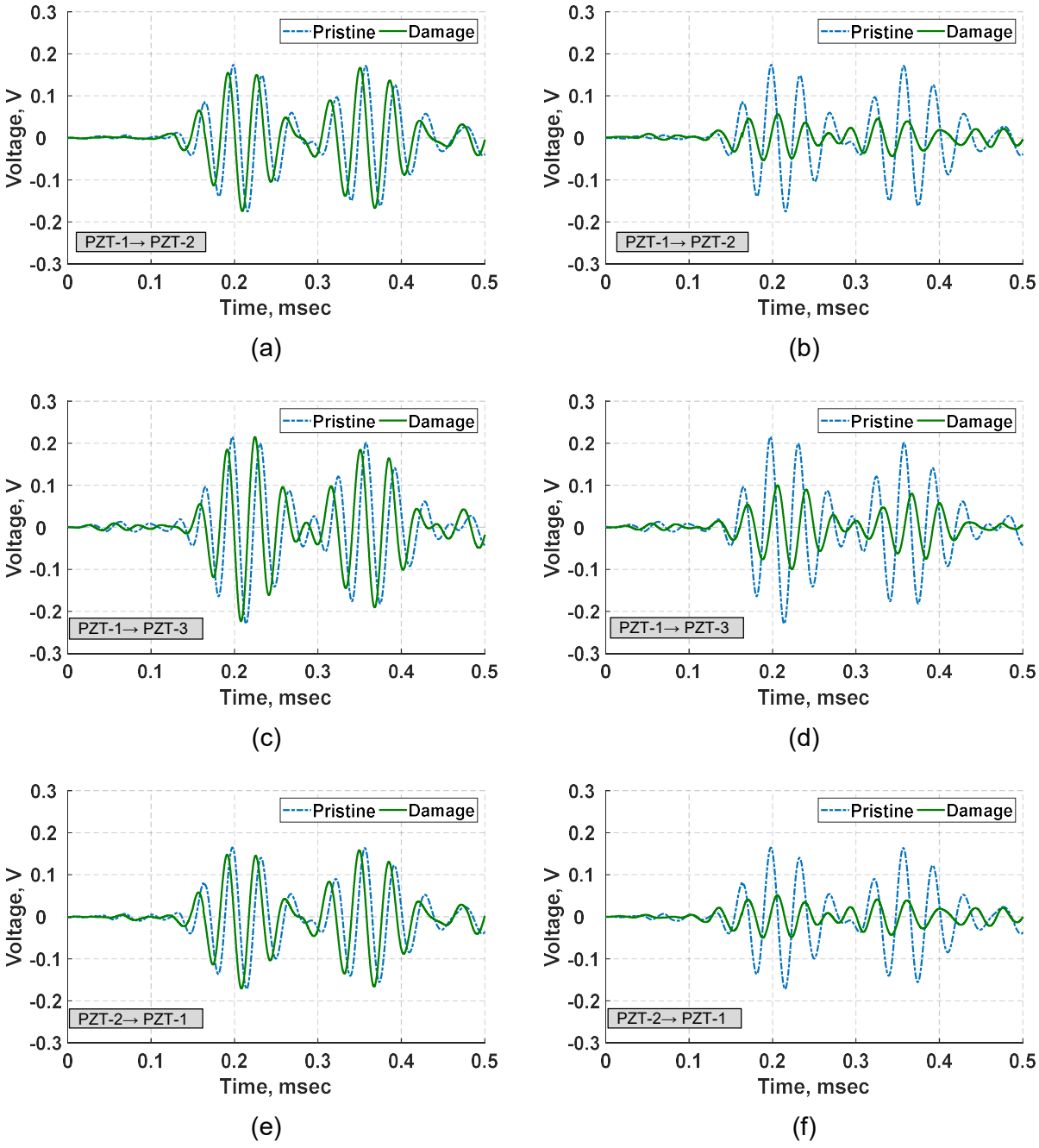

Figure 9.8: Comparison of waveforms collected at 1 mm deflection (left column) and 3.3 mm deflection (right column): (a) and (b) PZT-1 → PZT-2; (c) and (d) PZT-1 → PZT-3; (e) and (f) PZT-2 → PZT-1.

The flexural waves generated by bondline-embedded d35 PZT actuators traveled through the laminate specimen governed by maximum axial strain on the surface, mainly captured by the surface-mounted d31 PZT, and maximum shear strain at the neutral axis, sensed by bondline-embedded d35 PZTs. It can also be observed from the results in Figure 9.8 that the signals obtained from d35 PZT sensors show higher attenuation compared to the d31 PZT sensor signal. The d35 PZT signals show higher voltage reduction by about 10% compared to d31 PZT signals. This can be attributed to the optimal location advantage of d35 PZTs being internally embedded within the adhesive layer, resulting in direct coupling to the bondline.

Sensor waveform signals collected during the experiment were processed to determine the maximum voltage in the first arrival and the phase shift with respect to the reference signals. The results are shown in Figure 9.9. It can be seen from Figure 9.9a that the voltage amplitude displays little change until 2.3 mm deflection at which it shows a start of sharp decline in the amplitude reaching about 0.05 volt for d35 PZT-2 sensor. Over the mid-span deflection 0 – 3.3 mm, there is about 70% voltage reduction in the measured signals compared to the baseline signal. On the contrary, the phase shift in sensor signals (Figure 9.9b) indicates increasing trend until 0.9 mm (prior to the mixed-mode crack) and lagging baseline signals by about 50 degrees followed by an abrupt drop by 110 degrees, leading the baseline signals by 60 degrees. After 0.9 mm mid-span deflection, the sensed signals show an increasing trend crosses to the positive phase and extends past the initial peak and reaching 85 degrees at 3.3 mm deflection.

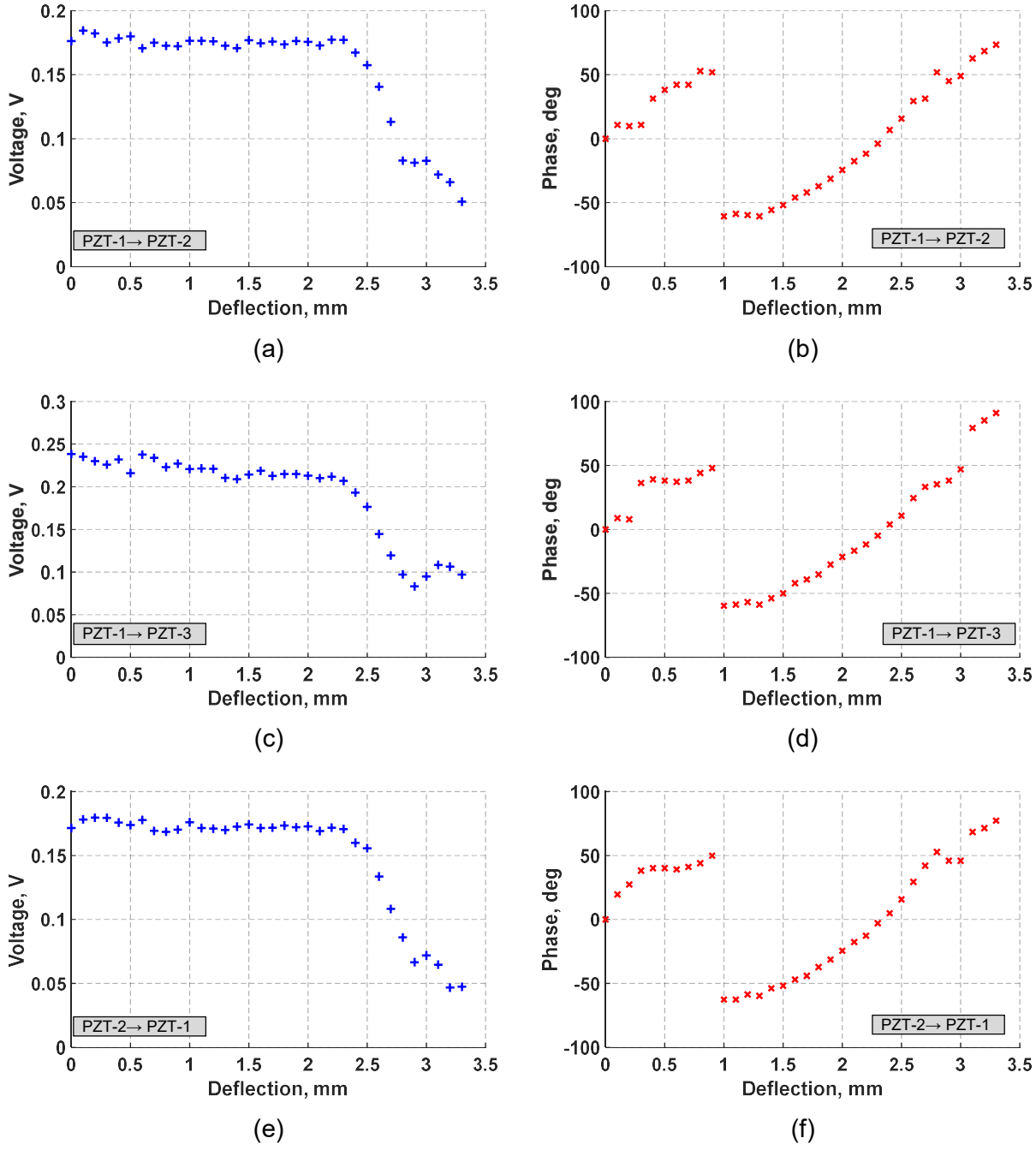

Figure 9.9: Maximum voltage amplitude (left column) and phase shift (right column) from waveforms: (a) and (b) PZT-1 → PZT-2; (c) and (d) PZT-1 → PZT-3; (e) and (f) PZT-2 → PZT-1.

Similar trends were also observed from the signals received by the surface-mounted d31 PZT sensor as shown in Figure 9.9c and d. It can be observed from the results that the phase shift in d31 PZT signals also show significant drop at 0.9 mm mid-span

deflection. The higher voltage amplitude generated by d31 PZT sensor compared to d35 PZT sensor was attributed to the variation in electromechanical properties as well as differing mechanisms of sensing elements and the forces acting on these sensing elements. As previously mentioned, the normal strains induced by the d35 PZT actuator are small in the adhesive joint and maximum at the free surface, where d31 PZT sensor was mounted. However, the shear strains are negligible at the surface and maximum at the neutral axis, where d35 PZT sensors were embedded. The surface-mounted d31 PZT sensor measured maximum normal stresses while d35 PZT sensors measured the maximum shear strain in the bondline. In Figure 9.9e and f, similar trends were observed in which the mixed-mode crack in the bondline resulted in significant effect on flexural waves transmitted through it with negligible voltage drop.

To evaluate bondline integrity, two damage index methods based on PCC and NSE were used to measure the difference between baseline signals and the measured signals over the first wave packet. It can be observed from the results in Figure 9.10 that PCC increases as the deflection increases until reaching initial peak at about 0.9 mm at which the mixed-mode crack was fully developed in the specimen. This was followed by a decreasing trend in the damage index value reaching a local low at 2.3 mm. That also followed by increasing trends reaching the maximum index value at 3.3 mm deflection. This behavior was observed from all embedded sensors in the specimen. The NSE damage index is less sensitive to phase shift in the signals and exhibits constantly decreasing trend from 0 – 2.3 mm deflection suggesting change in energy of the received signals is relatively small. This behavior reversed to an upward trend indicating significant drop in the signal energy reaching its maximum at 3.3 mm mid-span deflection. This

behavior can be observed from d35 PZT sensors as well as d31 PZT sensor with minor variation.

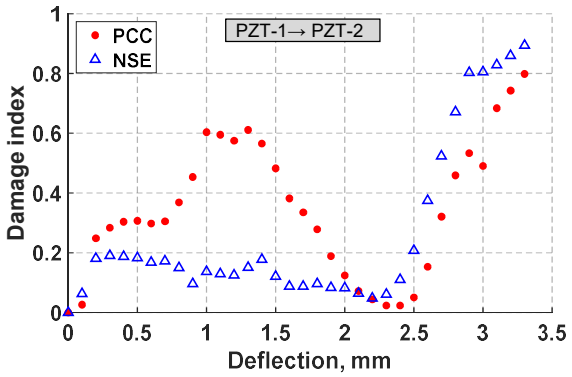

(a)

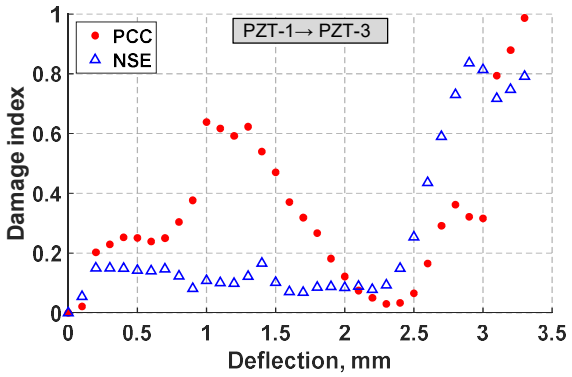

(b)

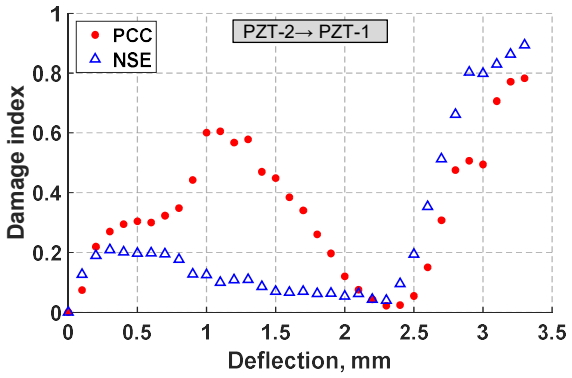

(c)

Figure 9.10: Damage index values based on PCC and NSE methods for signals received by: (a) d35 PZT-2; (b) d31 PZT-3; (c) d35 PZT-1.

The damage index values of PCC in Figure 9.10 reveals the interaction level of flexural waves with the damage. It can be noted from Figure 9.10, despite the increase in damage severity of the laminate specimen, the values of NSE and PCE shows decreasing behavior until loading cycle reached 2.3 mm. This trend could be due to the change in damage characteristics resulting in low interaction between the flexural waves and the bondline damage. Flexural waves tend to interact much less with linear defects such as voids than with nonlinear defects such as disbonds and cracks. The high sensitivity of flexural waves to nonlinear defects is often attributed to the change in the contact length of a defect during the propagation of waves [60,63,64]. Therefore, when the mixed-mode crack initiated over the mid-span deflection 0 – 0.9 mm, the crack has the characteristics of a nonlinear defect that has strong interaction with flexural waves. Thus, the PCC damage index from all sensors shows an increasing trend till the mix-mode crack fully developed at 0.9 mm mid-span deflection. The decreasing trend beyond 0.9 mm suggests the damage evolution was not favorable to flexural waves and reaching its maximum growth at 2.3 mm deflection.

Despite higher deflection has exacerbated the level of damage, both damage indices predicted low values suggesting flexural waves have minimal interaction with damage at 2.3 mm mid-span deflection. Over the deflection range 1 – 2.3 mm, the laminate specimen is expected to be accompanied by plastic deformation causing the mixed-mode crack to gradually develop into a large void such that the crack remained open at no-load conditions resulting in less interaction with flexural waves. Despite the presence of disbonds at early stage over 1 – 2.3 mm mid-span deflection range, it is expected the contribution of disbonds to voltage waveform distortion is minimal as the results suggest

that disbonds were either zero-volume disbonds (also known as kissing bonds) or were comparatively not long enough to interact with 36 mm wavelength flexural waves.

The damage index values from both NSE and PCC reveal a turning point at 2.3 mm with sharp upward trend until failure. It was noted that the flexural rigidity of the specimen constantly decreased while the disbond grew resulting in longer disbonds which were expected to be the main source for the noticeable distortion in the received waveform signals over the mid-span deflection range 2.3 – 3.3 mm. Despite plastic deformation could have some effects on the propagation signals but expected to be small. This finding agrees well with state-of-the-art ultrasonic wave interaction with defects supporting that elastic waves including flexural waves have higher sensitivity to nonlinear defects such as cracks and disbonds than linear defects such as voids [60,63–65].

By inspecting Figure 9.9 and Figure 9.10, it can be noted from the results that the PCC damage index is more sensitive to phase shift while the NSE damage index is more sensitive to amplitude of voltage waveform signals. Despite the existence of a combined defect in the bondline, the amount of distortion inflicted on the propagating flexural waves is determined by the dominant type of defect. In this study, the defect type has not been controlled thus multiple joint defects were present simultaneously. That also imposed a challenge to correlate change in waveform signals with a certain type of defect. The presence of different types of defects also imposes high uncertainty on identifying the type of damage by solely using damage index which represents a lump sum of damage effects on propagating waves. In real life structures, however, damage is often composed of two or more types of defects, making the proposed methodology appropriate for this study.

9.2.5. Influence of preload condition

In this analysis, actuation of bondline-embedded d35 PZTs and the sensing of elastic waves in the laminate specimen has occurred at a preload condition such that the mid-span load was not fully removed during ultrasonic inspection. An application of a small load on the specimen is expected to alter the characteristics of the combined defects and consequently the propagation of ultrasonic waves.

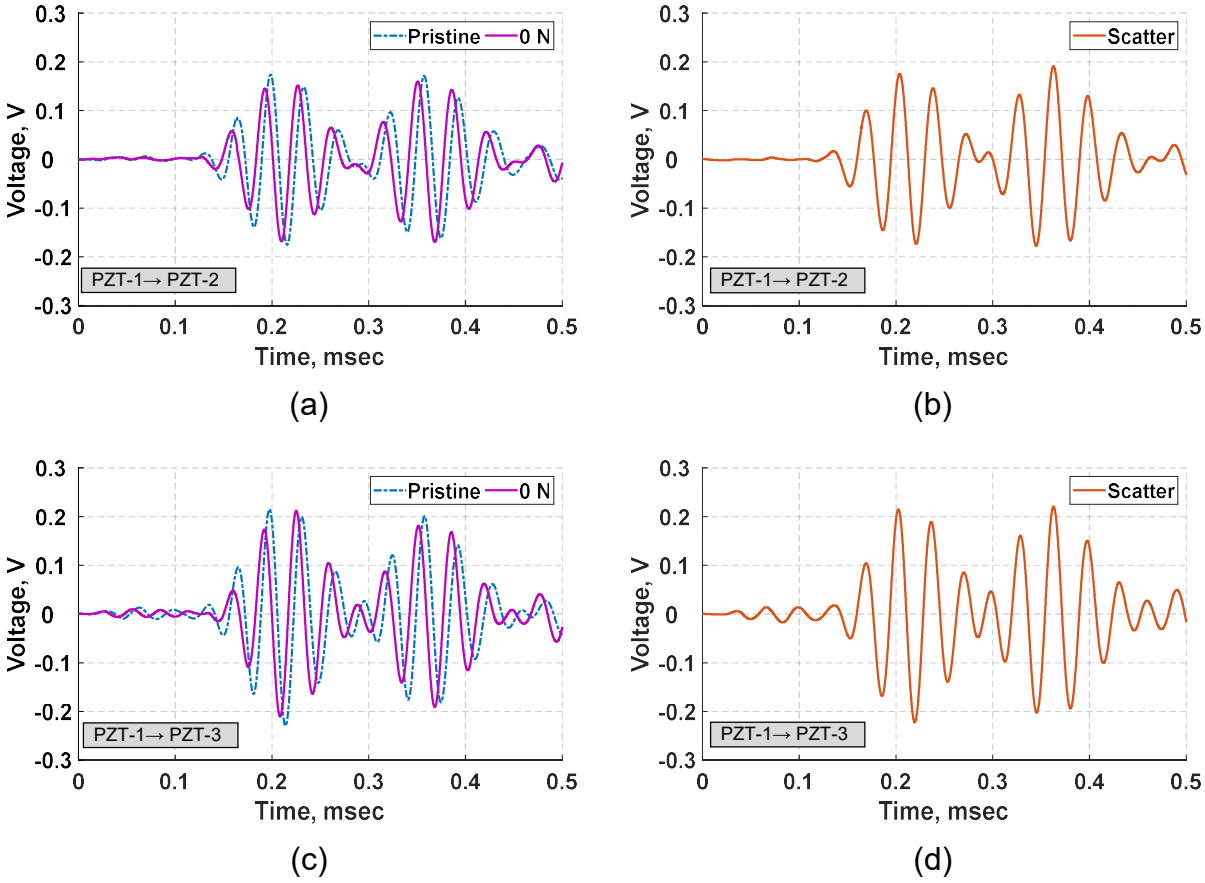

Figure 9.11: Comparison of signals (left column) and scattered signals (right column) at no-preload condition of 1.3 mm loading cycle: (a) and (b) d35 PZT-2 sensor; (c) and (d) d31 PZT-3 sensor.

In Figure 9.11, the waveform signals were picked up by the bondline-embedded d35 PZT and the surface-mounted d31 PZT for the three-point bending cycle of 1.3 mm mid-span deflection at no-preload condition. The received signals were superimposed with

baseline signals for comparison purposes, and the scattered signals which are the difference between the measured signals and the baseline signals were also calculated and displayed in Figure 9.11.

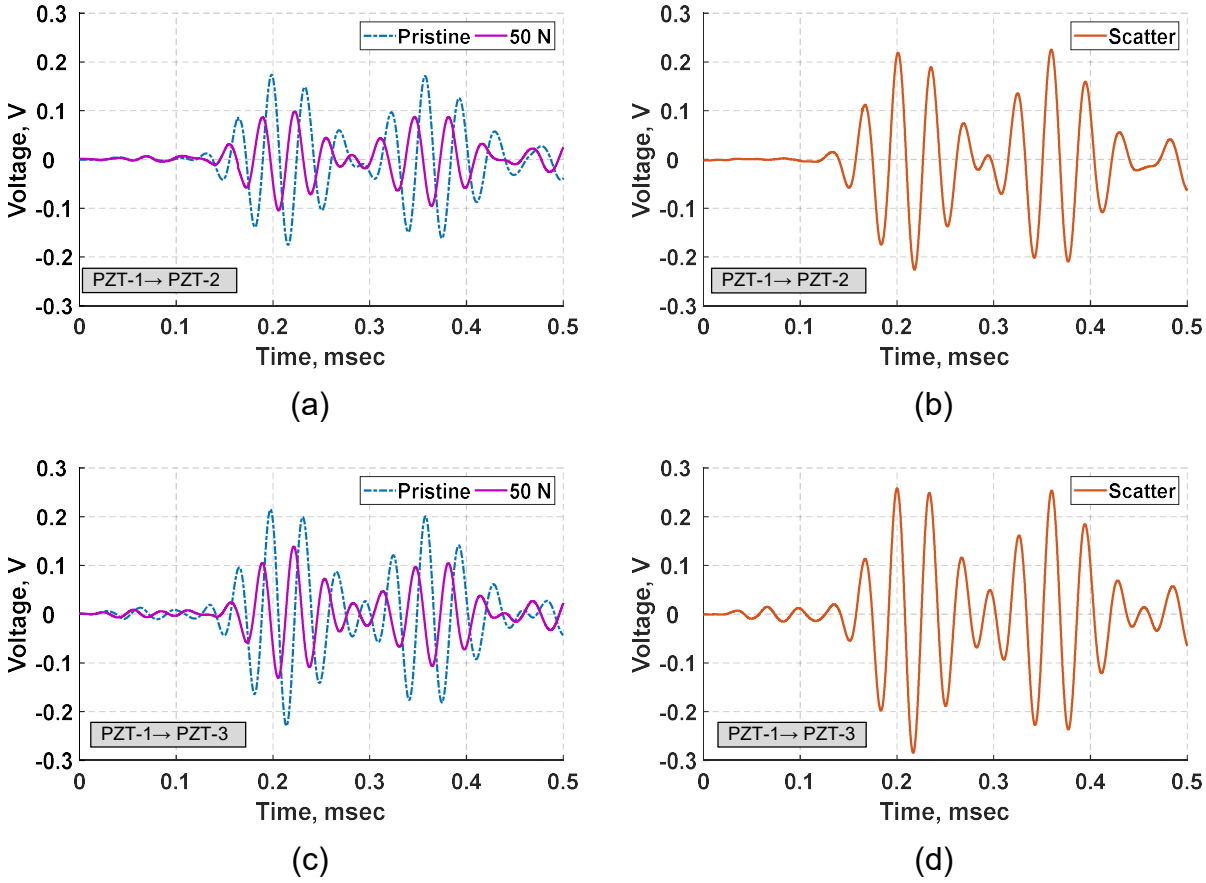

Figure 9.12: Comparison of signals (left column) and scattered signals (right column) from specimen with 50 N mid-span preload at 1.3 mm loading cycle: (a) and (b) d35 PZT-2 sensor; (c) and (d) d31 PZT-3 sensor.

Upon application of 50 N on the specimen and then performing ultrasonic inspection, the received signals along with the scattered signals for each sensor are shown in Figure 9.12. Despite the small magnitude of the applied load, the analysis indicates a significant difference between received signals from preload condition and no-preload condition. It can be noted from Figure 9.11 and Figure 9.12 that the captured signals at preload

condition are lagging the baseline signals with significant phase shift and voltage reduction as compared with received signals at no-preload condition.

The damage index based on PCC and NSE methods were also calculated for both loading conditions with results given in Table 9-2. The damage index values indicate that the damage exists with high severity at 1.3 mm mid-span deflection. The applied load at mid-span produces normal stresses across the thickness between loading supports, thus the propagating waves are anticipated to be modulated and be reflected on the received signals. However, this resulting distortion from a small applied load is also expected to be relatively small. The results strongly suggest that the applied load on the specimen caused a geometric change to the bondline damage resulting in significant distortion to the propagating waves.

Table 9-2: Damage indices at 1.3 mm mid-span deflection.

Wave Propagation Path	0 N		50 N	
	PCC	NSE	PCC	NSE
PZT-1 → PZT-2	0.5644	0.1790	1.2886	0.6947
PZT-1 → PZT-3	0.5398	0.1657	1.1829	0.6724

As previously discussed in Section 9.2.2, the mixed-mode crack was observed and fully developed in the bondline at 0.9 mm mid-span deflection, and that was followed by plastic deformation causing the crack to remain open resulting in low distortion in received signals over the range 1 mm – 2.3 mm mid-span deflection as shown in Figure 9.10. Therefore, in the preload condition at 1.3 mm mid-span deflection, the applied load is anticipated to open the mixed-mode crack and disbonds while the flexural waves transmitted through the bondline causing higher scattering of the propagating waves.

The results in Table 9-2 indicates that the damage index values calculated for bondline-embedded d35 PZT sensor are consistently higher than the surface-mounted d31 PZT sensor in both preload conditions. As mentioned earlier, the location of d35 PZT sensor in the bondline allows effective sensing of shear strains which interact profoundly to nonlinear defects as this finding was supported in literature [20,22].

9.3. Summary and Conclusions

The laminate specimen consisted of adhesively bonded aluminum plates with surface-mounted d31 PZT and bondline-embedded d35 PZT transducers was carefully designed for ultrasonic inspection. The joint defects in the bondline were created via quasi-static three-point bending test, and electromechanical impedance of d35 PZTs was measured after each three-point loading cycle to ensure their pristine state maintained throughout the experiment. It was observed that flexural waves generated by d35 PZT actuators exhibited strong interaction with joint damage especially nonlinear defects such as cracks and disbonds, supporting the capability of the proposed methodology for ultrasonic inspection of adhesively bonded structures. It was observed from experimental results that d35 PZT sensors have consistently showed higher voltage signal distortion to bondline defects as compared with the sensed signals by the surface-mounted d31 PZT sensor. It was also found that Pearson correlation coefficient is more sensitive to phase shift in received signals while normalized signal energy method more sensitive to amplitude of voltage waveform signals. The proposed approach provides novel insights into the benefits offered by bondline-embedded d35 PZT transducers for the health monitoring of adhesive bond joints.

Chapter 10
Conclusions and Future Work

In this chapter, the main contributions of this thesis are summarized and future directions of research are discussed. Limitations and challenges of the proposed approach are also discussed in some details.

10.1. Key Contributions and Conclusions

The response to the research questions presented in Chapter 2 are discussed briefly herein to highlight key contributions and conclusions of this thesis.

1. *Can embedded piezoelectric transducers in the bondline be used to identify the presence of damage in an adhesive joint through wave propagation?*

A novel approach was developed to tackle the challenge of detecting joint defects in laminate structures using ultrasonic inspection methods. This research has exploited a relatively new kind of piezoelectric transducers that were studied extensively through finite element multiphysics simulations and experimental testing. The proposed approach successfully produced promising results for detection of linear and nonlinear joint defects that often impose a significant challenge to detect using conventional nondestructive evaluation techniques. By placing the transducers within the bondline, it provided a direct coupling between the bondline and the d35 PZT transducers and that has improved the transmission and sensitivity of flexural waves to joint defects. The effectiveness of this methodology for the application of structural health monitoring was also evaluated experimentally. The results presented in the thesis provided fundamental work towards creating embedded, automated damage detection systems for adhesive bondlines using

antisymmetric waves generated by d35 PZT piezoelectric transducers embedded within the bondline of laminate structures.

2. *If so, can the proposed technique detect various types of defects such as voids, cracks, and disbond?*

Three damage cases including disbonds, cracks, and voids were introduced in the bondline of laminate structures to investigate the effectiveness of flexural waves to detect joint defects using bondline-embedded d35 PZT transducers. The root mean square deviation method was used as a damage index to quantify the sensitivity of flexural waves to joint defects. Flexural waves were found sensitive to the introduced joint defects but at various levels. They exhibited high sensitivity to disbond and vertical crack causing significant distortion in the received signals. However, flexural waves were found to show less sensitivity to voids compared to other considered defects. The high sensitivity of flexural waves to nonlinear defects was attributed to the change in the contact length during the propagation of flexural waves. The effects of defects on distributions of displacements and stresses were analyzed. Among all distributions, in-plane shear stress consistently showed noticeable distortion for all joint defects supporting the capability of d35 PZTs for inspection of laminate structures.

A laminate specimen with void was tested for damage detection analysis. By comparing the received signals from simulation and experiment, it was observed that the presence of void has mainly caused voltage attenuation in the waveforms. Another laminate specimen was also prepared with joint defects created via quasi-static three-point bending test, with results showing the ability of d35 piezoelectric transducers to monitor the bondline integrity. The EMI of d35 PZTs was measured after each three-point

loading cycle in order to ensure their pristine condition maintained throughout the experiment. A comparison between surface-mounted d31 PZT and bondline-embedded d35 PZT sensors was also conducted. It was found that received signals by bondline-embedded d35 PZTs have consistently showed higher distortion to bondline defects as compared with the sensed signals by the surface-mounted d31 PZT sensor.

3. *To what extent simulation approach can be beneficial to this study in terms of validation of the experimental results?*

The finite element simulations allowed to explore the feasibility of deploying d35 PZT transducers and conduct several studies to inform the future direction of laminate specimen design and testing methodology. A parametric study was performed by varying the thickness and length of d35 PZT transducers while monitoring the actuation strength and the sensed voltage signal. The size of bondline-embedded d35 PZT transducers was found to have a significant influence on the actuation strength and the sensing ability of d35 PZT transducers. Thicker and shorter d35 PZT sensors were found to produce stronger signals compared to thinner and longer d35 PZT sensors. However, d35 PZT actuators exhibited an opposite response to d35 PZT sensors. This presents an optimization challenge to generate strong actuation without compromising their sensing ability when transducers are used as both actuators and sensors.

The tuning analysis was investigated by varying the actuation frequency and examining the distributions of normal displacement and stresses across the laminate thickness. It was also noted that the strength of shear stress can be concentrated across the thickness of adhesive layer at lower actuation frequencies. This provides an opportunity to design d35 PZT actuators such that they generate strong in-plane shear

strains largely aimed to target the bondline region for adhesive joint evaluation. The frequency versus sensing voltage relation was also investigated by varying the actuation frequency and monitoring the amplitude of the received signals using FE simulations and then validating the results experimentally. The results from experiment and simulation indicated that there is an inverse relation between the actuation frequency and the maximum voltage.

The selectivity of d35 PZT sensors was also investigated in simulation by comparing voltage signals obtained from a bondline-embedded d35 PZT sensor and surface-mounted d31 PZT sensor. Mode conversion from wave interaction with a surface notch provided a collection of symmetric and antisymmetric waves in the laminate structure. It was found that d35 PZT sensors offer a selective hardware filter that primarily captures antisymmetric wave modes in the laminate structure while suppressing symmetric wave modes. The selectivity of d35 PZT sensors could be employed in signal processing to make the interpretation of the data more efficient, reducing uncertainty and leading to more reliable analysis outcomes. A beam-like specimen was also prepared to examine the directionality of flexural wave mode. The results from this specimen and plate-like specimen were found to be comparable confirming the ability of bondline-embedded d35 PZTs for generating directional waves.

4. *Can the proposed technique make use of signal processing methods to detect the severity of damage? If so, what is the damage detection algorithm?*

An investigation into a bondline-integrity health monitoring approach employing d35 piezoelectric transducers embedded inside the laminate specimen was considered in this work. The laminate specimen consisted of surface-mounted d31 PZT and bondline-

embedded d35 PZT transducers was carefully designed for ultrasonic inspection. The joint defects in the bondline was created via quasi-static three-point bending test, and electromechanical impedance of d35 PZTs was measured after each three-point loading cycle to ensure their pristine state maintained throughout the experiment.

A damage detection algorithm was developed to calculate damage index values based on Pearson correlation coefficient and normalized signal energy methods. The damage indices were also used as indicators of damage severity which can be used to trigger the need to schedule maintenance when the damage index above a certain threshold. The proposed algorithm was also equipped with discrete wavelet transform to de-noise experimental signals along with time-frequency analysis to examine the dispersion effect of the ultrasonic waves. It was found that Pearson correlation coefficient is more sensitive to phase shift in received signals while normalized signal energy method more sensitive to amplitude of voltage waveform signals. It was observed that flexural waves generated by d35 PZT actuators exhibited strong interaction with joint defects especially nonlinear defects such as cracks and disbonds, supporting the capability of the proposed methodology for ultrasonic inspection of adhesively bonded structures. It was also observed from experimental results that d35 PZT sensors have consistently showed higher voltage signal distortion to bondline defects as compared with the sensed signals by the surface-mounted d31 PZT sensor due to the location advantage of d35 PZT sensor being in the bondline sensing shear strain waves at the neutral axis of the laminate specimen. The proposed approach provides novel insights into the benefits offered by bondline-embedded d35 PZT transducers for the health monitoring of adhesive bond joints.

10.2. Future Work

Future work will include experimentally validating the parametric study of d35 PZT size while being embedded in the bondline of laminate structures. Furthermore, the selectivity of d35 PZT sensors to antisymmetric wave modes and rejecting symmetric modes needs to be experimentally verified through comparison of voltage signals from surface-mounted d31 and bondline-embedded d35 PZT sensors. Because this work is expected to be of importance for SHM of adhesive joints, testing the ability to use flexural waves generated and sensed by bondline-embedded d35 PZT transducers to detect defects in composites should be performed as well. Placing PZT transducers in the bondline also provides protection for the transducers from environmental, chemical, and physical hazards.

While measuring the bond strength of laminates is still under investigation, embedding sensors in the bondline could provide an opportunity to address this challenge. Future work will require investigating the effects of embedding sensors on the bond strength as well. Design of optimization and miniaturization of shear-mode piezoelectric transducers are of considerable interest to accelerate their integration into ultrasonic SHM systems. Furthermore, experimental work was mainly limited to a low actuation frequency range due to large thickness of PZT transducers, thus further investigation concerning the relation between actuation frequency of thinner PZTs and sensitivity of waves to joint defects need to be considered as well.

The feature extraction methods used herein were relatively sufficient to detect damage and estimate its severity. It was observed the superposition of multimode Lamb waves could present a challenge to isolate existing individual modes and analyze their

characteristics. Therefore, extracting the damage characteristics from multimode waveforms requires a robust signal processing algorithm to accomplish this purpose with minimal uncertainty. This challenge often compounds when multiple defects with different damage characteristics exist between two transducers in the structure. Furthermore, more information about existing damage characteristics such as location and severity will require to develop algorithms that involve measurements for multiple features and be correlated to fatigue diagnostics and prognostics of structures.

The ToF method was implemented to identify the propagating modes in the media and location of defects. A threshold was used to determine the arrival time of a propagating mode. The majority of the error however found in damage localization and uncertainties in group velocities of propagating modes was attributed to the thresholding method. A promising method to overcome this challenge is to use time-frequency approach in order to track the center frequency of wave packet rather the arrival time.

In health monitoring of bondline integrity, the defect type has not been controlled thus multiple joint defects were present simultaneously. That imposed a challenge to correlate change in waveform signals with a certain type of defect. Extracting specific features caused by each type of damage in waveform signals is expected to be a challenging task and would require more sophisticated signal processing techniques. The amount of distortion inflicted on the propagating waves determines the dominant type of defect. Thus, the presence of different types of defects also imposes high uncertainty on identifying the type of damage by solely using damage index which represents a lump sum of damage effects on propagating waves. In real life structures, however, damage is

often composed of two or more types of defects, making the proposed methodology appropriate for this study.

References

1. Giurgiutiu, V. *Structural Health Monitoring With Piezoelectric Wafer Active Sensors*; 2nd ed.; Elsevier Inc.: London, 2014; ISBN 9780124186910.
2. Stepinski, T.; Uhl, T.; Staszewski, W. *Advanced Structural Damage Detection Advanced Structural Damage Detection: From Theory To Engineering*; John Wiley and Sons Ltd: West Sussex, UK, 2013; ISBN 9781118422984.
3. Glišić, B.; Inaudi, D. *Fibre Optic Methods for Structural Health Monitoring*; John Wiley and Sons Ltd: West Sussex, UK, 2007; ISBN 978-0-470-06142-8.
4. Lorenzo, E. Di; Kosova, G.; Musella, U.; Manzato, S.; Peeters, B.; Marulo, F.; Desmet, W. Structural health monitoring challenges on the 10-MW offshore wind turbine model. *Journal of Physics: Conference Series* **2015**, *628*, 1–8, doi:10.1088/1742-6596/628/1/012081.
5. Altammar, H.; Kaul, S.; Dhingra, A. K. Use of wavelets for damage diagnostics in truss structures. *International Journal of Structural Integrity* **2017**, *8*, 373–391, doi:10.1108/IJSI-05-2016-0017.
6. Adams, D. *Health Monitoring of Structural Materials and Components: Methods with Applications*; John Wiley and Sons Ltd: West Sussex, UK, 2007; ISBN 0470511575.
7. MarketsandMarkets Structural health monitoring market by Solutions (hardware: sensors, data acquisition system; software & services), technology (wired and wireless), end users and geography - global forecast to 2022 Available online: https://www.marketsandmarkets.com/Market-Reports/structural-health-monitoring-market-101431220.html (accessed on Nov 22, 2017).
8. Gulgec, N. S.; Shahidi, G. S.; Matarazzo, T. J.; Pakzad, S. N. Current Challenges with BIGDATA Analytics in Structural Health Monitoring. *Structural Health Monitoring & Damage Detection* **2017**, *7*, 79–84, doi:10.1007/978-3-319-54109-9_9.
9. Rose, J. L. *Ultrasonic Guided Waves in Solid Media*; Cambridge University Press: New York, 2014; ISBN 9781107273610.
10. Ostachowicz, W.; Kudela, P.; Krawczuk, M.; Zak, A. *Guided Waves in Structures for SHM*; John Wiley and Sons Ltd, 2012; ISBN 9781119965855.
11. Joseph L. Rose Health Monitoring of Composite Structures Using Guided Waves. **2011**, *298*, 0–100, doi:10.1002/9780470612248.ch2.
12. Graff, K. F. *Wave motion in elastic solids*; Oxford University Press: London, 1991; ISBN 0486667456.
13. Rao, S. S. *Mechanical Vibrations*; 6th ed.; Hoboken, NJ: Pearson Education, Inc, 2010; Vol. 67; ISBN 9780132128193.
14. Rose, J. L. *Ultrasonic waves in solid media*; Cambridge University Press, 1999; ISBN 0521548896.

15. Pau, A.; Achillopoulou, D. V.; Vestroni, F. Scattering of guided shear waves in plates with discontinuities. *NDT and E International* **2016**, *84*, 67–75, doi:10.1016/j.ndteint.2016.08.004.

16. Köhler, B.; Gaul, T.; Lieske, U.; Schubert, F. Shear horizontal piezoelectric fiber patch transducers (SH-PFP) for guided elastic wave applications. *NDT and E International* **2016**, *82*, 1–12, doi:10.1016/j.ndteint.2016.04.001.

17. Yu, X.; Manogharan, P.; Fan, Z.; Rajagopal, P. Shear horizontal feature guided ultrasonic waves in plate structures with 90° transverse bends. *Ultrasonics* **2016**, *65*, 370–9, doi:10.1016/j.ultras.2015.08.012.

18. Nazeer, N.; Ratassepp, M.; Fan, Z. Damage detection in bent plates using shear horizontal guided waves. *Ultrasonics* **2017**, *75*, 155–163, doi:10.1016/j.ultras.2016.11.020.

19. Kinloch, A. J. *Adhesion and adhesives : science and technology*; Chapman and Hall, 1987; ISBN 9780412274404.

20. Kundu, T.; Maji, A.; Ghosh, T.; Maslov, K. Detection of kissing bonds by Lamb waves. *Ultrasonics* **1998**, *35*, 573–580, doi:10.1016/S0041-624X(97)00095-4.

21. Marty, P. N. P. N.; Desai, N.; Andersson, J.; Desaï, N.; Andersson, J. NDT of kissing bond in aeronautical structures. *World Conference on NDT* **2004**.

22. Nagy, P. B. Ultrasonic detection of kissing bonds at adhesive interfaces. *Journal of Adhesion Science and Technology* **1991**, *5*, 619–630, doi:10.1163/156856191X00521.

23. Díaz Valdés, S. H.; Soutis, C.; Diaz Vald, S. H.; Soutis, C. Real-time nondestructive evaluation of fiber composite laminates using low-frequency Lamb waves. *The Journal of the Acoustical Society of America* **2002**, *111*, 2026–2033, doi:10.1121/1.1466870.

24. Osmont, D.; Devillers, D.; Taillade, F. Health Monitoring of Sandwich Plates Based on the Analysis of the Interaction of Lamb Waves with Damages. *Smart structures and Integrated Systems* **2001**, *4327*, 290–301.

25. Wilcox, P. D.; Lee, C. K.; Scholey, J. J.; Friswell, M. I.; Wisnom, M. R.; Drinkwater, B. W. Quantitative structural health monitoring using acoustic emission. *SPIE Conference Proceedings* **2006**, *6173*, 61731K-61731K–10, doi:10.1117/12.658510.

26. Cuc, A.; Giurgiutiu, V. Wave Propagation and Dispersion OF Lamb Waves in Adhesively-Bonded Structures. *Proceedings of IMECE 2004: 2004 ASME International Mechanical Engineering Congress* **2004**, 1–6.

27. Blanas, P.; Wenger, M. P.; Shuford, R. J.; Das-Gupta, D. K. Active composite materials and damage monitoring. *International Workshop on Structural Health Monitoring* **1997**, 199–207.

28. Zhuang, Y.; Li, Y.-H.; Kopsaftopoulos, F.; Chang, F.-K. A self-diagnostic adhesive for monitoring bonded joints in aerospace structures. *The composites and advanced materials Expo* **2015**, 1–14, doi:10.1117/12.2219361.

29. Dugnani, R.; Zhuang, Y.; Kopsaftopoulos, F.; Chang, F.-K. K. K. Adhesive bond-line degradation detection via a cross-correlation electromechanical impedance – based approach. *Structural Health Monitoring* **2016**, *15*, 650–667, doi:10.1177/1475921716655498.

30. Spectroscopy, U.; Stepinski, T.; Jonsson, M. Narrowband ultrasonic spectroscopy for NDE of layered structures. *Insight: Non-Destructive Testing and Condition Monitoring* **2005**, *47*, 220–224, doi:10.1784/insi.47.4.220.63147.

31. Murayama, H.; Kageyama, K.; Uzawa, K.; Ohara, K.; Igawa, H. Strain monitoring of a single-lap joint with embedded fiber-optic distributed sensors. *Structural Health Monitoring: An International Journal* **2012**, *11*, 325–344, doi:10.1177/1475921711419994.

32. Sulejmani, S.; Sonnenfeld, C.; Geernaert, T.; Luyckx, G.; Mergo, P.; Urbanczyk, W.; Chah, K.; Thienpont, H.; Berghmans, F. Disbond monitoring in adhesive joints using shear stress optical fiber sensors. *Smart Materials and Structures* **2014**, *23*, doi:10.1088/0964-1726/23/7/075006.

33. Yeager, M.; Todd, M.; Gregory, W.; Key, C. Assessment of embedded fiber Bragg gratings for structural health monitoring of composites. *Structural Health Monitoring* **2017**, *16*, 262–275, doi:10.1177/1475921716665563.

34. Pieper, D.; Donnell, K. M.; Abdelkarim, O.; Elgawady, M. A. Embedded FSS sensing for structural health monitoring of bridge columns. *Conference Record - IEEE Instrumentation and Measurement Technology Conference* **2016**, *2016-July*, doi:10.1109/I2MTC.2016.7520475.

35. Kamal, A.; Giurgiutiu, V. Shear horizontal wave excitation and reception with shear horizontal piezoelectric wafer active sensor (SH-PWAS). *Smart Materials and Structures* **2014**, *23*, 085019, doi:10.1088/0964-1726/23/8/085019.

36. Benjeddou, A.; Deü, J. F. Piezoelectric transverse shear actuation and sensing of plates, part 1: A three-dimensional mixed state space formulation. *Journal of Intelligent Material Systems and Structures* **2001**, *12*, 435–449, doi:10.1106/TTBW-9YC2-33KY-8E66.

37. Benjeddou, A.; Deü, J. F. Piezoelectric transverse shear actuation and sensing of plates, part 2: Application and analysis. *Journal of Intelligent Material Systems and Structures* **2001**, *12*, 451–467, doi:10.1106/J8DX-R3AT-EA6G-85K7.

38. Koutsawa, Y.; Giunta, G.; Nasser, H.; Belouettar, S. Static analysis of shear actuated piezo-electric beams via hierarchical FEM theories. *Mechanics of Advanced Materials and Structures* **2015**, *22*, 3–18, doi:10.1080/15376494.2014.907946.

39. Giurgiutiu, V.; Rogers, C. A. Recent advancements in the electromechanical (E/M) impedance method for structural health monitoring and NDE. In *5th Annual International Symposium on Smart Structures and Materials*; Regelbrugge, M. E., Ed.; International Society for Optics and Photonics, 1998; Vol. 3329, pp. 536–547.

40. Dugnani, R.; Zhuang, Y.; Kopsaftopoulos, F.; Chang, F. K. Adhesive bond-line degradation detection via a cross-correlation electromechanical impedance–based

approach. *Structural Health Monitoring* **2016**, *15*, 650–667, doi:10.1177/1475921716655498.

41. Gao, H.; Shi, Y.; Rose, J. L. Guided wave tomography on an aircraft wing with leave in place sensors. *AIP Conference Proceedings* **2005**, *760*, 1788–1794, doi:10.1063/1.1916887.
42. Tseng, K.-H. K. H.; Naidu, A. S. K. Non-parametric damage detection and characterization using smart piezoceramic material. *Smart Mater. Struct.* **2002**, *11*, 317–329.
43. Torkamani, S.; Roy, S.; Barkey, M. E.; Sazonov, E.; Burkett, S.; Kotru, S. A novel damage index for damage identification using guided waves with application in laminated composites. *Smart Materials and Structures* **2014**, *23*, 095015, doi:10.1088/0964-1726/23/9/095015.
44. Wu, Z.; Qing, X. P.; Ghosh, K.; Karbhari, V. M.; Chang, F.-K. Health monitoring of bonded composite repair in bridge rehabilitation. *Smart Materials and Structures* **2008**, *17*, 045014, doi:10.1088/0964-1726/17/4/045014.
45. Cheraghi, N.; Taheri, F. A damage index for structural health monitoring based on the empirical mode decomposition. *JOURNAL OF MECHANICS OF MATERIALS AND STRUCTURES* **2007**, *2*, 43–62.
46. Hu, X.; Zhu, H.; Wang, D. A study of concrete slab damage detection based on the electromechanical impedance method. *Sensors* **2014**, *14*, 19897–909, doi:10.3390/s141019897.
47. Giurgiutiu, V.; Zagrai, A. N. Characterization of Piezoelectric Wafer Active Sensors. *Journal of Intelligent Materials Systems and Structures* **2000**, *11*, 959–976, doi:10.1177/104538900772664260.
48. Peairs, D. M.; Park, G.; Inman, D. J. Improving Accessibility of the Impedance-Based Structural Health Monitoring Method. *Intelligent Materials Systems and Structures* **2004**, *15*, 129–139, doi:10.1177/1045389X04039914.
49. Proakis, J. G.; Manolakis, D. G. *Digital signal processing*; Pearson Prentice Hall, 2007; ISBN 9780131873742.
50. Mallat, S. G. *A wavelet tour of signal processing: the sparse way*; Elsevier/Academic Press, 2009; ISBN 9780080922027.
51. Yang, J. *Analysis of Piezoelectric Devices*; World Scientific Publishing Co. Pte. Ltd.: Singapore, 2006; ISBN 978-981-256-861-8.
52. Tiersten, H. F. Thickness vibrations of piezoelectric plates. *The Journal of the Acoustical Society of America* **1963**, *35*, 53–58, doi:10.1121/1.424353.
53. Bathe, K.-J. *Finite Element Procedures*; 2nd ed.; Prentice Hall, Pearson Education, Inc.: Watertown, MA, 2014; ISBN 978-0-9790049-5-7.
54. ANSYS Inc. *ANSYS Contact Technology Guide*; Canonsburg, PA, 2017;
55. Kundu, T.; Maslov, K. Material interface inspection by Lamb waves. *International Journal of Solids and Structures* **1997**, *34*, 3885–3901, doi:10.1016/S0020-

7683(96)00197-7.

56. Boashash, B. *Time frequency signal analysis and processing: a comprehensive reference*; 2nd Editio.; Academic Press, 2015; ISBN 9780123985255.

57. ITW Chemtronics *Technical Data Sheet Circuit Works 60 Minute Conductive Epoxy*; Kennesaw, GA, 2008;

58. Henkel Corporation Aerospace *LOCTITE EA 9394: Epoxy Paste Adhesive*; Bay Point, CA, 2013;

59. Raghavan, A.; Cesnik, C. E. S. Review of guided-wave structural health monitoring. *Shock and Vibration Digest* 2007, *39*, 91–114.

60. Broda, D.; Staszewski, W. J. J.; Martowicz, A.; Uhl, T.; Silberschmidt, V. V. V. Modelling of nonlinear crack–wave interactions for damage detection based on ultrasound—A review. *Journal of Sound and Vibration* **2014**, *333*, 1097–1118, doi:10.1016/j.jsv.2013.09.033.

61. Mueller, I.; Janapati, V.; Banerjee, S.; Lonkar, K.; Roy, S.; Chang, F.-K. On the performance quantification of active sensing SHM systems using model-assisted POD methods. *Proceedings of the Eighth International Workshop on Structural Health Monitoring* **2011**, 12.

62. Methods, S. T. ASTM E 290 - Standard Test Methods for Bend Testing of Material for Ductility. *Current* **1998**, doi:10.1520/E0290-13.Copyright.

63. Alleyne, D. N.; Cawley, P. The Interaction of Lamb Waves with Defects. *IEEE Transactions on Ultrasonics, Ferroelectrics, and Frequency Control* **1992**, *39*, 381–397, doi:10.1109/58.143172.

64. Greve, D. W.; Tyson, N.; Oppenheim, I. J. Interaction of defects with Lamb waves in complex geometries. *Proceedings - IEEE Ultrasonics Symposium* **2005**, *1*, 297–300, doi:10.1109/ULTSYM.2005.1602854.

65. Altammar, H.; Dhingra, A.; Salowitz, N. Investigating the Feasibility of Ultrasonic Shear Actuation for Evaluation of Adhesive Joints in Multilayered Structures: FE Simulation. *ASNT Annual Conference* **2017**, 25–34.

Appendix

Piezoelectric Material Properties of PZT-5A polarized in z - direction,

$$[c]=\begin{bmatrix} 120.4 & 75.2 & 75.1 & 0 & 0 & 0 \\ 75.2 & 120.4 & 75.1 & 0 & 0 & 0 \\ 75.1 & 75.1 & 110.9 & 0 & 0 & 0 \\ 0 & 0 & 0 & 21.1 & 0 & 0 \\ 0 & 0 & 0 & 0 & 21.1 & 0 \\ 0 & 0 & 0 & 0 & 0 & 22.6 \end{bmatrix} GPa$$

(1)

$$[e]=\begin{bmatrix} 0 & 0 & -5.351 \\ 0 & 0 & -5.351 \\ 0 & 0 & 15.7835 \\ 0 & 12.2947 & 0 \\ 12.2947 & 0 & 0 \\ 0 & 0 & 0 \end{bmatrix} \frac{C}{m^2} \qquad \left[\varepsilon^T\right]=\varepsilon_o\begin{bmatrix} 1851 & 0 & 0 \\ 0 & 1851 & 0 \\ 0 & 0 & 1581 \end{bmatrix}$$

Piezoelectric Material Properties of PZT-5A polarized in x - direction,

$$[c]=\begin{bmatrix} 110.9 & 75.1 & 75.1 & 0 & 0 & 0 \\ 75.1 & 120.4 & 75.2 & 0 & 0 & 0 \\ 75.1 & 75.2 & 120.4 & 0 & 0 & 0 \\ 0 & 0 & 0 & 22.6 & 0 & 0 \\ 0 & 0 & 0 & 0 & 21.1 & 0 \\ 0 & 0 & 0 & 0 & 0 & 21.1 \end{bmatrix} GPa$$

(2)

$$[e]=\begin{bmatrix} 15.784 & 0 & 0 \\ -5.351 & 0 & 0 \\ -5.351 & 0 & 0 \\ 0 & 0 & 0 \\ 0 & 0 & 12.295 \\ 0 & 12.295 & 0 \end{bmatrix} \frac{C}{m^2} \qquad \left[\varepsilon^T\right]=\varepsilon_o\begin{bmatrix} 1581 & 0 & 0 \\ 0 & 1851 & 0 \\ 0 & 0 & 1851 \end{bmatrix}$$

In Eq.(1) and Eq.(2), ε_o is the vacuum permittivity and has a value of 8.854 μF/m.

Table 1: Material properties of shear-mode PZT, Hysol EA9394 adhesive epoxy, aluminum 6061-T6.

Property	Unit	Symbol	PZT-5A	Adhesive	Aluminum
Young's Modulus	10^9 N/m^2	Y_{11}	61.0	4.24	68.9
	10^9 N/m^2	Y_{33}	53.2	4.24	68.9
Shear's Modulus	10^9 N/m^2	G_{12}	22.6	1.46	25.9
	10^9 N/m^2	G_{13}	10.5	1.46	25.9
Poisson's ratio	1	v_{12}	0.35	0.45	0.33
	1	v_{13}	0.44	0.45	0.33
Density	kg/m^3	ρ	7600	1360	2700
Dielectric permittivity	8.854 μF/m	ε_{11}	1851	------	------
	8.854 μF/m	ε_{33}	1581	------	------
Piezoelectric coefficient	10^{-12} m/V	d_{35}	584	------	------
	10^{-12} m/V	d_{31}	−171	------	------
	10^{-12} m/V	d_{33}	374	------	------